Dissertation

submitted to the
Combined Faculties of the Natural Sciences and Mathematics
of the Ruperto-Carola-University of Heidelberg, Germany

for the degree of
Doctor of Natural Sciences

Put forward by
Anna Battista
born in Verona, Italy

Oral examination: 15 - 04 - 2015

Physical models for the motility of malaria parasites

Referees: Prof. Dr. Ulrich Schwarz
Prof. Dr. Heinz Horner

Zusammenfassung

Die Krankheit Malaria wird durch einen einzelligen Parasiten übertragen, der über seinen ganzen Lebenszyklus hinweg die Fähigkeit der Fortbewegung benötigt. Die mobilste Form des Parasiten ist der „Sporozoit“. Dies ist die Form, die vom Mosquito in die Haut des Wirts injiziert wird. Seine gebogene, längliche Geometrie bestimmt die Form seiner Trajektorien. Wir verfolgen verschiedene Modellansätze, um die physikalischen Grundlagen der Fortbewegung von Sporozoiten zu verstehen. Als erstes entwickeln wir ein geometrisches Modell für die Migration von einzelnen Sporozoiten in der Anwesenheit von Hindernissen. Dies erlaubt es uns, die experimentell beobachteten *in vivo* Trajektorien auf die strukturellen Eigenschaften des Parasitens und seiner Umgebung zurückzuführen. Unser zweites Modell zeigt, dass Sporozoiten als Kollektiv sich in stabilen Wirbelstrukturen organisieren können, wie experimentell in den Speicheldrüsen von infizierten Mosquitos beobachtet wird. Drittens verwenden wir einen mikroskopischen Ansatz, um die experimentell beobachtete Adhäsionsdynamik von gleitenden Sporozoiten mit Translations- und Rotationsreibung zu verbinden. Zum Schluss verbinden wir die Fortbewegung von Sporozoiten mit ihrer mechanischen Verformung. Eine Analyse von experimentellen Zeitreihen von Geschwindigkeit und Krümmung erlaubt es, die verschiedenen Komponenten des Fortbewegungsapparats zu unterscheiden. Insgesamt erklären unsere physikalischen Modelle viele wesentliche Eigenschaften der gleitenden Fortbewegung von Sporozoiten und ergeben Vorhersagen, die neuartige Experimente motivieren.

Abstract

The malaria disease is transmitted by a unicellular parasite that heavily relies on motility throughout its life cycle. We present different modelling approaches to the migration of the most motile form of the malaria parasite, the sporozoite, which is injected into the host skin by a mosquito. Their bent, elongated geometry shapes their trajectories. We first develop a geometrical model for the migration of a single sporozoite in the presence of obstacles. This enables us to trace the complex trajectories observed *in vivo* back to the structural features of both parasite and environment. Our second model shows that sporozoites can collectively organise in stable whirl-like structures, as observed experimentally in the salivary glands of malaria-infected mosquitos. Thirdly, we adopt a microscopic viewpoint linking the experimentally observed adhesion dynamics of gliding sporozoites with the presence of translational and rotational stochastic friction. Finally, we connect the propulsion system of sporozoites with mechanical cell deformations. Analysing experimental time series of sporozoite speed and curvature we can quantitatively distinguish the components of the gliding machinery. Overall, our physical models explain many essential features of gliding sporozoites and provide predictions that motivate novel experiments.

Contents

1 Introduction

In this chapter we offer an introduction to the four independent modelling projects presented in the main body of this work. The central subject of this thesis is the migration of malaria parasites, that we approach by developing physical models using a variety of theoretical and computational approaches, targeting biologically relevant problems at different length-scales.

While the study of malaria traditionally belongs to the cell-biological and medical areas, in this thesis we demonstrate that the migration of malaria parasites is accessible to a physical analysis.

Infectious diseases represent a highly important issue for global health. Among the growing efforts to understand and battle them, the use of novel approaches, like the physical modelling of traditionally biological problems, is of primary importance.

1.1 Introduction to malaria

Malaria is a parasitic disease transmitted to vertebrates, including humans, and caused by protozoan parasites belonging to the genus *Plasmodium*. Malaria relies on *Anopheles* mosquitos for transmission and thrives in environmental conditions that favour mosquito breeding.

According to estimates by the World Health Organisation (WHO) [1], the yearly toll from malaria amounts to about half a million deaths per year, with about 200 million infections. The dominating area in terms of mortality and morbidity is the Sub Saharan African region, with children and infants particularly vulnerable (Fig. 1.1).

Because of the high human and social cost of malaria, decades of efforts are piling up aiming at eradicating the disease. While even diagnoses can still be challenging, especially in remote areas, global efforts against malaria have been achieving significant and durable decreases in infections using a range of heterogeneous strategies. Among other modes of intervention, vector control targets mosquitos and mosquito larvae, promoting the use of insecticide-treated mosquito nets. On the human front, the action focuses on pharmacological therapies, with particular attention to infants, children and pregnant women. In parallel, research is targeting emerging issues, like drug-resistant parasites and insecticide-resistant mosquitos, while the long term goal of the efforts against malaria remains the generation of a preventive vaccine [1].

Plasmodium, the causative agent of malaria, exists in about 120 species, that infect

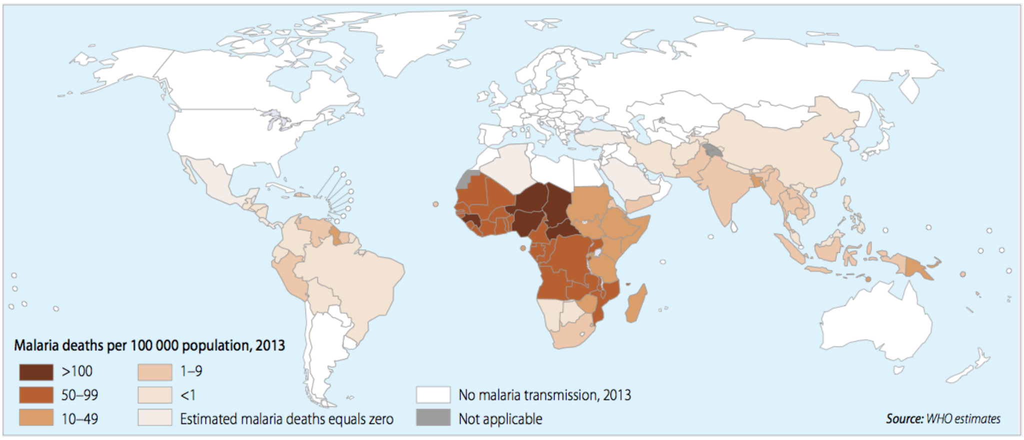

Source: WHO estimates

Figure 1.1: Distribution of deaths from malaria in the world in 2013. The disease affects the Sub Saharan African region with particular violence [1].

different species of vertebrates. Humans are only vulnerable to four Plasmodium species. Among those, the most common and dangerous is P. *falciparum*, that is dominant in Sub Saharan Africa. Plasmodium *vivax* instead is prevalent in Southeast Asia and Latin America, while only a fraction of the infections is caused by P. *ovale* and P. *malariae* [2].

1.1.1 The life cycle of malaria parasites

All species of Plasmodium are characterised by a complex life cycle [3,4]. Being a parasite, Plasmodium exploits a vertebrate host for replication, while host-to-host transmission relies on a vector (*Anopheles* mosquito). The life cycle of malaria parasites involves several replication stages in different environments (Fig. 1.2), distributed between the host and the vector, and relies heavily on active parasite motility for its successful completion.

Parasites, in the form of sporozoites, are first injected into the skin of the host during a bite by an infected mosquito. Sporozoites are highly motile cells and migrate through the dermis in order to enter a blood vessel and join the blood stream [5]. They follow passively the blood flow till they reach the liver, where they actively migrate through several liver cells until they find the one suitable for the start of the first replication stage.

There, each sporozoite forms a cyst and replicates producing thousands of merozoites, that are released into the blood stream upon rupture of the cyst following complete maturation. This stage can take between 5 and 16 days, depending on the parasite species.

In the blood stream, merozoites engage in an asexual replication cycle that, depending on species, takes between 1 and 3 days. Merozoites actively invade red blood cells and differentiate within. As the parasite develops within an infected red blood cell, the cell itself becomes rounded and knobbed, and adheres to the inner walls of the blood vessels, thereby impeding the proper flowing of the blood [6–10]. After new merozoites are formed, the infected red blood cells burst open and release the newborn parasites to repeat the cycle. This is the part of the malaria life cycle associated with the typical symptoms of

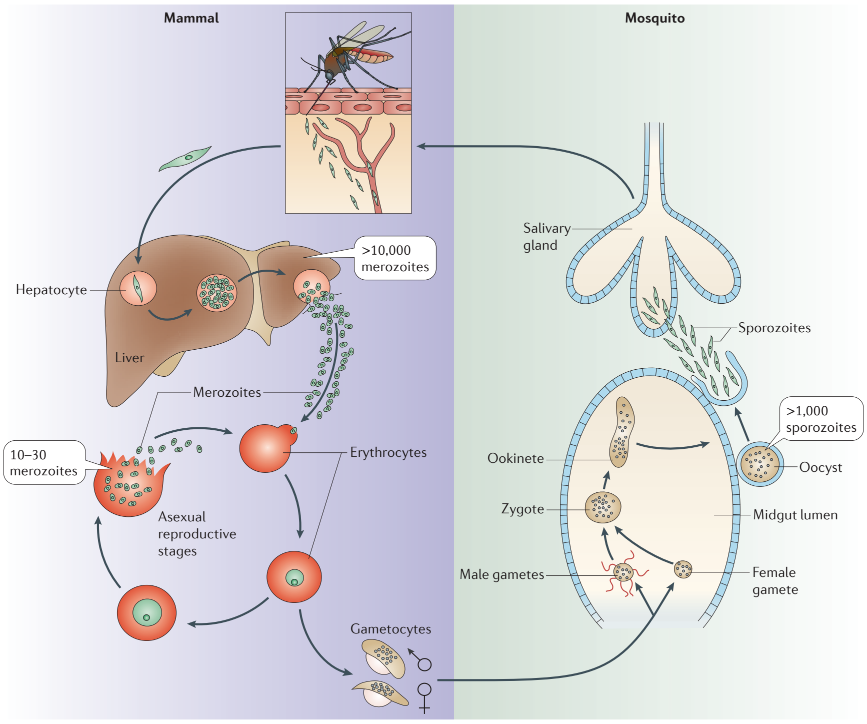

Figure 1.2: Life cycle of the malaria parasite. The parasites are injected in the skin of the host in the form of sporozoites via a bite by an infected mosquito. After a migration stage in the skin, the parasites reach the liver via the blood flow and undergo a replication stage, producing merozoites. Merozoites replicate further in the blood invading erythrocytes. The host cycle is completed when another mosquito bites the host and uptakes gametocytes, the sexual parasite stage stemming from the blood replication stage. In the mosquito, a final complex replication stage generates sporozoites ready to be injected into a new host (figure from [4]).

the disease, such as periodic fevers.

In a manner not yet fully understood, some of the merozoite-infected blood cells leave this cycle to develop sexual forms of the parasite, releasing male and female gametocytes into the blood circulation. When gametocytes are taken up by a mosquito during a blood meal, they develop into mature sex cells (gametes) within the mosquito gut. Male and female gametes fuse to form zygotes, which in turn become actively moving ookinetes, that burrow into the midgut wall of the mosquito and form oocysts. Each oocyst grows to produce hundreds of sporozoites that, upon bursting of the cyst (8-15 days, depending on species), actively invade the mosquito salivary gland, where they are stored ready to be injected at the next mosquito bite, with which the whole cycle can start again [3, 4].

1.2 Parasite motility in the life cycle

Cell motility is fundamental at several stages during the life cycle of the malaria parasite. Sporozoites in the host first rely on active migration to go through the dermis to reach a blood vessel [4,5] and, second, in order to reach a liver cell suitable for replication [4]. Merozoites need to actively invade red blood cells to be able to establish the asexual replication stage [3]. In the mosquito, ookinetes burrow into the midgut wall before forming the oocysts within which sporozoites can mature. And again, sporozoites in the mosquito need to actively invade the salivary glands to allow the mosquito to inject them into a new host [4,11].

1.2.1 Merozoites

Because of their medical relevance, most experimental efforts focus on the liver and blood stage of malaria and, specifically, on the molecular machinery responsible for active invasion of red blood cells [12–15]. Invasion of erythrocytes represents a particularly advantageous choice for merozoites, in that it allows access to an area that is protected from attacks by the immune system of the host and is therefore suitable for replication. As reported in [13], merozoites first recognise red blood cells via surface receptors, that trigger contact between the parasite and the membrane of the cell. Following contact, the merozoite reorients and begins the invasion of the erythrocyte, exploiting an actomyosin-based motor that provides the necessary power. Invading merozoites do not rupture the erythrocyte, but in fact penetrate in it by forming a vacuole. Maturation of the new Plasmodium *falciparum* parasites within the red blood cell causes the erythrocyte to round up and generates regularly spaced knobs on its surface [6,7,15]. The shape change and knobs cause the infected erythrocyte to adhere to and roll on the inner walls of the blood vessels, disturbing the proper flowing of the blood [8,9]. Interestingly, infected red blood cells perform rolling adhesion in a manner very similar to that of leukocytes, that need to adhere to the inner walls of the blood vessels in order to exit the blood flow to implement an immune response whenever necessary [10,16]. A model for rolling adhesion in shear flow, motivated by the behaviour of leukocytes, can be found in [17].

In the last years, the biophysics of red blood cell invasion and rupture has been generating considerable interest, triggering experimental and theoretical studies. A recent study analyses a theoretical model that considers the contribution to invasion given by the wrapping of the membrane of the red blood cell [18]. The authors conclude that the active contribution of the actomyosin motor of the parasite to invasion is less than expected, thanks to the mutual interaction between the invading parasite and the membrane of the erythrocyte. Not only the membrane dynamics during invasion is noteworthy, but also the dynamics of the membrane during the rupture of an infected red blood cell. In [19,20], the authors observe the membrane wrapping that accompanies the egress of merozoites as a result of an elastic instability. They argue that membrane wrapping allows an efficient angular dispersion of the parasites, and propose a theoretical, mechanical model that identifies two timescale dependent modes of release of the elastic energy of the membrane.

1.2.2 Sporozoites

Let us now turn our attention to sporozoites that, although not directly associated with the symptoms of malaria, represent the most motile stage of the life cycle, involving the mosquito, the skin and the liver of the host [4, 11]. It was only recognised about a decade ago that sporozoites are injected into the dermis and not directly into the blood stream of the host [5]. Sporozoite migration is essential and represents the first possibility of intervention to stop the parasites within the host.

Sporozoites are cells characterised by an elongated and bent shape: the typical cell is about 10 µm long, 1 µm wide, and has a radius of curvature of about 5 µm [21, 22]. The geometry of sporozoites shapes their trajectories. On a flat substrate, sporozoites describe circular trajectories matching the curvature of the cell and showing a strong chirality. In fact, over 95% of the cells move counterclockwise if observed with an inverted microscope, that mirrors the real image (Fig. 1.3a) [21]. In a three-dimensional environment, such as skin tissue or unstructured gels, sporozoites describe helical trajectories with various amounts of perturbations, depending on the complexity of the environment (see Chapter 2 and [5]).

Sporozoites are gliding cells that neither rely on cilia or flagella to move, nor extend pseudopods [23]. Their migration takes place instead without obvious changes in cell shape but, at the same time, results from a very versatile molecular system, that allows movement on a variety of substrates, ranging from biological tissue to glass surfaces. These observations lead to the hypothesis that sporozoites provide their own receptors for gliding, secreting the appropriate molecular complexes onto their membrane [23, 24]. However, as extensively reported in [24], this hypothesis is still surrounded by a number of fundamental unknowns, such as the nature of the substrate upon which the parasites glide, or the role of the various receptors involved in gliding. In general, studies specifically targeting the details of the gliding machinery are challenging, because different environments imply different topological constraints and, consequently, trigger specific modes of force transduction during migration. It has been experimentally determined that sporozoite motility relies on an actomyosin system localised at the periphery of the cell. Furthermore, actin is also believed to regulate sporozoite adhesion before the onset of gliding [25].

Efforts towards the understanding of the molecular components involved in gliding and their trafficking in the cell are ongoing. It is however known that this elusive molecular setup generates mean cell speeds of about 1-2 $\mu\mathrm{m\,s^{-1}}$, about one order of magnitude above the average migration speed of tissue cells [5, 24]. Given the hypothesis that sporozoites secrete their own receptors and the observation that they move rather smoothly in a variety of environments, the gliding machinery is typically pictured as a conveyer belt system consisting of adhesive protein complexes, that are secreted at the front end of the parasite and are translocated towards the rear end, with the net effect being forward movement of the cell [24, 26].

As discussed in more detail in the following, this is most likely an oversimplification of a very complex system. In fact, there is evidence showing that the conveyer belt must coexist, and possibly compete, with the formation and rupture of dynamic adhesion sites localised along the cell body [27]. These experimental results, highlighting the role of adhesion sites during gliding, are coherent with the current knowledge about other important gliding cells, namely bacteria [28–30]. It is, however, necessary to point out that fundamental differences exist even between gliding systems in different bacteria and that the common principles behind gliding have still to be uncovered [28].

In the next section we provide a summary of the biophysical experiments that have been targeting sporozoite motility and provide the basis for the models that are proposed and discussed throughout this thesis.

1.2.3 Sporozoites: experimental studies

Here we review the biophysical experiments that have been performed on sporozoites, with the aim of uncovering the properties of their propulsion machinery.

Sporozoites were first observed at the end of the 19^{th} century [31], but the first relevant studies on sporozoite motility have appeared only in 1974 [22]. Surprisingly, the first observations showing that active migration of sporozoites in the dermis is actually fundamental for host infection belong to the last decade [4], and have generated a large interest in understanding the details of sporozoite motility. Indeed, to weaken or disrupt sporozoite motility represents a potentially groundbreaking tool for preventive intervention against malaria. In the last decade, the experimental effort aimed at sporozoites, their structure and motility has been improved.

Let us start by considering the current knowledge about the internal structure of sporozoites, for the understanding of which cryogenic electron tomography (Cryo-EM) has proved an effective tool. Cryo-EM allows for the three-dimensional reconstruction of biological samples starting from two-dimensional images acquired at cryogenic temperature (-180°C). It is a valuable tool for the visualisation and understanding of complex structures because it allows for sub-nanometer resolution, without causing artefacts due to staining and fixation as in classic electron microscopy. Using Cryo-EM, it has been possible to find structural reasons for the chirality of sporozoites and to gain information about their motility system [21,32,33]. Figure 1.3b sketches a sporozoite and its internal components. Sporozoites are highly polarised cells, showing a marked difference between the organisation of their front and rear part. The front part is encaged by a number of microtubules (MT), that stop shortly before the nucleus, localised in the centre-rear part of the parasite. Microtubules are connected to the apical polar ring (APR) in a non-uniform manner, that leaves one microtubule isolated from the others (Fig. 1.3c). Furthermore, the APR is tilted, adding to the structural asymmetry of the cell. The cage of microtubules encloses several organelles, called rhoptries (Rho) and micronemes (Mic), that are involved in the secretion

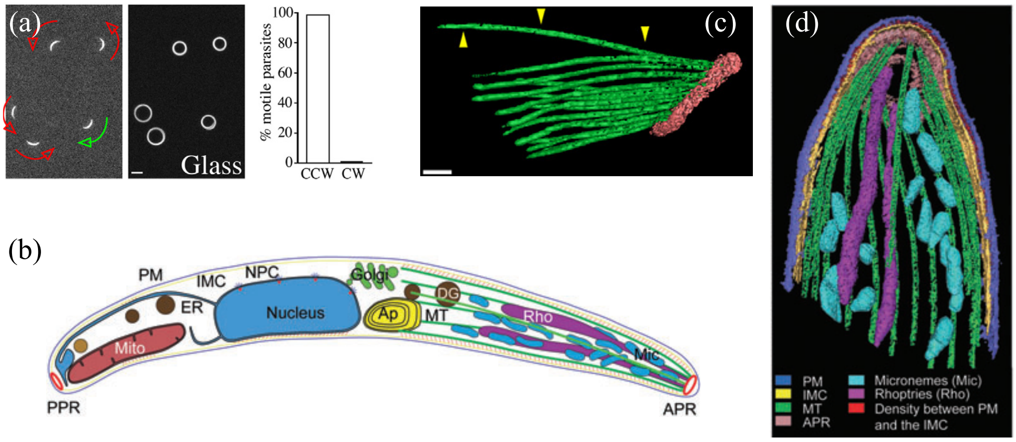

Figure 1.3: (a) Sporozoites are bow-shaped parasites that describe circular trajectories on a flat substrate, showing a strong preference for counterclockwise movement (adapted from [21]). (b) The front part of a sporozoite is encaged by a net of microtubules (MT) that encloses Rhoptries (Rho) and Micronemes (Mic), secretory organelles involved in motility. The nucleus is located in the centre-rear part of the cell (adapted from [32]). (c) Cryo-EM shows that the microtubules are connected to the tilted apical polar ring (APR) in a manner that leaves one microtubule isolated, adding to the structural asymmetry of the cell (adapted from [21]). (d) Cryo-EM image of the front part of a sporozoite showing microtubules, micronemes and rhoptries. The cell is surrounded by several layers, where the gliding machinery is supposedly located (adapted from [32]).

of the various proteins responsible for parasite motility (Mic) and host cell invasion (Rho) (Fig. 1.3d).

A microscopy technique used to investigate the dynamics of adhesion is reflection interference contrast microscopy (RICM, Fig. 1.4a) [27]. RICM exploits polarised light and interference to form an image of an object on a glass surface. The intensity of the output signal quantifies the proximity of the object to the surface. Conveniently, RICM does not require fluorescent probes, but relies entirely on the constructive or destructive interference of the incident with the reflected light. It has been shown in [27] that sporozoites during gliding develop dynamic adhesion sites, primarily localised at the front and rear end of the cell (red and green arrows in Fig. 1.4a). In particular, the rear adhesion site has been linked to deformations of the cell body as a response to stretching induced by the rear end of the cell, that can stick to the substrate impeding translocation. In contrast, the adhesions along the cell body are not as evident, and seem to undergo a considerably faster turnover with some hints of periodicity.

In the same work [27], the authors perform traction force microscopy (TFM) on gliding sporozoites (Fig. 1.4b). TFM exploits the displacement of tiny beads embedded in a gel-like substrate to reconstruct the forces exerted by translocating cells. Results show that the front and rear end of the parasite correspond to regions of enhanced traction force, consistently with the presence of adhesion sites. Since, unfortunately, it was not possible

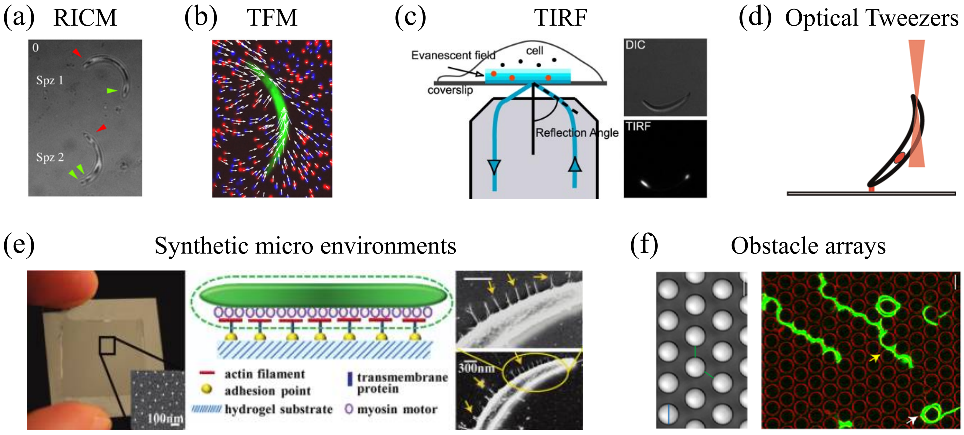

Figure 1.4: (a) RICM exploits the interference of polarised light to reveal the presence of dynamic adhesion sites localised at the front and rear end of the sporozoites (adapted from [27]). (b) TFM allows to quantify the force exerted by gliding sporozoites by quantification of the displacement of beads embedded in a gel-like substrate (adapted from [27]). (c) TIRF microscopy detects the signal from fluorescent probes in the vicinity of a glass surface and proves useful in investigating the dynamics of cell adhesion (adapted from [25]). (d) Optical tweezers provide a confining potential that allows to manipulate the sporozoites, to probe the role of different proteins at various adhesion stages (adapted from [34]). (e) Synthetic micro-environments show that the adhesion dynamics of sporozoites can be controlled by tuning the stiffness of the substrate and the position of the adhesive dots (adapted from [35]). (f) Obstacle micro-arrays approximate the skin environment by forcing the sporozoites to interact with micro-sized pillars (adapted from [36]).

to perform RICM and traction force microscopy at the same time, there are no data linking the adhesion status with traction force. Thanks to this work, we know nonetheless that the conveyer belt system hypothesised before must coexist, possibly compete, with the turnover of adhesion sites localised on the cell body during migration on a flat surface.

Total interference reflection microscopy (TIRF) allows to observe fluorescent probes in the proximity of a glass surface and, consequently, it is a very convenient tool to investigate the dynamics of the contacts between a cell and a substrate. In the case of sporozoites, TIRF has been exploited to determine how they adhere to glass surfaces and study some of the proteins involved in the process (Fig. 1.4c) [25]. Sporozoites adhere on flat surfaces in a stepwise manner, typically developing a contact with the apical or polar end first, then with the other end and, after a final flip over, with the rest of the cell body. It is interesting to note that, between the formation of the first and the second adhesion, the parasite can move actively, while being stuck at one end, for up to several minutes, a process called waving [22]. The same phenomenon is also observed when gliding sporozoites lose adhesion with the substrate [25, 36, 37].

It is also possible to directly manipulate sporozoites using optical tweezers, that exploit a highly focused laser beam to generate an attractive potential that is particularly suitable to trap small spherical beads, but is versatile enough to manipulate the elongated parasites [34]. Confining a sporozoite and pulling on it with the tweezers allows to probe the role of various proteins at different stages of adhesion (Fig. 1.4d). This approach is rather tricky, because of the susceptibility of the cells to the laser power, that must be sufficiently high to compensate for the high motility of the sporozoites but should not damage the molecular mechanisms.

A less invasive experimental approach is represented by synthetic micro-environments, namely substrates of controlled stiffness, patterned with nano-scaled regions that favour cell adhesion (Fig. 1.4e). In [35] the authors control externally the spacing of the adhesion sites and the stiffness of the substrate, showing that the properties of the substrate are sufficient in controlling the modulation and turnover of the adhesion sites during sporozoite migration.

Finally, a purely mechanical approach to the study of sporozoite gliding is represented by PDMS (polydimethylsiloxane) micro-arrays patterned with cylindrical obstacles (Fig. 1.4f). These substrates provide an environment of intermediate complexity: widely more controllable than the skin of the host and more complex than a simple flat surface. Results show that sporozoites in such obstacle arrays describe trajectories dependent on obstacle size and spacing (Fig. 1.4f) [36]. In principle, the complexity of obstacle arrays can be arbitrarily increased and tuned, in order to gradually approximate the relevant features of the skin system. These kind of experiments provide the motivation for the first modelling effort presented in this thesis (Chapter 2) [38].

1.3 Modelling sporozoites

1.3.1 The context: literature

We have seen that sporozoites are naturally curved, highly structured cells, showing marked differences between the internal organisation of their front and rear parts [32]. Sporozoites are adherent, motile cells believed to secrete their own receptors, a feature that presumably is responsible for their ability to ligate to a heterogeneous variety of substrates [24,35]. The molecular trafficking system regulating the adhesion dynamics of sporozoites is not fully understood yet, but it has been shown that it relies essentially on an extremely dynamic actomyosin system [24]. These features relate the sporozoite system to a history of efforts in biophysical modelling, which we briefly review in this section.

Sporozoites share important similarities with adherent animal cells, that in the last decade have been the object of a variety of models (see [39] and references therein). Cell adhesion is possible because of the active generation of mechanical force at the interface between the cell and the substrate by the cytoskeletal dynamics (Fig. 1.5a). The mechanical force itself results from specific, active molecular processes that lead to cytoskeletal reorganisation and the formation of adhesive contacts (adhesion sites) between the cell

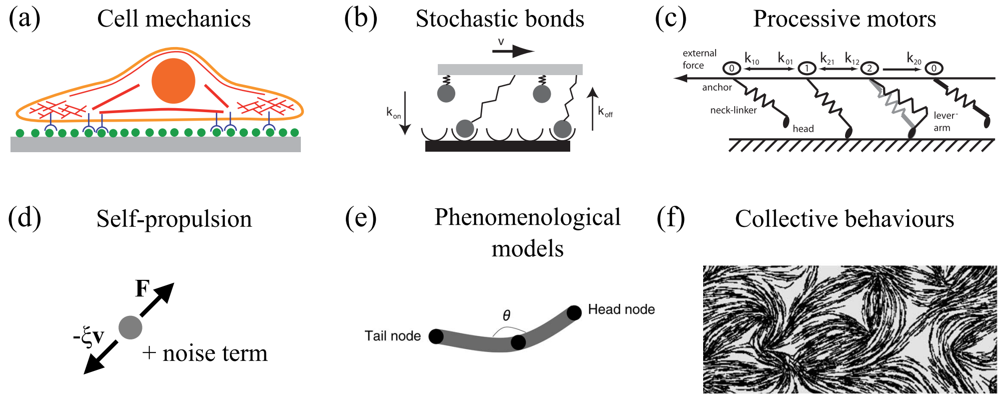

Figure 1.5: (a) Models for adherent animal cells focus on how the cytoskeletal dynamics generates force on a substrate via connections called adhesion sites (figure from [39]). (b) Adhesion to the substrate can be modelled using two surfaces connected by stochastic bonds (figure from [39]). (c) Springs following an energy consuming cycle can be used to model the stochastic generation of propulsion force by active motors (adapted from [40]). (d) Models of self-propelled particles abstract from the internal propulsion machinery, focusing on an effective propulsion force, a viscous term and external or internal noise terms. (e) Details of the system, like cell shape, can be included in the models, for example by approximating an elongated cell as a sequence of springs and beads (adapted from [41]). (f) Ensembles of self-propelled objects can lead to the emergence of collective behaviours (adapted from [41]).

and its substrate. To understand the details of force transmission at the cell-substrate interface, it is necessary to devise appropriate models that describe the internal structure of the cell. In the past years, reference models from soft matter physics, like active gels or active membrane models, have been extended to include the multi-scale character of the problem of cell adhesion [39]. For sporozoites, however, we still lack some of the fundamental knowledge that would allow for a reliable multi-scale model of adhesion. Sporozoites develop dynamic adhesion sites while the cell undergoes translocation. The set of proteins involved in the formation of the adhesions is still a subject of active research and, at the same time, the observation of the cytoskeletal dynamics of these cells is still an open challenge. Actin filaments, for example, are known to be a fundamental component of the motility and adhesive system of sporozoites, but have not been observed yet because of their high polymerisation and depolymerisation rates [32]. It follows that it is now most probably too soon to apply to sporozoites the multi-scale models of adhesion that work well for animal cells, because of the many unknowns on the cytoskeletal and molecular organisation of the system.

Apart from modelling approaches derived from soft matter physics, another way towards the understanding of cell-substrate adhesions is that of multi-contact (or bond) models [42]. Bond models focus on the connection between the cell and the substrate, simply modelling the system as two surfaces connected to each other via spring-like bonds that open or close stochastically. In this context we can distinguish several situations: the two surfaces may or may not move relatively to each other [43–49], and the bonds may be passive (Fig. 1.5b) [42], or they may follow an energy consuming cycle that generates forward propulsion (Fig. 1.5c) [40]. Because sporozoites are motile cells, let us focus on the case of relative motion between the two surfaces. Studies on sliding surfaces connected by simple spring-like bonds represent generic models of sliding friction, that apply to inert as well as biological surfaces. The connecting bonds are usually characterised by a constant on-rate and an elongation dependent off-rate, that typically lead to stick-slip behaviour. Stick-slip is a regime that appears at intermediate driving speeds and corresponds to enhanced fluctuations in the relative speed and traction force between the two surfaces [42, 50–52]. If the model deals with inert surfaces, stick-slip is associated to the transition between static and sliding friction. On the other hand, if bond models represent the cell-substrate interface, stick-slip is associated to an intermediate regime of cell translocation [53, 54].

Traditionally, the focus in this context has been on one-dimensional models, i.e. mutual sliding of the surfaces in a preferred direction. However, because sporozoites glide on a flat surface describing circular trajectories, rotational friction and translational friction must play comparably relevant roles. For this reason, in Chapter 4 we study a model of sliding friction including both these terms, drawing a connection with the case of cell migration.

To take into account that the connection between a sporozoite and its substrate is due to an active system of molecular motors, it is possible to adopt a more biology-related, sophisticated approach. Motors generating a power stroke can be approximated by active springs following an energy consuming cycle that generates forward propulsion (Fig. 1.5c) [40]. Although this is a one-dimensional model, it is a promising microscopic approximation of the conveyer belt system that is thought to be responsible for the forward propulsion of sporozoites.

Abstracting from the dynamics of adhesion, a valid approach is to model motile cells as self-propelled particles in a Brownian framework (among others [55–57]). This method neglects completely the internal structure of the cell that leads to force generation, and considers only the net results, namely a propulsion force in the equation of motion. The cell is approximated as a point-like object, or an object of simple geometry, propelled by a force and or a torque and perturbed by noise terms (Fig. 1.5d) [58, 59]. Noise terms can derive from the propulsion machinery (active, or internal, noise), or from the surrounding environment (passive, or external, noise). Importantly, the two kinds of noise can be distinguished only if the mass of the particle is taken into account (see Sec. 2.7 and [60]). Brownian models are effective to target the average statistical properties of cell motility [61].

In the presence of some experimental knowledge about the system under study, pure Brownian models can be an oversimplified solution. It could, for example, be appropriate to include in the models relevant details about the cell shape or the propulsion system. A relevant example of this kind in the literature is that of *Myxococcus xanthus*, a straight, elongated bacterium that is modelled as a flexible chain of springs and beads (Fig. 1.5e), propelled by a sequence of steps and stochastic relaxations [41, 62]. In these works the authors also include in the models the phenomenology of cell propulsion, like observed reversals in the direction of motion corresponding to alternative translocation methods adopted by the bacteria.

For sporozoites we also adopt a sort of hybrid Brownian approach in Chapter 2, by considering a parasite as a naturally curved rod with bending rigidity. We introduce a propulsion system that, in the absence of perturbations, leads the rod on circular trajectories matching its curvature. We then define an interaction scheme with hard obstacles in a phenomenological manner based on experimental observations [36]. Importantly, with this approach, we introduce in the model a noise source that is confined at the time and location of the interaction with an obstacle [38].

With the addition of interaction terms, Brownian models can also be extended to study the emergence of collective behaviour in systems of many particles [63]. Typically, these systems exhibit transitions from disordered to ordered states, and the transition can be described in terms of one or more system-specific order parameters. An analytical treatment of such systems is possible in the case of sufficiently simple particles and equations of motion [64]. In these situations, it is possible to draw parallels between the behaviour of the out-of-equilibrium system of self-propelled particles and the statistical mechanical treatment of phase transitions in equilibrium systems [63]. Although the formal treatment of self-organisation is limited to mathematically simple systems, the transitions themselves are a much more general feature that can be observed in more phenomenological setups.

Considering again the case of *Myxococcus xanthus*, the bacteria approximated as chains of springs and beads organise in non-trivial patterns if left free to interact according to an experimentally motivated scheme (Fig. 1.5f) [41, 62]. These kind of models for collective phenomena are of special interest for the sporozoite system. Indeed, sporozoites show collective behaviour in preparations of salivary glands of infected mosquitos, arranging in motile whirl-like structures. In Chapter 3 we present an experimentally motivated model to describe and better understand the self-organisation of the sporozoites.

Finally, it is relevant to include data-driven modelling as another approach to the study of cell motility. The quantitative, formal analysis of available experimental data allows to extract relevant, non-obvious features of the system. An example of this kind is [65]. Given that the details of the internal molecular machinery of Dictyoselium are highly uncertain, the authors devise a theoretical model for its motility based on a rigorous statistical analysis of the trajectories of the cells. In Chapter 5 we first connect to this line of thought by proposing a model for sporozoite gliding that links the details of a minimal gliding machinery with the observed stretching of sporozoites as a results of the adhesion of the rear end of the cell [27]. Second, we perform a systematic analysis of time series of sporozoite speed and curvature, providing the basis for future data-driven models.

1.3.2 Outline of the thesis

This thesis groups four independent, experimentally motivated projects, each aimed at investigating different aspects of the motility of Plasmodium sporozoites.

In Chapter 2 we focus on sporozoite migration in the presence of obstacles. This part is motivated by recent experimental work showing that sporozoites migrate in arrays of cylindrical obstacles describing trajectories dependent on the geometrical features of the environment [36, 38]. Such experimental setup is meant to approximate the complex environment that sporozoites encounter upon injection by a mosquito into the skin of a host. To describe migrating sporozoites we adopt a hybrid model of self-propulsion, by explicitly considering the bent shape of the sporozoite, its flexibility and its circular trajectories. We further describe the collisions with the obstacles based on experimental observations. In particular, we postulate that a collision with an obstacle can be solved either deterministically or stochastically. The interplay between these two modes of collision solution shapes the trajectories that the model sporozoite describes under different geometrical conditions.

Chapter 3 focuses on the self-organisation of a dense system of sporozoites. It is motivated by the observation of sporozoites arranged in whirl-like structures in the salivary glands of infected mosquitos, following preparation. In this case, sporozoites are modelled as chains of springs and nodes, are locally flexible and upon mutual collision can either deviate or overlap. In our investigation, we focus particularly on the role of the third dimension, i.e. overlap, in the formation of the whirl-like structures and their stability.

Our third model, presented in Chapter 4, represents a shift from a cell level approach to a microscopic approach. Motivated by gliding sporozoites on a flat surface, for which translational and rotational friction are bound to play a comparable role, we consider a model of stochastic friction involving both terms. Importantly, we include in the model inertia, representing the persistency of cellular movement, and consider a velocity dependent on-rate to account, for example, for different regimes of the propulsion system.

As a final project, we propose in Chapter 5 a deterministic model for sporozoite gliding that connects the details of the gliding machinery to the deformations of the cell. In this case we are motivated by the current hypothesis about the gliding system of sporozoites, namely the competition between a conveyer belt and dynamic adhesion sites localised on the cell body. We complement this data-driven theoretical model with the quantitative analysis of data sets of sporozoite speed and curvature, focusing on the features of the stick-slip behaviour of gliding cells.

All the projects presented in this thesis share a common methodological core. The first step of each project is an assessment of the available experimental knowledge, in order to determine upon which assumptions we should build a theoretical model. Because they represent the first basis of the modelling process, these first assumptions must be firmly grounded in the experiments and should not represent a too harsh constraint. As a second step, we define a theoretical framework including the most relevant phenomenological observations. In order to leave room for further developments in the modelling, we take care to keep the number of parameters low, so that this part is not cluttered by unnecessary or unmotivated assumptions. We devote a particular attention to the study and the analysis of the models in relation to their predictive power. In this context, it is important that the models are simple and solid enough to be robust in the perspective of further refinements, that could stem from the experimental determination of new relevant features of the systems under study.

Credit for the experimental work this thesis is based on goes to the group of Prof. Dr. Friedrich Frischknecht (Heidelberg University Clinics). The people involved are mentioned explicitly at the beginning of each chapter.

2 Malaria parasite migration in structured environments

In this chapter we model the migration of malaria parasites in the presence of obstacles. We propose a geometrical, stochastic model, showing that the interplay between the structural properties of the parasites and the environment is responsible for complex migration patterns.

Sections 2.1 to 2.6 of this chapter are derived from our recently published paper: *Geometrical model for malaria parasite migration in structured environments*, A. Battista, F. Frischknecht and U.S. Schwarz, Phys. Rev. E **90** (2014) [38].

Credit for the experimental work we refer to throughout the chapter goes to the Frischknecht group (Heidelberg University Clinics), in particular to Janina Hellmann, Lucas Schütz, Noa Dahan, Leandro Lemgruber and Miriam Ester.

Section 2.7 is added in order to describe more extensively the theoretical framework within which our model is built. Section 2.8 is added at the end of the chapter in order to present the current efforts and approaches in the analysis of newly designed experiments. This section could not exist without the help and collaboration of Julianne Mendi Muthinja Wietzorrek (Frischknecht group).

2.1 Introduction

The migration of malaria parasites (in the form of sporozoites) in the skin of a vertebrate host is very fast, with an average migration speed exceeding $1\,\mu\mathrm{m\,s^{-1}}$, which is 1-2 orders of magnitude faster than the migration of typical tissue cells [5]. Plasmodium sporozoites are about $10\,\mu\mathrm{m}$ long and about $1\,\mu\mathrm{m}$ wide, depending on the species and stage of maturity [21]. Mature sporozoites are crescent shaped with an average radius of curvature of about $5\,\mu\mathrm{m}$ [22] and move on circular trajectories on a flat substrate, with a strong preference for counterclockwise movement (under an inverted microscope, that mirrors the real image) [22]. In contrast to crawling cells, that extend protrusions to translocate, sporozoites migrate with changes in cellular shape that are limited to their curvature [27]. Sporozoites lack cilia or flagella and therefore are not swimming cells, as for example *E. Coli* [66]. Instead, their type of motion is called *gliding motility* and depends on adhesion between the cell and the substrate. Sporozoites are supposedly propelled by an internal conveyer belt system that translocates adhesive transmembrane proteins from the front to the rear end of the cell, exploiting an evolutionary ancient actomyosin system [24, 26]. In contrast to mammalian tissue cells, however, this adhesion is relatively non-specific as the adhesion receptors seem to bind to many different ligands [35].

The observation of two-dimensional circular movement, together with the fact that, in an unstructured three-dimensional environment, sporozoites tend to move on roughly helical paths, suggest that the movement of sporozoites is strongly determined by their geometrical shape [5, 21, 22, 36, 67, 68]. However, sporozoite trajectories are also highly dependent on the structural properties of their environment. For example, they show different patterns of locomotion in the tail versus the ear of mice, possibly as a result of the different organisation of the extracellular matrix [36]. The role of the environment in sporozoite migration has been previously addressed by experimental studies that have employed micro-fabricated pillar arrays [36]. Similar experimental approaches have been used recently also for other cellular systems, for example the nematode worm *C. Elegans* [69], the amoeba *Dictyostelium* [70], the bacteria *Neisseria gonorrhoeae* and *Myxococcus xanthus* [71], and the eukaryotic parasite causing the sleeping disease, the trypanosome [72]. Migration of sporozoites through arrays with different pillar diameters and spacing revealed complex motion patterns depending on both radius and spacing, highlighting the role of the interplay between the peculiar geometrical features of the parasite and repeated encounters with obstacles [36]. However, a quantitative framework to understand the features of sporozoite migration in complex environments is still missing.

Sporozoite gliding is different from most other types of cell locomotion that have been analysed with mathematical models before, but also shares some instructive similarities. The flow of actin and related molecules driving the conveyer belt system [24, 73] is reminiscent of the flow of actin in keratocytes, that has been studied e.g. within a hydrodynamic framework [74] or phase field models [75]. However, the structural organisation of the actin system in sporozoites is very different and far from understood [76]. The coupling between the sporozoite and the substrate via adhesion molecules is similar to the situation in adherent animal cells, which has been described before e.g. as a slip boundary for an active gel [77, 78], but again the exact details are not known yet. In particular it is unclear how adhesion molecules are injected into and removed from the conveyer belt system, and how they are organised along the body of the sporozoite [27].

Due to the uncertainty regarding the molecular system, it is natural to start with a mathematical analysis at the cellular level. In this framework, active motion in the presence of hard obstacles is often treated using Brownian models for simply shaped and non-deformable particles [55, 79–81]. For more details on this topic we refer the reader to Sec. 2.7. However, in the case of sporozoites, as well as of other cells moving in structured environments [69–72], cell deformations should be taken into account. One instructive example is the bacterium *Myxococcus xanthus*, that is also self-propelled and rod-shaped and that has been described as a flexible chain of beads [41, 82]. While this work investigated interactions between the bacteria, here we address a single but curved object interacting with a given obstacle array. Moreover we do not model the parasite as a chain of beads, but introduce a parametrisation that is computationally less expensive.

In this paper we propose a cell level, geometry-based model for sporozoite migration that takes into account the sporozoite curvature and length, but not its thickness. Our model focuses on adhesion to a solid support and repeated collisions with obstacles. We exclude the explicit modelling of the internal gliding machinery, whose effect, to a first approximation, is to propel the sporozoite forward at a typical speed. Instead, we model the parasite as a self-propelled rod with spontaneous curvature that, in the absence of obstacles, moves with constant speed along a circular trajectory of matching curvature. Motivated by experimental observations, collisions with hard obstacles are solved either by a temporary change in the curvature of the rod or by a random reorientation. Extending our model to three dimensions, we consider the effect of twist and show that both bending and twisting help the parasite to navigate arrays of cylindrical obstacles with the shape of blood vessels. Our analysis demonstrates how the complexity of sporozoite motility in structured environment is shaped by the geometrical and mechanical properties of the parasite, and provides a first quantitative framework to rationalise the experimental results for sporozoites moving in pillar arrays and other structured environments.

2.2 Experimental motivation

We start with the experimental observations underlying our theoretical analysis (more details of our experimental procedures are provided in appendix A of the paper corresponding to this chapter [38]). Sporozoites from the rodent model parasite Plasmodium *berghei* migrating on a two-dimensional flat substrate describe circular trajectories with a radius similar to their own radius of curvature (Fig. 2.1a). Migration in unstructured three-dimensional environments, such as matrigel, leads to perturbed helical trajectories (Fig. 2.1b). Trajectories *in vivo* (e.g. in the ear of a mouse) are more irregular, but still include circular elements with a radius that again seems to correspond to the radius of curvature of the parasite (Fig. 2.1c).

In order to study motility patterns in quantitative detail, micro-fabricated PDMS pillar arrays have emerged as a very useful assay, because it allows us to design the geometrical structure and to perform microscopy that can be easily combined with image processing. The pillars are usually placed in a hexagonal arrangement (Fig. 2.2a(i)). Because sporozoite adhesion is relatively non-specific, no special surface functionalisation or passivation is required. The sporozoites settle between and interact with the pillars, sometimes leading to clear deviations from their unperturbed shape (Fig. 2.2a(ii)). While sporozoites often seem to make contact with a pillar during translocation (Fig. 2.2a), adhesion between the parasite and a pillar is not a requirement to circle around it (Fig. 2.2b). Typical trajectories of P. *berghei* sporozoites in pillar arrays are shown in Fig. 2.2c as overlay of a time series of fluorescent images. Sporozoites can circle around pillars both in a stable

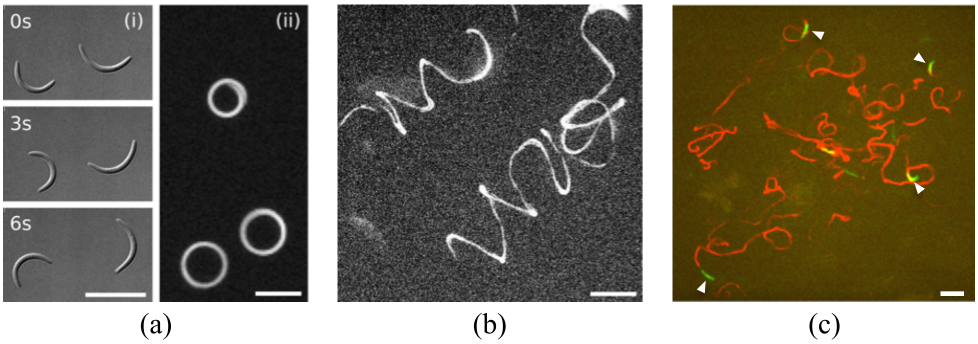

(a) (b) (c)

Figure 2.1: Plasmodium sporozoites are curved gliding parasites that describe environment dependent trajectories. (a) On a two-dimensional substrate sporozoites move on roughly circular trajectories in a counterclockwise direction. (i) Time series of differential interference contrast (DIC) images (time given in seconds). (ii) Overlay of a time series of fluorescent images of three gliding sporozoites. (b) In three-dimensional unstructured gels sporozoites describe perturbed helical trajectories, as shown here with maximum fluorescent projections of two sporozoites migrating in matrigel. (c) *In vivo* trajectories (red) of sporozoites (green, white arrowheads) migrating in the dermis of the ear of a mouse appear more random but circular elements are clearly present. The trajectories are maximum fluorescence intensity projections for 240s. Sporozoites are represented at the start of the imaging in green and pointed to by the white arrowheads. Trajectories, in red, are represented from 5s after the start till the end of the imaging time. Scale bars: 10 µm.

manner (Fig. 2.2c(i)) and in an unstable manner (Fig. 2.2c(ii)). In the second case, the parasite remains attached to the substrate with its back end and probes the environment in a waving manner until it adheres and migrates again with a new orientation. Trajectories can also show distinct linear patterns as in Fig. 2.2c(iii) or be mainly meandering as in Fig. 2.2c(iv).

Although motility patterns of sporozoites in obstacle arrays can be automatically classified using image processing [36, 37], it is difficult to quantify the systematic effect of the structure of the environment on the migration of the single cell because of the inherent variability within a population of sporozoites. Experimental evidence suggests that spontaneous curvature, cell length, bending rigidity and adhesion structure show a strong degree of variability from one sporozoite to the other. For example, Fig. 2.3 shows the broad distribution of spontaneous curvature (details given in Sec. 2.6.1). While this geometrical feature of the sporozoite can be measured relatively easily, most of its other features are not directly accessible, especially not in the context of motility assays. In this chapter we propose a physical model to systematically study the role of the geometrical and mechanical properties of sporozoites during migration in obstacle arrays, which in the future might be helpful to estimate these microscopic properties from macroscopic observations.

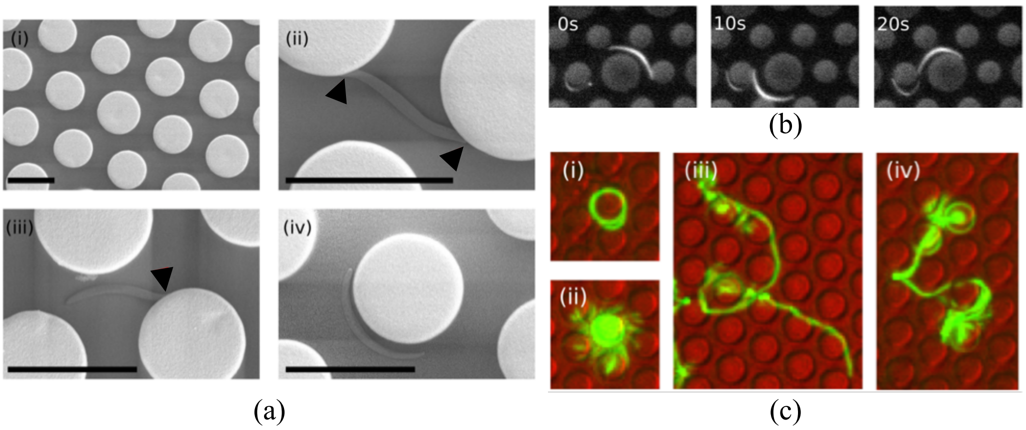

Figure 2.2: (a) Top views by scanning electron microscopy of micro-fabricated arrays consisting of PDMS pillars on a flat PDMS substrate and arranged according to a hexagonal lattice (i). Plasmodium sporozoites migrating in the arrays lie on the substrate and can interact with the pillars: the ends of the parasite can either contact the pillars (black arrowheads) or not (ii-iv). Scale bars: 10 µm. (b) Circling of sporozoites around pillars does not require direct contact. Furthermore, occasional contact does not confine the parasite to the pillar. Numbers indicate time in seconds. Scale bars: 10 µm. (c) Typical trajectories of sporozoites migrating in pillar arrays: circular trajectories (green channel) around pillars (red channel) (i), linear (iii) and meandering (iv) trajectories. In addition, adhesion of sporozoites can also be unstable, leading to a probing phase that ends with migration into a new direction (ii).

2.3 Basic model

2.3.1 Geometrical considerations

Consider a hexagonal lattice of lattice constant l patterned with circles (pillars) of radius ρ, the distance between two nearest neighbours being $d = l - 2\rho$. We model the sporozoite as a bent rod of length L and curvature κ_0 (Fig. 2.4a). We define a set of non-dimensional quantities such that the rod has unit curvature:

$$\widetilde{\rho} = \rho\kappa_0;\;\; \widetilde{d} = d\kappa_0;\;\; \widetilde{l} = 2\widetilde{\rho} + \widetilde{d};\;\; \widetilde{L} = L\kappa_0\;\; . \tag{2.1}$$

Consider the parasite moving on the circle that best fits its shape. In a $(\widetilde{\rho}, \widetilde{d})$ lattice the parasite is said to move steadily if its circular trajectory does not collide with any of the obstacles in the lattice. This is possible in two ways: either the trajectory lies between the pillars (BTW) or it loops around one or more pillars (ARN) (Fig. 2.4a). Conditions for steady movement in the obstacle array are derived from the geometry of the lattice. Circling between the pillars is possible for distances:

$$\widetilde{d} \geq \sqrt{3} - \widetilde{\rho}(2 - \sqrt{3})\;\; , \tag{2.2}$$

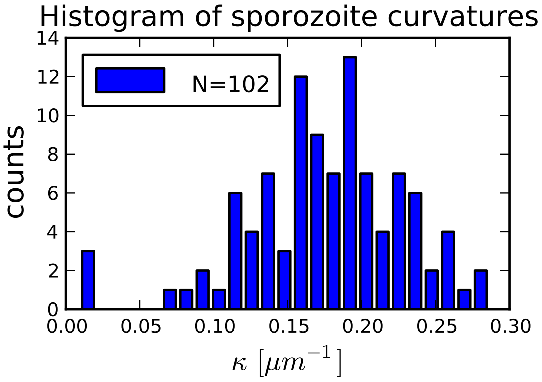

Figure 2.3: Curvature distribution of Plasmodium sporozoites automatically measured from a sample of $N = 102$ cells. The values are widely distributed around curvatures of about $0.2\,\mu\mathrm{m}^{-1}$, corresponding to an average radius of curvature of about $5\,\mu\mathrm{m}$.

while circling around one or more pillars is possible for:

$$\widetilde{d} \geq 1 - \widetilde{\rho} \text{ and } \widetilde{\rho} \leq 1 \ . \tag{2.3}$$

The curves identified above define four regions in the $(\widetilde{\rho}, \widetilde{d})$ plane, delimited by the solid lines in Fig. 2.4b. In region 1 no steady pattern is possible, region 2 allows for ARN patterns, region 3 for both ARN and BTW patterns, while in region 4 only BTW patterns can fit. The dark grey and green points in Fig. 2.4b correspond to the curvature values from the distribution of Fig. 2.3 for typical obstacle array parameters $(\rho = 5, d = 6)\mu\mathrm{m}$ and $(\rho = 4, d = 3)\mu\mathrm{m}$, respectively, as used in experiments [36]. Since a sample of sporozoites does not localise to a unique region of the $(\widetilde{\rho}, \widetilde{d})$ plane, the information on the curvature of the sporozoite is necessary to make predictions about its most likely trajectory. For a typical experiment with the curvature distribution shown in Fig. 2.3, we conclude that both ARN and BTW motility patterns are expected to be observed.

2.3.2 Interaction with the obstacles

Motivated by detailed experimental observations of Plasmodium *berghei* sporozoites migrating in pillar arrays, we divide the interaction with the obstacles in two categories (Fig. 2.5). In the first case, the parasite successfully avoids the pillar via a temporary change in the bending of the cell body. In the second case, the parasite transiently loses adhesion to the substrate to then reattach with a new orientation to resume migration. In the following we formalise these experimental observations using two different descriptions of the interaction between the bent rod and the obstacles: the binary and the statistical interaction schemes, corresponding to a stiff and a flexible rod, respectively. To keep the model simple, we disregard the asymmetry between clockwise and counterclockwise motion, which is expected to be of minor relevance for the case of frequent collisions studied

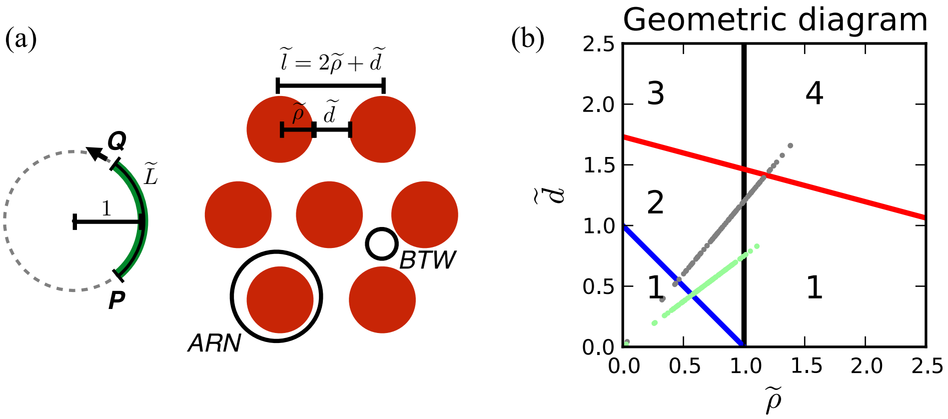

Figure 2.4: (a) Our model parasite is a one-dimensional bent rod that, when unperturbed, describes a circular trajectory on the circle that best fits its shape. Migration of the rod in hexagonal obstacle arrays is characterised by frequent collisions, but two unperturbed stable motility patterns are possible, depending on the obstacle size and distance: circling around one or more obstacles (ARN) and circling between the obstacles (BTW). (b) Geometric diagram identifying the regions of the $(\widetilde{\rho}, \widetilde{d})$ plane, delimited by the solid lines, where ARN and BTW are allowed. In region 1 no steady pattern is possible, region 2 allows for ARN, region 3 for both ARN and BTW, while in region 4 only BTW patterns are possible. The dots correspond to the curvature values from the distribution of Fig. 2.3 for typical obstacle array parameters $(\rho = 5, d = 6)$µm (dark grey) and $(\rho = 4, d = 3)$µm (green) used in experiments [36].

here.

In the binary model the sporozoite is stiff and can move with fixed unit curvature either clockwise or counterclockwise. A collision triggers a check to determine if the configuration symmetric with respect to the tangent in P solves the overlap (Fig. 2.5a, rightmost orange rod). If not, than the parasite reorients by rounding up around P and sampling a random exit angle to resume motion with unit curvature and a probability 1/2 of moving either clockwise or counterclockwise (Fig. 2.5b). The binary model is purely geometrical and avoids changes in curvature, but allows for the two basic responses observed in experiments (deflection and tumbling).

In the statistical model, we allow the parasite to assume a non-natural curvature for a short time in order to solve a collision situation. We consider an interval $I = [-\widetilde{\kappa}, \widetilde{\kappa}]$ of curvatures that the sporozoite can assume in order to avoid an obstacle upon collision. However, only a subset $I_c \subseteq I$ allows the parasite to avoid the obstacle. We assign to each curvature an energy $E(\kappa)$ according to a symmetric double well potential with minima in $\kappa = \pm 1$, so that in general the total bending energy of the rod reads:

$$E_{\text{bend}} = \int_0^{\widetilde{L}} ds\, E(\kappa(s)) = \int_0^{\widetilde{L}} ds\, [(\kappa(s) - 1)(\kappa(s) + 1)]^2 \quad . \tag{2.4}$$

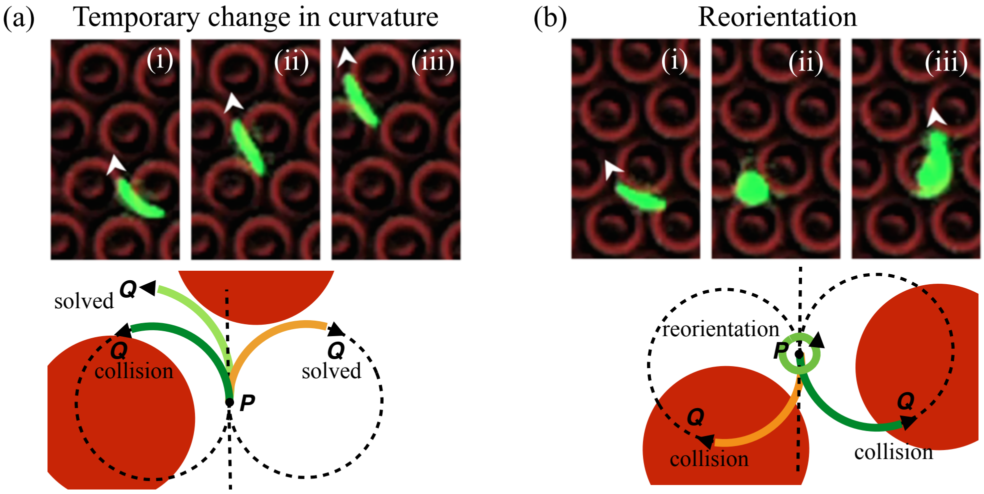

Figure 2.5: We group the interactions between Plasmodium sporozoites and obstacles in two categories. In the first (a), obstacles are avoided via a change in the bending of the cell body. The deformation is temporary: once the collision is solved the rod proceeds its migration with unit curvature, the sign of which is consistent with that of the temporary curvature. The deformed region progressively shifts towards the rear of the rod. (b) In the second interaction mode the collision is solved via a reorientation of the rod, after which migration is resumed with unit curvature and an equal probability of moving clockwise or counterclockwise. Our model thus allows both for changes in the curvature of the rod as well as for random reorientations. The balance between the two modes of interaction depends on the model parameters.

We introduce a temperature via $\beta = 1/(k_\mathrm{B}T)$ to account for the strength of the bending effect. We also assign an energy E_tmb to a reorientation (tumbling) event. We finally distinguish between new curvatures of equal or of different sign. Therefore we introduce σ, the initial sign of the curvature. We then define the partition function $Z(\beta)$ that includes all possible outcomes of the collision event in the statistical model:

$$Z(\beta) = e^{-\beta E_\mathrm{tmb}} + \frac{1}{2}(1 + \sigma\,\mathrm{sgn}(\kappa)) \sum_{\kappa \in I_\mathrm{c}} e^{-\beta E(\kappa)} + \frac{1}{2}(1 - \sigma\,\mathrm{sgn}(\kappa)) \sum_{\kappa \in I_\mathrm{c}} e^{-\beta E_\mathrm{max}} \quad . \tag{2.5}$$

This equation shows that the rod has three possibilities upon collision: it can tumble, it can assume a new curvature with sign σ, or it can assume a new curvature with sign $-\sigma$. New curvatures with the same sign are close to the initial curvature and are weighted by Boltzmann factors. New curvatures of opposite sign must overcome an energy barrier E_max and therefore are treated differently from curvatures with the same sign. The outcome of the collision is chosen stochastically according to the probabilities represented in the partition sum. Independent of this outcome, the resulting parasite deformation is only temporary, meaning that once the collision is solved the rod proceeds its migration with unit curvature. Progressively, the deformed region shifts towards the back of the rod. If the interval I consists only of $\kappa = \pm 1$, we recover the binary model. When I_c is empty, the rod

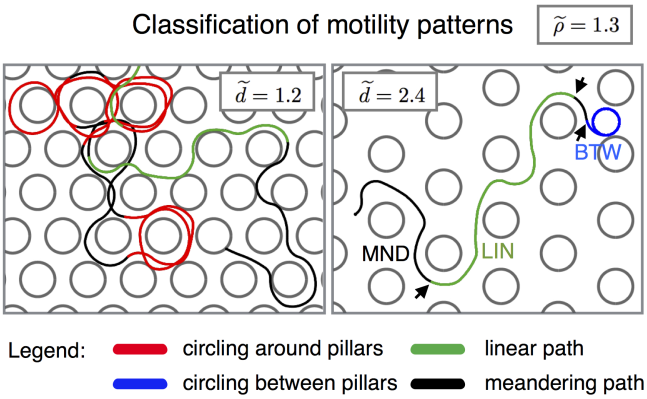

Figure 2.6: Sample output of the algorithm classifying the motility patterns. For each trajectory we isolate paths circling around obstacles (ARN), between obstacles (BTW) and linear paths (LIN); the parts of the trajectory excluded from this categories are classified as meandering (MND). In the right box, the arrows identify the transitions from one pattern to another.

performs a random reorientation, again as in the binary model. The inverse temperature β describes the importance of the energy terms for adhesion and bending versus an equal partitioning between all possible states.

2.3.3 Classification of the trajectories

We analyse the trajectory the parasite describes under the different interaction rules by tracking its rear end P. Using a custom-made MATLAB routine we classify which proportion of the trajectory of P is spent either circling around a pillar (ARN), circling between pillars (BTW), or moving through the lattice in a linear fashion (LIN). Portions of the trajectory not falling in any of these categories are classified as meandering (MND). Sample results of this classification are shown in Fig. 2.6. In the following we analyse the trajectories of the parasite for two representative values of $\tilde{\rho} = 0.7, 1.3$ and a set of distances $\tilde{d} \in [0.2, 3]$ and compare the results with the predictions from the geometric diagram in Fig. 2.4b. The details of our analysis of the trajectories are explained in 2.6.2.

2.3.4 Simulation results

In our model, the parameters β and $E_{\max}$ describe the effects of adhesion and bending. Because at the current stage it is not possible to estimate their values from a microscopic model, we fix their values to $\beta = \log 2$ and $E_{\max} = 1$ as a representative choice for a wide set of parameters that lead to results consistent with the experimental observations. In accordance with experiments, the typical parasite length is set to $\tilde{L} = 2\pi/3$. In the following, each parameter set is studied using $N = 50$ independent simulations. The rod moves with constant unit speed and the trajectory is measured in terms of the non-dimensional arc length s. The rod is discretised in steps $ds = 0.02\tilde{L}$ and each simulation can last until the trajectory is $200\widetilde{L}$ long. For numerical reasons, a simulation is terminated when, at a random reorientation, the distance between P and the obstacle is below $d_{\min} = 0.01\widetilde{L}$.

We start with the condition $E_{\text{tmb}} = +\infty$, which means that the collision with an obstacle is solved by a random reorientation only when none of the possible deformations is able to free the rod. Results of the binary model, corresponding to the limiting case $\kappa = \pm 1$, are represented in Figs. 2.7a and 2.7d. For $\widetilde{\rho} = 0.7$ (Fig. 2.7a) we observe, with increasing $\widetilde{d}$, a dominance of MND, then ARN and finally BTW. The transition from MND to ARN takes place in correspondence with the dashed line, that represents the curve separating region 1 from region 2 in Fig. 2.4b. Similarly, the transition from ARN to BTW begins at the dashed-dotted line, that represents the line separating region 2 and 3 in Fig. 2.4b. For $\widetilde{\rho} = 1.3$ we only observe a transition from MND to BTW, because the obstacle radius is too large to allow for ARN. The transition coincides with the dashed-dotted line, that separates region 2 and 3 in Fig. 2.4b. Results from the binary model therefore agree very well with the predictions from the geometrical phase diagram.

Allowing the rod to change curvature upon collision has the effect of increasing the occurrence of circling for $\widetilde{\rho} < 1$ (Figs. 2.7b and 2.7c). For $\widetilde{\rho} > 1$ the flexibility allows circling and linear patterns where in the binary case only meandering is possible (compare Fig. 2.7d with Figs. 2.7e and 2.7f). Figures 2.7b and 2.7e refer to a rod that can choose curvatures from the interval $I^{(1)} = [-1, 1]$, while Figs. 2.7c and 2.7f correspond to a rod choosing from the wider interval $I^{(2)} = \left[-\left(\pi/\widetilde{L} + 1/2\right), \left(\pi/\widetilde{L} + 1/2\right)\right]$. Since in this last case the rod can increase its absolute curvature to solve a collision, BTW competes with ARN at lower $\widetilde{d}$ than with $I^{(1)}$, leading to increased MND and BTW pattern and a faster decrease of ARN.

Figure 2.7e shows a dip in the ARN curve. In fact, for pillar radii $\widetilde{\rho} > 1$ circling can take place only if the rod is flexible, at the cost of continuous collisions with the obstacle and adjustments of the curvature of the rod. Three different situations can be isolated (Fig. 2.8). The distance $\widetilde{d}$ is very small (Fig. 2.8a): in this case the adjustment in the curvature of the rod depends on both *pillar 1* and *pillar 2*. For intermediate values of $\widetilde{d}$ (Fig. 2.8b) the change in curvature depends only on *pillar 1*, but *pillar 2* interferes with the trajectory of the rod after the curvature change. As a consequence, circling around *pillar 1* is possible only at the cost of separate collisions with both *pillar 2* and *pillar 1*. For $\widetilde{d}$ large enough (Fig. 2.8c) *pillar 2* does not interfere with the trajectory of the rod after the curvature change due to the collision with *pillar 1*. Therefore, circling around *pillar 1* does not require collisions with any other pillar.

Figure 2.7f does not show any dip in the ARN curve; this is due to the interval $I^{(2)}$ being wider than $I^{(1)}$. The possibility of increasing the absolute curvature offers more possibilities to solve the collision at intermediate distances without randomly reorienting (Fig. 2.8). In addition, BTW competes with ARN at lower $\widetilde{d}$ than in the case of $I^{(1)}$, thereby favouring the decrease in the circling frequency at larger $\widetilde{d}$.

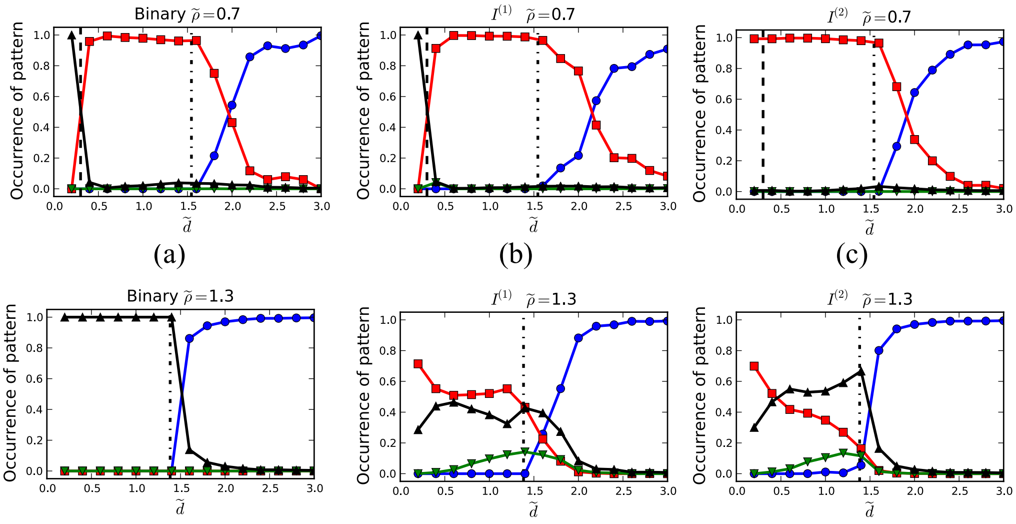

(a) (b) (c)

(d) (e) (f)

Figure 2.7: Occurrence of motility patterns for stiff and flexible rods. The red (squares), blue (circles) and green (downward triangles) solid lines denote the ARN, BTW and LIN patterns respectively. The black solid line (upwards triangles) refers to MND patterns. (a) For the binary model with $\widetilde{\rho} = 0.7$ the distance dependence of the motility patterns is characterised by a transition from MND to ARN to BTW. The transition from ARN to BTW is conserved also when the rod is flexible (b,c), but the transition from MND to ARN is lost in (c), when the rod can increase its absolute curvature to avoid an obstacle. The dash-dotted and dashed lines represent the lines in Fig. 2.4b separating region 1 from 2 and region 2 from 3 for $\widetilde{\rho} < 1$. The transition from one motility pattern to another takes place as predicted by Fig. 2.4b. (d) The binary model for $\widetilde{\rho} = 1.3$ only allows for a transition from MND to BTW. Flexible rods (b,c) can also circle around the obstacles and move linearly in the array. The dash-dotted line represents the line in Fig. 2.4b separating region 1 from 4 for $\widetilde{\rho} > 1$. It corresponds to the onset of BTW patterns for both stiff and flexible rods.

We next consider the case of a finite E_{tmb}, which means that the parasite can solve collisions by tumbling even when they could be solved by a deformation. The effect of E_{tmb} is relevant in conditions where collisions between the rod and the obstacles are frequent and the possible solutions limited, i.e. for $\widetilde{\rho} > 1$ and low $\widetilde{d}$ (Fig. 2.9 for $I^{(1)}$). Low values of E_{tmb} favour random reorientations, particularly at low distances. Consequently, meandering paths grow at low $\widetilde{d}$ and the dip in the ARN disappears (Figs. 2.9a and 2.9b), while it is still present at higher E_{tmb} (Fig. 2.9c).

2.4 Model extensions

2.4.1 Anisotropic obstacle arrays

We introduce an anisotropy in the obstacle array by assuming that half of the contour of the obstacle can trigger a random reorientation of the rod upon collision. Collisions

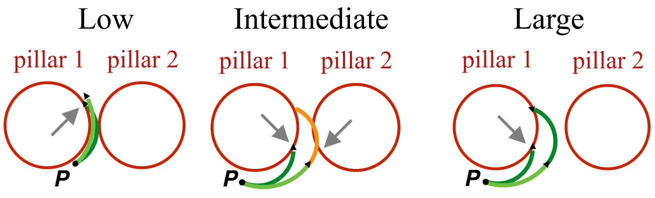

(a) (b) (c)

Figure 2.8: Collisions of the parasite with the obstacles depending on the lattice spacing. (a) At small distances a collision causes the rod to deform based on *pillar 1* and *pillar 2*. (b) Intermediate distances force the rod to interact separately with *pillar 1* and *pillar 2*, while at large distances (c) the rod does not interact with *pillar 2*. Since intermediate distances correspond to an augmented collision frequency, random reorientations are also more frequent and circling around the obstacles is less likely than at small or large distances.

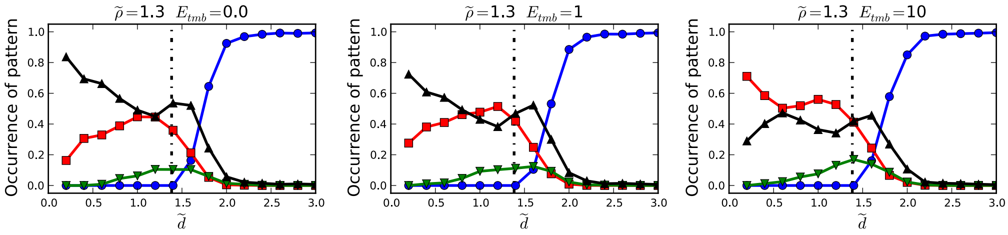

(a) (b) (c)

Figure 2.9: Effect of a finite E_{tmb} on the migration patterns of a flexible rod ($I^{(1)}$). The red (squares), blue (circles) and green (downward triangles) solid lines denote the ARN, BTW and LIN patterns respectively, the black solid line (upward triangles) refers to MND patterns. The dash-dotted line represents the onset of BTW as predicted by Eq. (2.2). (a,b) Low values of E_{tmb} allow the rod to solve a collision via a random reorientation even if the obstacle could be avoided via a change in curvature. This favours meandering patterns at low $\tilde{d}$, when collisions with the obstacles are most frequent. (c) High values of E_{tmb} restore the changes in the bending of the rod at low $\tilde{d}$ (Fig. 2.7e, Fig. 2.8a).

occuring at the reorienting contour (black in Fig. 2.10a) are assigned a tumbling energy $E_{\text{tmb}} = -20$, while we set $E_{\text{tmb}} = 20$ otherwise. To analyse the effect of the anisotropy on the trajectories we divide the lattice in 6 sectors, each $\pi/3$ wide, and measure the fraction of the simulated trajectories that terminate in each of them. The sectors are centered at the starting point of each trajectory; in Fig. 2.10a they are centred on the obstacle to emphasise the connection with the natural directions of the lattice.

The effect of the reorienting contour is pronounced for $\tilde{\rho} > 1$, that is when the rod can circle around an obstacle only via continuous collisions and curvature adjustments. Under the obstacle configuration of Fig. 2.10a the rod is more likely to end up in *sector 2*, represented by the red line (square markers) in Fig. 2.10b (curvature interval $I^{(1)}$). In contrast, no sector stands out when we analyse the location of the end points in an isotropic obstacle array (Fig. 2.10c). The directionality in the migration induced by the

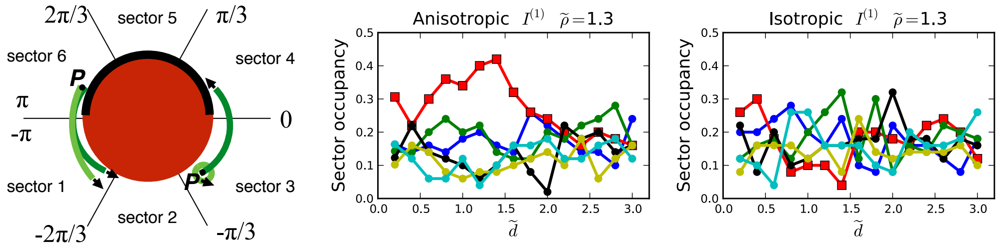

(a) (b) (c)

Figure 2.10: (a) An anisotropic obstacle array consists of pillars that have half of the contour (black) triggering a random reorientation of the rod, while the other half favours changes in the bending of the rod. We divide the lattice in sectors corresponding to the natural directions of the lattice in order to quantify the directionality imposed by the anisotropy on the trajectories. (b,c) Fraction of trajectories that end up in each of the sectors defined in (a). Sectors from 1 to 6 are plotted, in order, in blue, red, green, black, yellow and cyan. Sector 2 can be distinguished by the square markers. Anisotropic obstacle arrays (b) favour the occupancy of sector 2 (red line, square markers), whereas no sector is preferred in the isotropic case (c). The anisotropic obstacle array induces directionality because it renders less likely for the rod to move from a non-coated to a coated region than the other way around.

anisotropy in the pillar array can be explained with the help of Fig. 2.10a. A rod moving from the reorientation-triggering region to a normal region of the obstacle collides with it in the normal region and solves the interaction via a deformation. On the contrary, a rod that moves from the normal region to the reorientation-triggering region collides with the part of the pillar that forces a random reorientation. Since the centre of the random reorientation is the rear end P, the random reorientation takes place close to the normal region of the obstacle. Effectively, this feature renders less likely for the rod to move from a normal to a reorientation-triggering region than the other way around, thereby leading to the observed directionality.

2.4.2 Heterogeneous obstacle arrays

Let us consider environments with obstacles of two different radii, as in Fig. 2.11a. In the following we will refer to the outer (more common) pillar radius as $\widetilde{\rho}$, while the inner, less common pillar radius is labeled $\widetilde{\rho}_{\mathrm{b}}$. We refer to the distance between two neighbouring outer pillars as $\widetilde{d}$.

Geometrical considerations analogous to those for the homogeneous obstacle array allow us to state that the rod moves steadily in the $(\widetilde{\rho}, \widetilde{\rho}_{\mathrm{b}}, \widetilde{d})$ lattice if it can circle between the pillars (BTW), around the outer pillar (ARN) or around the inner pillar (ARN$_{\mathrm{b}}$) (Fig. 2.11a). The pattern ARN$_{\mathrm{b}}$ is possible for $\widetilde{\rho}_{\mathrm{b}} < 1$. The condition on $\widetilde{d}$ for ARN$_{\mathrm{b}}$ to take place is $\widetilde{d} \geq 1 - \widetilde{\rho}$. The pattern ARN is possible for $\widetilde{\rho} < 1$, while the corresponding

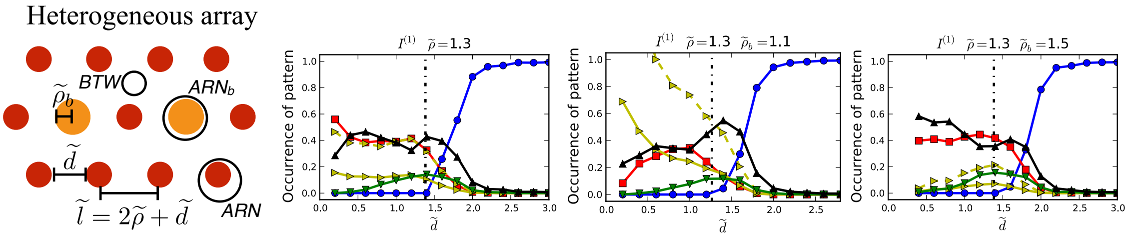

(a) (b) (c) (d)

Figure 2.11: (a) Heterogeneous arrays include obstacles of two different radii, $\widetilde{\rho}$ and $\widetilde{\rho}_\mathrm{b}$; $\widetilde{\rho}$ is three times more common than $\widetilde{\rho}_\mathrm{b}$; $\widetilde{\rho}$ can be smaller or larger than $\widetilde{\rho}_\mathrm{b}$. Stable motility patterns for a bent rod in the lattice are circling between obstacles (BTW) or circling around $\widetilde{\rho}$ or $\widetilde{\rho}_\mathrm{b}$ (ARN and ARN$_\mathrm{b}$, respectively). (b,c,d) Occurrence of motility patterns for a flexible rod ($I^{(1)}$) in heterogeneous obstacle arrays. The red (squares), yellow (right triangles), blue (circles), green (downward triangles) and black (upward triangles) solid lines denote, in this order, ARN, ARN$_\mathrm{b}$, BTW, LIN and MND patterns. The dashed yellow line (right triangles) corresponds to three times the frequency of ARN$_\mathrm{b}$. (b) If $\widetilde{\rho} = \widetilde{\rho}_\mathrm{b}$ the occurrence of ARN reflects $\widetilde{\rho}$ being three times more common than $\widetilde{\rho}_\mathrm{b}$. This correspondence is broken when $\widetilde{\rho} \neq \widetilde{\rho}_\mathrm{b}$ in (c) and (d), because the rod associates more often with obstacles that represent a better geometrical fit.

conditions on $\widetilde{d}$ are:

$$\widetilde{d} \geq 1 - \widetilde{\rho} \qquad \text{for } \widetilde{\rho}_\mathrm{b} \leq \widetilde{\rho}\ , \tag{2.6}$$

$$\widetilde{d} \geq 1 - 2\widetilde{\rho} + \widetilde{\rho}_\mathrm{b} \qquad \text{for } \widetilde{\rho}_\mathrm{b} > \widetilde{\rho}\ . \tag{2.7}$$

Finally, BTW can take place for:

$$\widetilde{d} \geq \frac{1}{2}\left[\sqrt{3}(1+\widetilde{\rho}_\mathrm{b}) + \sqrt{4(1+\widetilde{\rho})^2 - (\widetilde{\rho}_\mathrm{b}+1)^2}\right] - 2\widetilde{\rho} \qquad \text{for } \widetilde{\rho}_\mathrm{b} \leq \widetilde{\rho}\ , \tag{2.8}$$

$$\widetilde{d} \geq \sqrt{3} - \widetilde{\rho}(2-\sqrt{3}) \qquad \text{for } \widetilde{\rho}_\mathrm{b} > \widetilde{\rho}\ . \tag{2.9}$$

We now investigate how the trajectories of a flexible rod (curvature interval $I^{(1)}$) in a heterogeneous pillar array differ from those in a homogeneous array. In order to do that, we adapt the MATLAB routine for trajectory classification to distinguish circling around the two different kinds of pillars. As a control, we apply the routine to a flexible rod ($I^{(1)}$) with $E_\mathrm{tmb} = +\infty$ in a homogeneous pillar array (Fig. 2.11b). Coherently with the homogeneity of the array, the occurrence of circling around $\widetilde{\rho}_\mathrm{b}$ is $1/3$ of the occurrence of circling around $\widetilde{\rho}$. The deviations between the dashed yellow line (right triangular markers), that is three times the occurrence of circling around $\widetilde{\rho}_\mathrm{b}$ and the red line (square markers, circling around $\widetilde{\rho}$) are due to finite statistics effects.

Figures 2.11c and 2.11d show the analysis of the patterns for the two pillar pairs $(\widetilde{\rho}, \widetilde{\rho}_\mathrm{b}) = (1.3, 1.1)$ and $(\widetilde{\rho}, \widetilde{\rho}_\mathrm{b}) = (1.3, 1.5)$. In both cases, all the pillar radii exceed the radius of

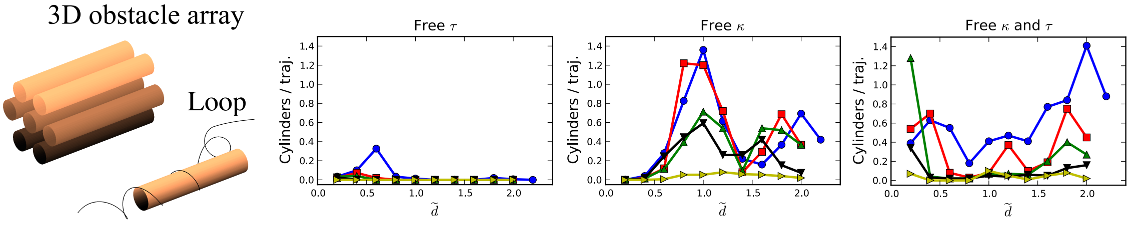

(a) (b) (c) (d)

Figure 2.12: (a) Three-dimensional obstacle arrays consist of a identical cylinders arranged according to a hexagonal lattice. A bent and twisted rod that moves in the array on a helical path is deformed and deviated by the interaction with the obstacles and can as a result loop around the cylinders. (b,c,d) Mean number of cylinders per simulated trajectory involved in one or more looping events. The blue (circles), red (squares), green (upward triangles), black (downward triangles) and yellow (right triangles) curves refer, respectively, to $\widetilde{\rho} = 0.6, 0.7, 0.8, 0.9$ and 1. Looping is deterred by variations in the torsion of the rod (b), but is favoured at smaller radii for rods with a flexible curvature, as in (c) and (d).

curvature of the rod, therefore making circling around any of the pillars possible only at the cost of continuous interactions and adjustments of the rod's curvature. Focusing on the circling patterns around each of the two available radii, we see that the rod associates preferably with the pillars that have the curvature closest to 1, avoiding the other option. In other words, the rod spends more time in the regions of the pillar array that represent a better geometrical fit.

2.4.3 Three-dimensional obstacle arrays

In three dimensions, we have to consider not only bending, but also twisting as a fundamental deformation mode of the parasite. We extend our model to three dimensions by adding a twist to the bent rod with the introduction of a non-dimensional torsion parameter $\widetilde{\tau}_0$. Motivated by the interaction between sporozoite and blood vessels, as an obstacle array we now consider a hexagonal lattice of hard cylinders of radius $\widetilde{\rho}$ (Fig. 2.12a). The unperturbed trajectory of the rod is assumed to be a helix with unit curvature and torsion $\widetilde{\tau}_0$ so that, in terms of the non-dimensional arc-length s, a trajectory around the z axis is expressed as:

$$\mathbf{h}_{\widetilde{\kappa},\widetilde{\tau}}(s) = \begin{pmatrix} \frac{1}{1+\widetilde{\tau}_0^2} \cos\left(s\sqrt{1+\widetilde{\tau}_0^2}\right) \\ \frac{1}{1+\widetilde{\tau}_0^2} \sin\left(s\sqrt{1+\widetilde{\tau}_0^2}\right) \\ \frac{s}{\sqrt{1+\widetilde{\tau}_0^{-2}}} \end{pmatrix} . \tag{2.10}$$

The three-dimensional equivalent of ARN is a helical trajectory looping around a cylindrical obstacle.

For simplicity we consider only positive curvatures and torsions. In order to avoid overly expensive computations, we moreover use the zero temperature limit ($\beta \to \infty$), which constrains the system to its minimal energy states. Let us consider a set of curvatures $I = [\widetilde{\kappa}_{\min}, \widetilde{\kappa}_{\max}]$ and a set of torsions $J = [\widetilde{\tau}_{\min}, \widetilde{\tau}_{\max}]$ that the rod can assume in order to avoid a cylinder upon collision. To each configuration of the rod we assign an energy E:

$$E = \int_0^{\widetilde{L}} ds\, [E_\kappa(\kappa(s)) + E_\tau(\tau(s))] = \int_0^{\widetilde{L}} ds\, [(\kappa(s) - 1)^2 + \alpha(\tau(s) - \widetilde{\tau}_0)^2] \ , \tag{2.11}$$

where α is a coefficient defining the relative contribution of the curvature and torsion energy terms. Similarly to the two-dimensional case (Eq. (2.5)) we define the partition function:

$$Z(\beta) = \sum_{\kappa \in I} \sum_{\tau \in J} e^{-\beta[E_\kappa(\kappa(s)) + E_\tau(\tau(s))]} = \sum_{\kappa \in I_\mathrm{c}} \sum_{\tau \in J_\mathrm{c}} e^{-\beta[E_\kappa(\kappa(s)) + E_\tau(\tau(s))]} \ . \tag{2.12}$$

The pair $(\widetilde{\kappa}, \widetilde{\tau})$ that solves a collision is the one minimising E in $I_\mathrm{c} \times J_\mathrm{c}$.

We choose $\widetilde{L} = 2\pi/3$, $\alpha = 1$ and $\widetilde{\tau}_0 = 0.5$. Each parameter set is supported by $N = 150$ independent simulations when the rod is flexible in the curvature or in the torsion only, by $N = 100$ when both curvature and torsion can vary. The rod is discretised in steps $ds = 0.02\widetilde{L}$ while each simulation can last until the trajectory is $200\widetilde{L}$ long. A simulation is terminated if no $(\widetilde{\kappa}, \widetilde{\tau})$ configuration allows the rod to solve the collision. The intervals for curvature and torsion are $\left[0, 2\pi/\widetilde{L}\right]$ and $\left[0, \sqrt{(2\pi/\widetilde{L})^2 - 1}\right]$ respectively.

We compare the trajectories of rods that are allowed to solve collisions by changing only their curvature, only their torsion, or both. Trajectories are characterised by the number of cylindrical obstacles involved in at least one looping event (Fig. 2.12a). We find that looping around the obstacles is favoured when the rod is allowed to change its curvature upon collision, but is suppressed when only the torsion is allowed to change (Figs. 2.12b and 2.12c). When both curvature and torsion are variable, the rod can loop around the obstacles also in very crowded environments (Fig. 2.12d).

2.5 Discussion

Fast and effective sporozoite migration in the host skin is essential to ensure successful transmission of malaria [5,83,84]. Starting from the striking observation that the sporozoite stage is the only phase of the life cycle of the malaria parasite in which the cells are crescent-shaped [22], we have studied the consequences of this peculiar geometry for sporozoite motion in structured environments. Existing studies addressing sporozoite motility have mainly focused on the molecular mechanisms underlying the propulsion machinery [23, 24]. Here we take a more macroscopic viewpoint and build on previous work that has investigated experimentally the migration of sporozoites in pillar arrays [36]. No theoretical study of the mechanical interplay between the parasite and the environment has, to our knowledge, been presented so far. In this work we have used geometrical arguments and stochastic computer simulations to analyse sporozoites as self-propelled and curved rods. We have focused on migration in arrays with circular or cylindrical obstacles because of our focus on geometrical determinants.

For arrays of identical circular obstacles, the system is most interesting when the obstacles have radii larger than one, so that the bent rod, that has unit curvature, can associate with the obstacles only at the cost of continuous collisions. In this case, the migration patterns of flexible parasites are much richer than those of stiff parasites. Flexible parasites can associate to the obstacles and also move linearly in the lattice where, under the same conditions, stiff parasites can only collide and reorient, resulting in meandering patterns (Figs. 2.7d, 2.7e and 2.7f). A flexible parasite can solve its collisions via a change in curvature, therefore reducing the frequency of random reorientations and describing a trajectory that in general is more stable and smoother.

Flexible parasites are sensitive to anisotropies in the obstacle array (Fig. 2.10a), that trigger directional movement (Fig. 2.10b). This finding provides an interesting experimental perspective. In fact, selectively coated obstacles offer a simple coupling between mechanical and chemical properties in sporozoite motility. Assays of this kind are in principle experimentally realisable [85], provided a suitable inhibitor of adhesion to the substrate and the pillars is used. For example, polyethylene glycol (PEG) has been used previously to prevent sporozoite adhesion [35]. Such a system would contribute to the validation and improvement of the model, in addition to further help the understanding of sporozoite motility in controlled environments and in the presence of an elementary anisotropy. Indeed, one could envision experimental setups of intermediate complexity, for example arrays of soft elastic pillars, that could give information on the forces involved in collisions. Insights from such systems would then help to quantitatively analyse sporozoite motility *in vivo*.

We have further used our model to analyse the effect of obstacles of different sizes (Fig. 2.11a) on the trajectories of the rod. Our results show how the sporozoite statistically associates with preference to the obstacles that provide a better fit to its shape (Fig. 2.11). It is tempting to interpret this result *in vivo*, when the sporozoite glides through the dermis of the host aiming at a blood capillary. The ability to spend more time around structures of matching size could help the parasite in the search for a blood capillary to invade. Surprisingly, the typical radius of a blood capillary is about 8-10 µm, very close to the typical radius of curvature of sporozoites [22], that are also observed to loop around blood vessels before invading them [5].

As a last step, we have extended the model to account for parasite migration in three-dimensional obstacle arrays (Fig. 2.12a). In this case, the parasite is both bent and twisted and moves, if unperturbed, on a helical trajectory. Collisions with the cylindrical obstacles deviate the rod and allow for the trajectory to loop around them (Fig. 2.12a). This feature is intriguing, in that it closely resembles the circling of sporozoites around blood vessels *in vivo* [5]. Our findings reveal that flexibility in the curvature of the parasite is essential for looping to take place. Torsional flexibility alone does not allow for looping, but combined with curvature variations boosts looping in very packed environments (Fig. 2.12). We speculate that sporozoite motility *in vivo* and the association to blood capillaries is greatly favoured by the ability of the parasite to adapt its curvature and torsion based on the structure of the surrounding environment. New techniques to custom design three-dimensional micro-environments [86] represent a high potential for further experimental studies of sporozoite migration.

To conclude, we have shown that sporozoites migrating in complex environments can be efficiently modelled as self-propelled bent (and, in three dimensions, twisted) rods. The flexibility in the bending of the rods facilitates migration in obstacle arrays that do not represent a good geometrical fit. Our focus on cell shape and on the details of the interaction with the obstacles shows that much of the complexity observed in experiments studying sporozoite migration [36] can indeed stem from the geometrical and mechanical properties of the system. Using three-dimensional cylindrical obstacles we have shown that trajectories can loop around them, suggesting a prominent role of the geometrical properties of sporozoites also during migration in the skin of the host, that is successful if it terminates with the finding and invasion of a blood capillary. Our work provides a theoretical framework to analyse future experiments in a quantitative manner.

We finally note that our modelling approach, focusing on basic geometrical and mechanical properties, is not limited to the study of sporozoite motility. In fact, it could be used for the study of other motile cells that undergo temporary shape changes during gliding, for example other apicomplexa such as *Toxoplasma gondii* [87] or gliding bacteria [28].

2.6 Classification of curvatures and motility patterns

2.6.1 Curvature measurements

We have measured the curvatures of Fig. 2.3 starting from images of fluorescent sporozoites on a flat substrate. We have used MATLAB routines to extract the morphological skeleton of each cell. We have then computed the radius of the circumcircle of all the triangles that can be built using the end points of the skeleton as two of the vertexes. The curvature of the parasite is defined as the inverse of the average of the circumcircle radii.

2.6.2 Two-dimensional obstacle arrays

To analyse the motion of a bent rod in an obstacle array we study the positions of its rear end P. The trajectory of P is continuous everywhere, except when a random reorientation takes place. In this case, the bent rod rounds up with centre P and uniformly samples an exit angle, from which it resumes migration with unit curvature and a probability 1/2 of moving either clockwise or counterclockwise. The maximum length required for the point P to lose memory of the rounding-up is $\widetilde{L}$.

The analysis of a trajectory T begins with a check for random reorientations and the exclusion of the $\widetilde{L}$ long paths following them. Let n_r be the number of random reorientations in T, so that there are at most n_r+1 continuous paths T_i left to be analysed independently. Within each T_i, we distinguish between linear (LIN) paths, paths circling between pillars (BTW), around a pillar (ARN) as well as meandering paths (MND). In the case of arrays with obstacles of two different radii we distinguish circling around each of the two kinds (ARN and $\mathrm{ARN_b}$).

We define minimum lengths for the continuous paths T_i to be possibly classified as LIN, BTW or ARN. Paths longer than $L_{\mathrm{LIN}} = 8\widetilde{L}$ are considered for LIN classification. Paths longer than $L_{\mathrm{BTW}} = 2\pi/\widetilde{\kappa}_0$ are considered for BTW classification. Paths longer than $L_{\mathrm{ARN}} = 3\pi \max(1/\widetilde{\kappa}_0, \rho')$ are considered for ARN classification. For homogeneous arrays, $\rho' = \widetilde{\rho}$, while for heterogeneous arrays $\rho' = (\widetilde{\rho} + \widetilde{\rho}_{\mathrm{b}})/2$. The default curvature of the rod $\widetilde{\kappa}_0$ is 1 with our choice of non-dimensional quantities, but is explicitly written here for clarity purposes. Paths T_i shorter than $\min(L_{\mathrm{LIN}}, L_{\mathrm{BTW}}, L_{\mathrm{ARN}})$ are classified as MND. Distinction between LIN, BTW and ARN paths takes place independently. Possible overlaps are taken care of as a final step.

2.6.3 Circling between pillars

We compute the centre of mass CM of each continuous piece of length L_{BTW} of a trajectory T_i. The segment is classified as BTW if CM is outside the pillars, its distance from the closest pillar is larger than $\widetilde{\kappa}_0^{-1}$ and $\langle |T_i - \mathrm{CM}|^2 \rangle$ is below a user-defined threshold that we set to $t_{\mathrm{BTW}} = 0.1/\widetilde{\kappa}_0$.

2.6.4 Circling around pillars

For each continuous piece of length L_{ARN} of a trajectory T_i we compute the centre of mass CM. The segment is classified as ARN in two cases. (a) CM is outside the pillars, its distance from the closest pillar is below $\widetilde{\kappa}_0^{-1} - 2\widetilde{\rho}^*$ and $\langle |T_i - \mathrm{CM}|^2 \rangle$ is below a user-defined threshold t_{ARN}. (b) CM is inside a pillar and $\langle |T_i - \mathrm{CM}|^2 \rangle < \mathrm{t_{ARN}}$. In both cases, we choose $t_{\mathrm{ARN}} = 0.3/\widetilde{\kappa}_0$. For homogeneous pillar arrays $\widetilde{\rho}^* = \widetilde{\rho}$, while for heterogeneous arrays $\widetilde{\rho}^*$ is the radius of the pillar that the parasite is circling around.

2.6.5 Linear

For each continuous piece of length L_{LIN} of a trajectory T_i we compute the elongation as the ratio between the end-to-end distance and L_{LIN}. The segment is classified as LIN if the elongation is above the user-defined threshold $t_{\mathrm{LIN}} = 0.8$.

All the regions that have not been classified up to now are classified as MND. We take care of the regions that have been classified as more than one pattern by ranking ARN

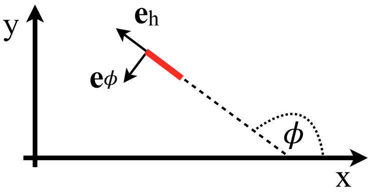

Figure 2.13: Representation of the heading vector $\mathbf{e}_\mathrm{h}$ and the polar orientation vector $\mathbf{e}_\phi$, associated with a short, stiff rod with preferred direction of movement and varying orientation.

before BTW, which in turns ranks before LIN.

2.7 Brownian approach to self-propulsion

So far in this chapter we have presented, analysed and discussed the implications of a model for sporozoite motility focused on the geometrical features of the parasite and the environment. We have taken into account the curvature of the parasite as a key component of the model, and we have implemented a detailed interaction scheme firmly grounded on experimental observations.

As can be rightfully expected, our approach is neither the first nor the only possible one. In particular, a first Brownian model for sporozoite migration was realised in the Schwarz group (Heidelberg University) and is reported in detail in [88]. Brownian models represent, in fact, a common approach to the description of self-propelled particles and, in particular, of actively motile microorganisms. The Brownian framework typically models a self-propelled particle without specifically including its shape and volume, while the focus is instead on the preferred direction of motion determined by a propulsion force. At the same time, the interaction with the environment is typically approximated by random forces [55–57, 89]. This approach is therefore more abstract and less phenomenological than the one we chose to describe sporozoite motility in structured environments.

In this section we propose a brief analysis of the reasoning behind the Brownian approach to self-propulsion and include a few paragraphs discussing the features of the model presented in [88], focusing in particular on the role of noise terms and stochasticity.

2.7.1 Brownian models

Consider a Brownian particle and let $\mathbf{r}$ and $\mathbf{v}$ identify, respectively, its position and velocity. The prototypical equations used to describe this system are the following:

$$\frac{d\mathbf{r}}{dt} = \mathbf{v} \ , \tag{2.13}$$

$$\frac{d\mathbf{v}}{dt} = \mathbf{f}(\mathbf{r}, \mathbf{v}, t) - \gamma(\mathbf{v})\,\mathbf{v} + \boldsymbol{\eta}(t) \ . \tag{2.14}$$

The terms $\mathbf{f}(\mathbf{r},\mathbf{v},t)$ and $\gamma(\mathbf{v})$ are a forcing and a friction term, respectively, while $\boldsymbol{\eta}(t)$ is a random force, accounting for the stochasticity in the motion of individual particles. Note that these general equations do take into account the mass of the particle.

Neglecting, for the moment being, the forcing term by setting $\mathbf{f}(\mathbf{r},\mathbf{v},t) = 0$, we can follow the formalism and rationale of [60] to introduce the concepts of active and passive noise and understand their effect on the system.

Since we refer to particles with a preferred direction of motion, it is useful to introduce a heading vector $\mathbf{e}_\mathrm{h}$. In two-dimensions, $\mathbf{e}_\mathrm{h}$ is fully determined by the angle $\phi(t)$, defining the polar orientation with respect to the x axis: $\mathbf{e}_\mathrm{h} = (\cos\phi(t), \sin\phi(t))$ (Fig. 2.13). The temporal evolution of the position becomes $\dot{\mathbf{r}}(t) = \mathbf{v}(t) = v(t)\mathbf{e}_\mathrm{h}$. Defining the orthogonal vector $\mathbf{e}_\phi(t) = (-\sin\phi(t), \cos\phi(t))$, the temporal evolution of the velocity vector reads:

$$\dot{v} = -\gamma(v)\,v + \mathbf{e}_\mathrm{h}\cdot\boldsymbol{\eta}(t) \;\;, \tag{2.15}$$

$$\dot{\phi} = \frac{1}{v}\,\mathbf{e}_\phi\cdot\boldsymbol{\eta}(t) \;\;. \tag{2.16}$$

Note that the coordinates $(v(t), \phi(t))$ differ from the traditional polar coordinates, in that the velocity $v(t)$ can also assume negative values with respect to the heading direction.

In general, active particles are influenced by two conceptually different kinds of fluctuations: *passive* fluctuations ($\boldsymbol{\eta}_\mathrm{p}(t)$), that originate from the environment in which the particle moves, and *active* fluctuations ($\boldsymbol{\eta}_\mathrm{a}(t)$), that are an independent stochastic process in the direction of motion and in the velocity with respect to the heading and perpendicular to it. Assuming Gaussian white noise terms for both the passive and active components of fluctuations, the random force $\boldsymbol{\eta}(t)$ can be written as:

$$\boldsymbol{\eta}(t) = \boldsymbol{\eta}_\mathrm{a}(t) + \boldsymbol{\eta}_\mathrm{p}(t) \;\;, \tag{2.17}$$

$$\boldsymbol{\eta}_\mathrm{a}(t) = \sqrt{2D_v}\,\xi_v(t)\,\mathbf{e}_\mathrm{h} + \sqrt{2D_\phi}\,\xi_\phi\,\mathbf{e}_\phi \;\;, \tag{2.18}$$

$$\boldsymbol{\eta}_\mathrm{p}(t) = \sqrt{2D}\,(\xi_x(t)\,\mathbf{e}_x + \xi_y(t)\,\mathbf{e}_y) \;\;. \tag{2.19}$$

Explicitly writing the active and passive fluctuations into Eqs. (2.15) and (2.16) yields:

$$\dot{v} = -\gamma(v)\,v + \sqrt{2D}\,\cos\phi\,\xi_x(t) + \sqrt{2D}\,\sin\phi\,\xi_y(t) + \sqrt{2D_v}\,\xi_v(t) \;\;, \tag{2.20}$$

$$\dot{\phi} = -\frac{\sqrt{2D}}{v}\,\sin\phi\,\xi_x(t) + \frac{\sqrt{2D}}{v}\,\cos\phi\,\xi_y(t) + \frac{\sqrt{2D_\phi}}{v}\xi_\phi(t) \;\;. \tag{2.21}$$

Equations (2.20) and (2.21) reveal that, in the (v,ϕ) frame, active fluctuations cause additive noise, while passive fluctuations translate into multiplicative noise. The Fokker-Planck equation corresponding to the probability density function (PDF) $p(v, \phi, t)$, reads:

$$\begin{aligned}\frac{\partial}{\partial t}\, p(v,\phi,t) = & -\frac{\partial}{\partial v}\left[\left(-\gamma(v)\, v + \frac{D}{v}\right) p(v,\phi,t)\right] + \\ & + (D_v + D)\frac{\partial^2}{\partial v^2}\, p(v,\phi,t) + \frac{D_\phi + D}{v^2}\frac{\partial^2}{\partial \phi^2}\, p(v,\phi,t) \ . \end{aligned} \tag{2.22}$$

The steady state solution of Eq. (2.22) factorises into the product of a ϕ-dependent and a v-dependent term. Importantly, as discussed in [60], the velocity dependent term $p(v)$, when v approaches zero, shows different behaviours depending on the contribution of active and passive fluctuations. It follows that, at least on a formal level, a study of $p(v)$ at low speeds allows to determine which kind of fluctuations is dominating in a system.

Forcing term Let us now consider a forcing term $\mathbf{f}(\mathbf{r}, \mathbf{v}, t) \neq 0$, by means of a preferred rotation described by a Lorentz-like force term, as in [89, 90]. This could be, for instance, a formal description of a circularly gliding sporozoite. The vector $\boldsymbol{\omega}$ that appears below is perpendicular to the plane of rotation, as would be, for example, the case of a magnetic field:

$$\frac{d\mathbf{r}}{dt} = \mathbf{v} \ , \tag{2.23}$$

$$\frac{d\mathbf{v}}{dt} = -\gamma(\mathbf{v})\, \mathbf{v} + \boldsymbol{\omega} \wedge \mathbf{v} + \boldsymbol{\eta}(t) \ . \tag{2.24}$$

Expressing these equations in (v, ϕ) coordinates, as done before, leads to the Fokker-Planck equation (2.22) with an additional term accounting for rotation:

$$\begin{aligned}\frac{\partial}{\partial t}\, p(v,\phi,t) = & \frac{\partial}{\partial v}\left(\gamma(v)\, v - \frac{D}{v}\right) p - \frac{\partial}{\partial \phi}\, \omega\, p + \\ & + \frac{\partial^2}{\partial v^2}\,(D_v + D)\, p + \frac{\partial^2}{\partial \phi^2}\left(\frac{D + D_\phi}{v^2}\right) p \ . \end{aligned} \tag{2.25}$$

In this case the PDF is no longer uniform in the angle, which, in contrast to the case of Eq. 2.22, prevents a simple analytical treatment in the absence of simplifying approximations.

Constant speed A common approximation in this context is to consider situations in which the speed of the particle is constant [55–57]. In this case, the probability density function of the speed is proportional to a δ-function: $p(v) = \delta(v - v_0)$. Under this assumption, the Fokker-Planck equation (in the circling case) simplifies to:

$$\frac{\partial}{\partial t}\, p(\phi, t) = -\frac{\partial}{\partial \phi}\, \omega\, p(\phi, t) + \frac{\partial^2}{\partial \phi^2}\left(\frac{D + D_\phi}{v_0^2}\right) p(\phi, t) \ . \tag{2.26}$$

This equation expresses diffusion with drift. Its solution can be found working in the Fourier space, with (ϕ_0, t_0) as initial conditions and the definition:

$$p(\phi, t|\phi_0, t_0) \sim \int dk\, \tilde{p}(k, t)\, e^{-ik\phi} \ . \tag{2.27}$$

The probability density function for the angle at time t reads:

$$p(\phi, t|\phi_0, t_0) = \frac{v_0}{\sqrt{4\pi\,(D + D_\phi)(t - t_0)}} \exp\left(-\frac{(\phi - \phi_0 - \omega\,(t - t_0))^2\, v_0^2}{4\,(D + D_\phi)(t - t_0)}\right) \ , \tag{2.28}$$

and the case $\omega = 0$ returns the solution to standard diffusion. Note that the diffusive solution refers to the angular dynamics, not to the displacement of the particle.

While in the general case (Eq. (2.25)) the shape of the probability density function gives information about the presence of active and passive fluctuations, this distinction is lost when prescribing a constant v. Indeed, the passive coefficient D and the active coefficient D_ϕ appear as a sum in Eq. (2.28), that therefore does not allow to tell the active contribution from the passive one.

Conceptually, assuming a constant v is a strong approximation if the aim is to model an active, self-propelled, particle. While overdamping the system allows to consider only its orientational degrees of freedom and certainly eases the analytical calculations, it comes at a price. The system no longer distinguishes passive from active noise or, in other words, the noise due to the environment from that due to the microscopic internal propulsion mechanism. It is therefore necessary to consider the validity of the approximation depending on the specific system under study.

2.7.2 Brownian approach to sporozoite motility

The first model for sporozoite motility in arrays of circular obstacles is a Brownian model [88] and dates back before the start of my doctoral studies. In this model, a sporozoite is approximated as a self-propelled, straight rigid rod of length 2 µm, about one fifth of the average sporozoite length. The choice of the length follows from the simplifying assumption that only the front part of the parasite is responsible for changes in the direction of motion. The propulsion is oriented in the direction of the rod's axis and accounts for the forward movement, thereby mimicking gliding. Additionally, the rod is rotated by an internal torque, which accounts for the curved shape of the sporozoite by reproducing its circular trajectories. The equations of the model read:

$$\frac{\partial \mathbf{r}}{\partial t} = \beta\, \mathbb{D}[F\, \hat{\mathbf{u}} - \mathbf{I}_r(\mathbf{r}, \phi) + \mathbf{f}] \ , \tag{2.29}$$

$$\frac{\partial \phi}{\partial t} = \beta\, D_r[M - I_\phi(\mathbf{r}, \phi) + \tau] \ . \tag{2.30}$$

The vector $\mathbf{r}$ represents the position of the rod, while the angle ϕ describes the unit vector $\hat{\mathbf{u}} = (\cos\phi, \sin\phi)$ along the rod's axis (the vector $\hat{\mathbf{u}}$ corresponds to the heading vector $\mathbf{e}_\mathrm{h}$ introduced in the previous section). The translational diffusion matrix $\mathbb{D}$ is defined as $\mathbb{D} = D_l(\hat{\mathbf{u}} \times \hat{\mathbf{u}}) + D_t(\mathbf{1} - \hat{\mathbf{u}} \times \hat{\mathbf{u}})$, where D_l is the longitudinal diffusion constant along the heading axis, and D_t is the transverse diffusion constant. The term D_r represents the rotational diffusion constant, while $\mathbf{f}$ and τ are active random terms, accounting for noise in the propulsion force and for the thermal bath.

The terms $\mathbf{I}_r(\mathbf{r}, \phi)$ and $I_\phi(\mathbf{r}, \phi)$ represent the interactions with the obstacles affecting the position and the orientation, respectively. Two kinds of interactions with obstacles are considered: a stochastic one that assumes abrupt and random changes in the direction of motion upon collision, and a deterministic one that describes the interaction with obstacles via a soft potential. In this second version, the model resembles that of a Brownian circle swimmer introduced in [55] for *E. Coli*.

The stochastic interaction scheme generates complex, too noisy trajectories that show a qualitative dependence on the geometry of the obstacle array. The deterministic interaction scheme, on the contrary, provides smooth trajectories and fails to account, for example, for meandering patterns (see [88] for further details). In general, neither of the two schemes seems to provide an effective description of sporozoite migration in obstacle arrays, which is what triggered the development of our geometry-centred model.

Considering the stochastic terms involved, the Brownian approach to sporozoite motility is relatively complex. In fact, the noise term $\mathbf{f}$ in Eq. (2.29) is a passive noise term acting on the centre of mass of the rod. On the other hand, the noise term τ in Eq. (2.30) is an active noise component, perturbing the orientation of the rod. In addition to that, the interaction with the obstacles can also include stochasticity. It follows that the Brownian model for sporozoite motility includes two to three independent noise terms, all contributing to the final dynamics of the rod.

In contrast, in this chapter we have presented a modelling approach with reduced stochasticity: in our model, randomness is localised in time and space at the interaction with the obstacles. We have traded the complexity represented by multiple noise contributions in favour of geometrical complexity, by explicitly taking into account the elongated and bent shape of the parasite. This has allowed us to explore and quantify in detail the effect of the geometrical match between the cell shape and the obstacles.

2.8 Experimental outlook

Our theoretical model for sporozoite motility in pillar arrays is tightly connected to the experimental work on sporozoite migration performed in the Frischknecht group (Heidelberg University Clinics). Past experimental observations in the group [36] have provided a valid motivation for the development of a model able to interpret the results in a formal, quantitative manner. We have tuned the model building in order for it to be predictive, which required taking into account the presence of experimental challenges, such as the unavoidable biological variance within a population of sporozoites. Thanks to these efforts, our model is now proving useful for the realisation and interpretation of experiments involving newly designed obstacle arrays with pillars of two different diameters.

As reported in Sec. 2.4.2, we predict that, in the presence of pillars with radii larger than κ_0^{-1}, a sporozoite with curvature κ_0 should spend a larger fraction of time around the pillars with the curvature closest to this value (Fig. 2.11). If both kinds of pillars have radius larger than the radius of curvature of the parasite, then circling around any of them is only possible at the cost of continuous deformations of the parasite and collisions with the pillar. In other words, we expect circling around larger pillars to be energetically more expensive that circling around matching ones. This implies that sporozoites should be able to select best matching pillars in a manner regulated by the bending energy.

Simulations, however, are performed using a model sporozoite with fixed curvature. In contrast, experiments are necessarily realised using a population of sporozoites that has an inherent heterogeneity. As shown in Fig. 2.3, a typical population of sporozoites is characterised by a broad distribution of curvatures, a feature that must be taken into account throughout the experimental process, from the design of the setup to the interpretation of the results.

To expand on this point, suppose that a population of N sporozoites has a symmetric distribution of curvatures centred in κ_0 with standard deviation σ. Let us consider an array of obstacles with radius κ_0^{-1}. Half of the sporozoites in the population need to deform to circle around a pillar, while the remaining half, in principle, is able to circle around a pillar without interacting with it nor deforming. For the $N/2$ sporozoites that can circle around the pillars without necessarily touching any of them, the obstacles are basically invisible. In an array with obstacles of curvature $\kappa_0 - 2\sigma$, a number of sporozoites much larger than $N/2$ is bound to interact with the obstacles and deform.

It follows that, when investigating pillar selection based on the bending energy, results are the more clear the smaller is the fraction of sporozoites for which the pillars are effectively invisible. We conclude that pillar arrays suitable to investigate selection are those in which both kinds of pillars have radius significantly larger than κ_0^{-1}.

The realisation of such experiments and further developments in this direction are part of the promising PhD work of Julianne Mendi Muthinja Wietzorrek (Frischknecht group).

3 Modelling collective motion of sporozoites

In this chapter we address the problem of collective motion of sporozoites. Following preparation of salivary glands of malaria infected mosquitos, sporozoites can be observed to arrange in stable, yet motile, whirl-like structures.

Section 3.1 gives an overview of our current experimental knowledge: we discuss the main features of the system and the open experimental challenges and perspectives. In Sec. 3.2 we focus on the various theoretical approaches that can be adopted in modelling collective behaviours. In Secs. 3.3 and 3.4 we define our theoretical model for a system of interacting sporozoites and present an analytical study of the model. We present and analyse the results of our numerical simulations in Secs. 3.6 and 3.7, focusing in particular on the features of the system linked to the stability of the whirl-like structures. Finally, we summarise and conclude in Sec. 3.8.

Our model is effective in interpreting the experimental observations within a formal framework and, in addition, allows to identify some of the key features of the experimental system. The model predictions contribute significantly in the definition of the next experimental efforts.

Credit for the experimental work discussed in this chapter goes to the Frischknecht group (Heidelberg University Clinics), specifically to Konrad Beyer.

3.1 Sporozoite whirls

During its complex life cycle the malaria parasite Plasmodium undergoes complicated reproductive stages in various heterogeneous environments, involving both the mosquito and the vertebrate host. Sporozoites, the stage of Plasmodium that is injected into the vertebrate host, mature in the midgut of the mosquito to then invade its salivary glands. The invasion is a process likely involving gliding motility, but its details are still a subject of active research [11]. The salivary glands of a mosquito act as a storage space for sporozoites before injection into the host (Fig. 3.1a). Sporozoites in the salivary glands are not motile and, during a mosquito bite, are injected into the skin of the host flowing with the saliva that is pumped out of the proboscis of the mosquito [91].

A schematic representation of the internal structure of a salivary gland is shown in Fig. 3.1b, which is an adaptation from [11]. A gland is delimited by the salivary gland

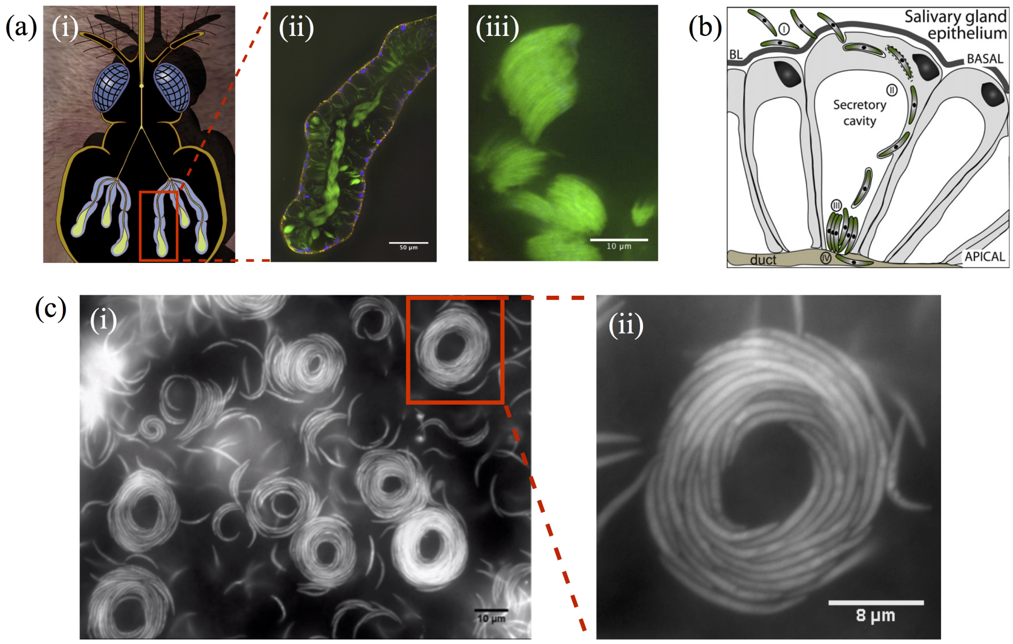

Figure 3.1: (a) (i) Sketch of a mosquito and its salivary glands, consisting of three lobes each and connected by salivary ducts [91]. (ii) Fluorescent image of an infected salivary gland. The sporozoites (green) are distributed in the extracellular space delimited by the acinar cells. (iii) Detailed view of the sporozoites in the salivary gland, arranged in non-motile stacks. (b) Drawing of a section of an infected salivary gland. Sporozoites invade the gland crossing the epithelium and basal lamina, to then settle in the cavity formed by the acinar cells. Image adapted from [11]. (c) (i) Whirls formed by GFP-expressing sporozoites at the basal lamina of a salivary gland, following preparation. (ii) Detail of a large, stable whirl with a complex dynamic structure. All experimental images have been acquired by Konrad Beyer (Frischknecht group).

epithelium. The basal lamina separates the epithelium from the acinar cells, that are shaped so that each cell forms a secretory cavity. The secretory cavities are all connected to each other, thus forming an extracellular space where the saliva is secreted. Sporozoites cross the acinar cells during invasion and stop in this extracellular space, usually arranging into non-motile stacks as shown in Fig. 3.1a(ii) and (iii).

Surprisingly, in infected salivary glands treated with an activation medium[1], sporozoites become motile and can arrange in dynamic whirl-like formations at the apical side of the basal membrane surrounding the acinar cells. Example of whirls are shown in Fig. 3.1c for the rodent model parasite Plasmodium *berghei*. Such very regular structures, most probably favoured by the natural curvature of the sporozoites, are remarkably stable and are reminiscent of collective behaviours observed in a variety of systems, biological and not, and a wide range of length-scales [63].

The experimental study of sporozoite whirls is currently performed by Konrad Beyer

---

[1] 3% BSA (bovine serum albumin) in RPMI (Roswell Park Memorial Institute medium).

(Frischknecht group). The observation and quantification of sporozoite whirls is a highly non-trivial procedure, partly due to the fact that there is currently no protocol that enables the observation of the whirls in an *in vitro*, controlled system. Whirls, in fact, can only be observed within the biologically complex salivary gland of the mosquito. For this reason, not only the experimental procedure is challenging, but so are also the interpretation and quantification of the experimental observations. The group of Dr. Heike Böhm (Heidelberg University) is currently developing image processing tools aiming at the automatisation of whirl analysis.

Tools for the detailed quantification of whirl dynamics are still under development. Nonetheless, we can exploit the experimental data currently available to gain information relevant for the definition and validation of our theoretical model, that will be extensively described throughout this chapter. At the moment, our best experimental insight into whirl structure and dynamics comes from two-dimensional images (only one focused layer) acquired using spinning disc microscopy.

Let us start with the experimental observation that the whirls form at the basal lamina surrounding a salivary gland (Fig. 3.1b). Because the gland is observed from the outside, only the layer of sporozoites adherent to the inner side of the membrane is in focus. Since only the part of the whirl that adheres to the membrane is clearly visible, the question is whether this is enough to gain information concerning the overall structure and dynamics of the whirl. We predict three main possible structures.

First, whirls could be purely two-dimensional structures: in this case we should not observe any overlap between the parasites and sporozoites would not be able to leave or join the plane of imaging. Consequently, we should be able to track each cell across the entire observation time.

Second, whirls could be two-dimensional, but sporozoites could leave a whirl or join it, thereby disappearing from or appearing into the plane of imaging. This would imply that the sporozoites are able to move within the salivary gland and, occasionally, adhere to the basal lamina and join a whirl, or leave a whirl to join the bulk.

Third, whirls could consist of several motile layers. Their third dimension could be fundamental for the overall structure and stability. In this case, the sporozoites would be able to leave or join the plane of imaging without leaving the whirl itself, but simply moving to one of the upper layers of cells. The minimal system in this framework would be a whirl consisting of a single layer, in which sporozoites can intersect. In more colloquial terms, the generic whirl would be a donut shaped, inherently three-dimensional structure, dynamic yet stable.

In order to develop a first idea about which of these three situations may be more realistic, we turn our attention to a typical whirl and look for cells intersecting each other, or cells leaving or joining the plane of imaging. As mentioned above, these events would indicate the presence of a relevant third dimension in the dynamics of the whirl.

The images in Fig. 3.2 represent GFP-expressing sporozoites and belong to a movie

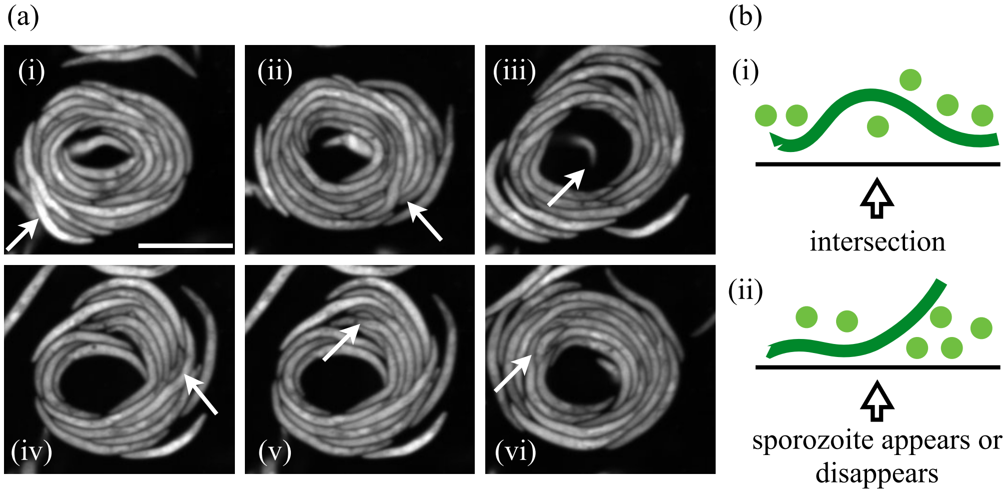

Figure 3.2: (a) Spinning disc confocal images of a sporozoite whirl at different time points (Konrad Beyer, Frischknecht group). The whirl is dynamic. Sporozoites can intersect each other as in (i) and (ii); they can join the plane of imaging and subsequently the whirl as in (iii); they may be squeezed out of the whirl as in (iv) or work their way through the whirl to the imaging plane as in (v) and (vi). Scale bar: 10 µm. (b) Schematic representation of the sporozoite configurations corresponding to intersections (i) and cells appearing into and disappearing from the plane of imaging (ii).

recorded with a spinning disc confocal microscope at 60x magnification. We indeed observe sporozoites intersecting as well as sporozoites appearing and disappearing into and from the plane of imaging. The presence of events of both kinds reveals that the adhesion to the basal lamina is not permanent and points towards the existence of a bulk of free sporozoites and/or a three-dimensional component of the whirl structure. Figures 3.2a(i) and (ii) highlight two intersection events. Figure 3.2a(iii) shows a sporozoite joining the membrane layer to subsequently (not shown) join the inner boundary of the whirl. In Fig. 3.2a(iv) the arrow points to a sporozoite that is squeezed out of the imaging plane seemingly due to several other sporozoites that push together at its side. Finally, Figs. 3.2a(v) and (vi) show the appearance of two sporozoites in the imaging plane. In both cases, the cells look like they are working their way through the layer of sporozoites, but neither the dynamics of insertion or removal of sporozoites are clear.

Figure 3.2b shows schematically how our observations support the presence of a significant role of the third dimension. The horizontal solid black lines represent the membrane onto which the whirls form, while the arrow indicates the point of view of the observer. In dark green we represent a sporozoite oriented parallel to the page, while light green circles denote sporozoites with different orientations, the details of which are not relevant. For an intersection between two sporozoites to be detected, one cell needs to detach from the membrane, overcome another cell, and then possibly work its way through a layer of sporozoites to attach to the membrane again (Fig. 3.2b(i)). Alternatively, an intersection could correspond to a sporozoite already on the membrane opening and going through a gap between another attached sporozoite and the membrane itself. Figure 3.2b(ii) sketches the process of sporozoites joining or leaving the membrane plane, which appear to be energetically less expensive processes than an intersection.

We can safely state that the analysis of the sporozoite dynamics in the plane of imaging strongly supports the presence of a relevant third dimension, be it represented by the whirl structure or by a bulk of free sporozoites in the salivary gland. However, open questions remain. It is not yet clear whether a whirl actually extends above the plane of imaging, that is to say whether there is a finite thickness to the whirl or not. If the whirl would consist indeed of a single layer on the membrane, then a cell leaving the imaging plane would become part of a reservoir of sporozoites above it. On the other hand, if the whirl had a three-dimensional structure, for example if it had a donut-like shape, sporozoites leaving the imaging plane would be cells moving within the dynamic whirl structure without leaving it.

Another open question is whether the whirls are spatially constrained. For example, we speculate that the basal lamina could be wrinkled, thus generating a compartmentalised environment. Furthermore, the whirls could be constrained in the third dimension due to limited space between the basal lamina and other structural elements of the salivary gland.

We think these questions concerning the structure of the whirls, their environment and the relation between the two could be answered by focusing on three-dimensional imaging and dedicated image analysis.

In the following, after an introduction on the modelling of collective motion, we propose our theoretical model of whirl dynamics. Due to the open experimental challenges and the lack of an in vitro system to analyse the whirls in a controlled manner, we develop a general model aiming at understanding the issues related with whirl structure and stability.

3.2 Modelling collective motion

Systems of similar, interacting self-propelled units are prone to develop collective behaviours [63]. Self-propulsion typically means that the units maintain an approximately constant absolute velocity, which is a condition that can only be realised in an open system and, therefore, tells that collective behaviours are phenomena typical of out-of-equilibrium systems. A general feature of collective motion is that the action of an individual unit is dominated by the influence of the others, that is to say, in the collective regime the individual unit behaves differently than it would do alone.

Collective motion started to be widely studied in the past years, as exhaustively discussed in the 2012 review by Vicsek and Zafeiris [63], which we refer to in this introduction. Collective phenomena are present in a wide variety of systems, length-scales and conditions. In a biological context, they can be observed, for example, in systems of actin filaments [92], tissue cells [93], bacteria [62] or, as shown here, parasites, but also fish [94] and birds [95].

Note that the interaction between the units can be of different kinds. Actin filaments interact with each other via a collision scheme that only depends on the more or less frequent contacts between the filaments [92]. A layer of cells can behave collectively based on adhesion cues between adjacent units [93]. Birds, on the other hand, are likely to behave in a flock based on a more complex interaction, including some processing of the information coming from more or less close neighbours [95].

Despite the variety of units, interaction schemes and length-scales involved, models and studies have been focusing on the common core of these systems, namely the presence of a transition from a disordered to an ordered state as a function of some relevant parameters, possibly system-specific. Efforts towards this aim include analysis in the area of statistical mechanics, in terms of critical phenomena and phase transitions, but also continuum approaches.

The seminal statistical mechanical approach is the Vicsek model [64], that considers identical point-like particles moving with a fixed speed. The particles follow an interaction rule that aligns the direction of motion with the average direction of the neighbouring particles within a definite range. In addition, the orientation of the particles is influenced by random noise.

Continuum approaches, in contrast, aim at a macroscopic description of the systems, approximating the ensemble of units to a continuous medium [96]. These approaches are more suitable to investigate the long-range properties of the systems. A third method is to use the theoretical framework offered by hydrodynamics, in which the focus is on the hydrodynamic properties of systems consisting of microscopic swimmers [97].

The analytical approach, however, is not the only available, as computer simulations are effective in modelling systems in which one wants to take into account, for instance, non-trivial geometrical features of the units or a detailed interaction scheme. An example of that is the computational modelling of *Myxococcus xanthus* [41, 62]. In these works, the bacterium is modelled as a sequence of rods and joints. Its shape is regulated by a Hamiltonian including a bending energy, that regulates the angle at the joints, and by an elastic energy, that regulates the length of the rods. The configuration of the model bacterium is determined by a sequence of node steps and stochastic relaxations. To model the interaction, the authors include several experimental observations in the model, for instance the switch between two different propulsion strategies.

Another significant example of this computational approach to collective behaviour is that of [98]. In this paper the authors schematically model bacterial flagella as flexible chains of beads, able to propel themselves forward using a wave-like motion. In the presence of an asymmetry that assigns an effective curvature to the flagella, they move on a curved trajectory and self-organise into vortices. The authors analyse both the effects of volume exclusion and hydrodynamics.

In order to model sporozoites, we adopt the computational approach coupled with an analytical argument to predict the behaviour of the system as a function of a few relevant parameters. We take into account the peculiar elongated and bent shape of the sporozoites by approximating a parasite as a chain of springs and nodes with bending energy. The behaviour of each model parasite results from the equations of motion of its nodes, and from the interaction scheme regulating the repulsion and the overlap between different objects. Because model parasites effectively act as independent agents, following a set of rules that regulate their mutual interaction, our work fits in the framework of agent-based modelling. In fact, agent-based modelling represents a broad spectrum of models, all characterised by the implementation of a set of autonomous agents, and aiming to investigate the emergence of collective behaviours. In our case, we perform deterministic simulations and do not impose any alignment rule between the agents, but instead the alignment results only from excluded volume interactions mediated by a potential. While this approach can be more expensive than implementing a coarse-grained interaction scheme, it allows to study the system across a wider range of length-scales, from the interaction between two agents to the overall behaviour of the organised system. Because in principle systematic experimental observations of the interactions between the sporozoites are possible, we decided to maintain the possibility of a direct comparison between the experimental and the model system.

3.3 Model

3.3.1 Agent definition

A sporozoite (agent) is modelled as a chain of springs and nodes (Fig. 3.3a). Pairs of consecutive nodes are connected by identical harmonic springs. Each node is assigned a bending energy that ensures that the rest configuration of the chain lies on a circular arc. In addition, each node is the centre of a two-dimensional Gaussian potential, that regulates the interaction between the agents, allowing them both to deform and to overlap upon collision (Fig. 3.3b). Based on our experimental observations and the literature, in the following we prescribe each unperturbed agent to move counterclockwise on a trajectory with curvature matching its own [22].

All the agents are identical and have total length L and rest curvature κ_0. They are discretised in N_n nodes spaced by $R_0 = L/(N_\mathrm{n} - 1)$, while the angle formed by three consecutive nodes is given by $\theta_0 = \pi - R_0\kappa_0$.

We fix $N_\mathrm{n} = 15$ and consider nodes with non-zero, identical masses M. Taking into account the mass eases the control of the agent's length and allows to explore a more comprehensive range of physical situations.

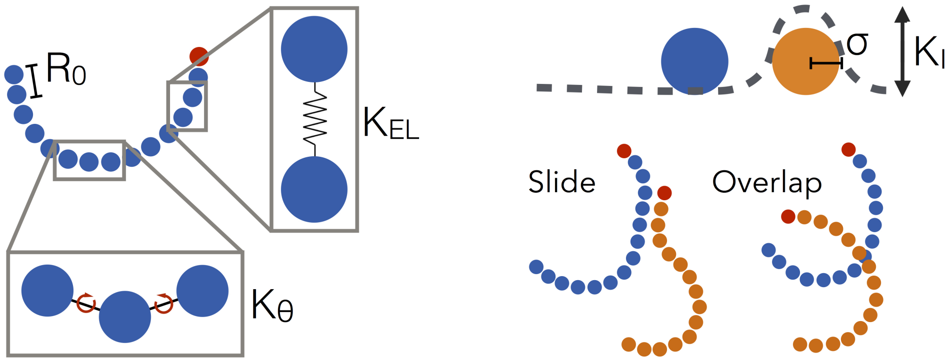

(a) (b)

Figure 3.3: (a) A sporozoite is modelled as a chain of nodes connected by springs with elastic constant K_{EL} and rest length R_0. The model sporozoite has a non-zero rest curvature and has bending stiffness K_θ. (b) Each node corresponds to a two-dimensional Gaussian potential of height K_{I}. Two interacting model sporozoites can either deform sliding along each other, or overlap. The decision between the two possibilities is deterministic and follows from the integration of the equation of motion of each node.

3.3.2 Equation of motion

Each node of each agent obeys an equation of motion that, denoting the position of the i^{th} node in the (x, y) plane as $\mathbf{r}_i$, reads:

$$M\ddot{\mathbf{r}}_i = \mathbf{F}_{\mathrm{P}} - \Gamma\dot{\mathbf{r}}_i + \mathbf{F}_{\mathrm{I}} + \mathbf{F}_{\mathrm{EL}} + \mathbf{F}_\theta \quad , \tag{3.1}$$

which includes a propulsion force $\mathbf{F}_{\mathrm{P}}$, a friction term proportional to the coefficient Γ, an interaction force $\mathbf{F}_{\mathrm{I}}$ due to the presence of the other agents, and two internal forces $\mathbf{F}_{\mathrm{EL}}$ and $\mathbf{F}_\theta$ that constrain the length and the shape of the agent.

Propulsion force $\mathbf{F}_{\mathrm{P}}$ The direction of the propulsion force for each node is determined by the position of the adjacent nodes. In general, the i^{th} node is propelled in the direction identified by the $(i-1)^{\mathrm{th}}$ and $(i+1)^{\mathrm{th}}$ nodes. For the head node the direction is that connecting the 1st with the 2nd node, while for the tail node the direction is that connecting the last with the second to last node. We consider the magnitude of the propulsion force identical for all the nodes and constant in time.

Interaction force $\mathbf{F}_{\mathrm{I}}$ We define a purely repulsive interaction between the agents by associating a Gaussian potential to each node. Two nodes $\mathbf{r}_i$ and $\mathbf{r}_j$, belonging to different agents, exert on each other a force of magnitude:

$$f_{ij} = K_{\mathrm{I}} \frac{d_{ij}}{\sigma^3\sqrt{2\pi}} \exp\left(-\frac{d_{ij}^2}{2\sigma^2}\right) \quad , \tag{3.2}$$

where d_{ij} is the distance between the two nodes and σ is the standard deviation of the Gaussian associated to each node. The direction of the force f_{ij} is that of the line connecting nodes $\mathbf{r}_i$ and $\mathbf{r}_j$. We refer to the constant K_I as the interaction parameter.

Elastic force $\mathbf{F}_\mathrm{EL}$ The term $\mathbf{F}_\mathrm{EL}$ prescribes the distance between two consecutive nodes in an agent. Consider $\mathbf{r}_i$ and $\mathbf{r}_{i+1}$, belonging to the same agent. The elastic energy associated to their distance is:

$$E_\mathrm{EL}^{i,i+1} = K_\mathrm{EL}(d_{i,i+1} - R_0)^2 \ , \tag{3.3}$$

where K_EL is a constant and $d_{i,i+1}$ is the distance between $\mathbf{r}_i$ and $\mathbf{r}_{i+1}$. Based on the elastic energy we compute the force $\mathbf{F}_\mathrm{EL}$, that for an internal node is the result of two contributions $\mathbf{F}_\mathrm{EL}^{i,i+1}$ and $\mathbf{F}_\mathrm{EL}^{i,i-1}$. The force $\mathbf{F}_\mathrm{EL}^{i,i\pm1}$ is exerted along the direction connecting the i^th and $(i \pm 1)^\mathrm{th}$ nodes.

Bending force $\mathbf{F}_\theta$ This term prescribes the curvature of the chain. We assign to each node, except the head and the tail nodes, a bending energy given by:

$$E_\theta^i = K_\theta(\theta_{i-1,i+1} - \theta_0)^2 \ . \tag{3.4}$$

The force $\mathbf{F}_\theta$ acting on the i^th node is computed considering the torques exerted on the segments connecting node i with the nodes $i \pm 1$.

3.3.3 Non-dimensional parameter set

We identify a set of non-dimensional parameters in order to study the model in a general framework. The relevant model parameters and their corresponding physical dimensions are: M, mass of a node [M]; K_EL, elastic constant of the spring connecting two consecutive nodes [MT^{-2}]; F_P, propulsion force [MLT^{-2}]; Γ, translational friction coefficient [MT^{-1}]; K_I, interaction coefficient [ML^{3}T^{-2}]; K_θ, bending stiffness [ML^{2}T^{-2}]; L, length of an agent [L]; σ, width of the Gaussian [L]. We choose the following non-dimensional parameter set:

$$\widetilde{F}_\mathrm{P} = \frac{F_\mathrm{P}}{K_\mathrm{EL}\sigma}, \ \widetilde{\Gamma} = \frac{\Gamma}{\sqrt{M\,K_\mathrm{EL}}}, \ \widetilde{K}_\mathrm{I} = \frac{K_\mathrm{I}}{K_\mathrm{EL}\sigma^3}, \ \widetilde{K}_\theta = \frac{K_\theta}{K_\mathrm{EL}\sigma^2}, \ \widetilde{L} = \frac{L}{\sigma} \ . \tag{3.5}$$

3.4 Analytical study

3.4.1 Timescales

In order to quantitatively characterise the model, we identify several timescales that are relevant in determining the behaviour of the system. In particular, we distinguish between two structural timescales, originating from the mechanical properties of the agents, and two interaction timescales, determined by the interplay between different agents.

Structural timescales Let us consider the angle θ formed by three consecutive nodes. The generic equation for the behaviour of θ reads:

$$I\ddot{\theta} = -K_\theta \, \theta - \Gamma^* \dot{\theta} \ . \tag{3.6}$$

Solving the equation in the overdamped limit produces a typical timescale $\tau_{\text{damp}} = \Gamma^*/K_\theta$, characterising the friction dominated relaxation of an agent after a change in bending. On the contrary, neglecting the friction term yields the oscillation period $\tau_{\text{osc}} = \sqrt{I/K_\theta}$.

The units of Γ^* are $[\Gamma^*] = \mathrm{L}^2[\Gamma]$; identifying the length-scale with R_0 yields the relation $\Gamma^* = R_0^2\Gamma$. Coherently, we can approximate the moment of inertia I with $I = MR_0^2$. This leads to:

$$\tau_{\text{damp}} = \frac{R_0^2\Gamma}{K_\theta}, \ \ \tau_{\text{osc}} = R_0\sqrt{\frac{M}{K_\theta}} \ . \tag{3.7}$$

Interaction timescales In studying the typical timescales related to the interaction between the agents, we focus on determining the time required for two agents to overlap upon collision (τ_{over}) and on the time required to deviate an agent upon collision (τ_{dev}). Let us consider the equation:

$$0 = F_{\mathrm{P}} - \Gamma\dot{x} - \frac{K_{\mathrm{I}}}{\sigma^3\sqrt{2\pi}}|x|e^{-\frac{x^2}{2\sigma^2}} \ , \tag{3.8}$$

that is the one-dimensional equation for a single node interacting with an energy bump in the overdamped limit. Considering the energy bump centred in $x = 0$ we can limit the treatment to $x < 0$ and therefore write:

$$0 = F_{\mathrm{P}} - \Gamma\dot{x} + \frac{K_{\mathrm{I}}}{\sigma^3\sqrt{2\pi}}xe^{-\frac{x^2}{2\sigma^2}} \tag{3.9}$$

$$\Rightarrow \ \dot{x} = \frac{F_{\mathrm{P}}}{\Gamma} + \frac{1}{\Gamma}\frac{K_{\mathrm{I}}}{\sigma^3\sqrt{2\pi}}xe^{-\frac{x^2}{2\sigma^2}} \tag{3.10}$$

$$\Rightarrow \ t - t_0 = \Gamma\int_{x(t_0)}^{x(t)} dt' \frac{1}{F_{\mathrm{P}} + \frac{K_{\mathrm{I}}}{\sigma^3\sqrt{2\pi}}xe^{-\frac{x^2}{2\sigma^2}}} \ . \tag{3.11}$$

Equation (3.11) cannot be integrated. To reach an estimate for the timescale we have to approximate the integral. For this reason we restrict the integration between -2σ and $-\sigma$ and, in this interval, substitute the force $xe^{-\frac{x^2}{2\sigma^2}}K_{\mathrm{I}}/(\sigma^3\sqrt{2\pi})$ with a linear function:

$$\frac{K_{\mathrm{I}}}{\sigma^3\sqrt{2\pi}}xe^{-\frac{x^2}{2\sigma^2}} \ \ \rightarrow \ \ -\frac{K_{\mathrm{I}}}{\sigma^2}\frac{1}{\sqrt{2\pi e}}\left(2 + \frac{x}{\sigma}\right) \ . \tag{3.12}$$

Consequently, the approximated interaction force in the chosen range $[-2\sigma, -\sigma]$ is 0 in -2σ, while in $-\sigma$ it equals $F_{\min} = -K_{\mathrm{I}}/(\sigma^2\sqrt{2\pi e})$, which is also the minimum of the original interaction force. Now the integral can be solved exactly:

$$t - t_0 \simeq \Gamma \int_{x(t_0)}^{x(t)} dt' \frac{1}{F_\mathrm{P} + F_\mathrm{min}\left(2 + \frac{x}{\sigma}\right)} \tag{3.13}$$

$$\Rightarrow\ t - t_0 \simeq \Gamma \frac{\sigma}{F_\mathrm{min}} \log \left[F_\mathrm{P} + F_\mathrm{min}\left(2 + \frac{x}{\sigma}\right)\right]_{x(t_0)}^{x(t)} \tag{3.14}$$

$$\Rightarrow\ \tau^*_\mathrm{over} \simeq \Gamma \frac{\sigma}{F_\mathrm{min}} \log\left(1 + \frac{F_\mathrm{min}}{F_\mathrm{P}}\right) \text{ with } x(t) = -\sigma,\ x(t_0) = -2\sigma\ . \tag{3.15}$$

Consistently, prescribing a constant ratio F_P/Γ (constant velocity in steady state), $\tau^*_\mathrm{over} \to \infty$ for $\Gamma \to -F_\mathrm{min}$, while $\tau^*_\mathrm{over} \to 0$ for $\Gamma \to \infty$.

From Eq. (3.14) we can compute the timescale associated to a deviation as the time required to reach zero speed as an effect of the encounter with an energy bump. We use Eq. (3.14) to express $x(t)$, then derive with respect to time taking into account that $x(t_0) = -2\sigma$:

$$F_\mathrm{P} + F_\mathrm{min}\left(2 + \frac{x(t)}{\sigma}\right) = \left[F_\mathrm{P} + F_\mathrm{min}\left(2 + \frac{x(t_0)}{\sigma}\right)\right] \exp\left(\frac{F_\mathrm{min}}{\Gamma\sigma}(t - t_0)\right) \tag{3.16}$$

$$\Rightarrow\ v(t) = \frac{F_\mathrm{P}}{\Gamma} \exp\left(\frac{F_\mathrm{min}}{\Gamma\sigma}(t - t_0)\right) \tag{3.17}$$

$$\Rightarrow\ \tau^*_\mathrm{dev} = -\frac{\Gamma\sigma}{F_\mathrm{min}} = \frac{\Gamma\sigma^3}{K_\mathrm{I}}\sqrt{2\pi e}\ . \tag{3.18}$$

Taking into account that each agent consists of N_n identical nodes, each propelled by a force $\mathbf{F}_\mathrm{P}$ and subject to a friction Γ, we can adjust the treatment above substituting $N_\mathrm{n}F_\mathrm{P}$ to F_P and $N_\mathrm{n}\Gamma$ to Γ. This leads to the adjusted timescales:

$$\tau_\mathrm{over} = \Gamma\sigma \frac{N_\mathrm{n}}{F_\mathrm{min}} \log\left(1 + \frac{F_\mathrm{min}}{N_\mathrm{n}F_\mathrm{P}}\right)\ , \tag{3.19}$$

$$\tau_\mathrm{dev} = -\Gamma\sigma \frac{N_\mathrm{n}}{F_\mathrm{min}}\ . \tag{3.20}$$

3.4.2 Interpretation

We compare the two structural timescales τ_damp and τ_osc to quantify the role of friction in the dynamics of the system. In particular, the system is friction dominated when $\tau_\mathrm{damp} > \tau_\mathrm{osc}$, i.e. when the damping suppresses the oscillations. This leads to the condition:

$$\Gamma > \frac{\sqrt{MK_\theta}}{R_0}\ . \tag{3.21}$$

From the interaction timescales we can derive two independent conditions. Firstly, for τ_over to exist, the argument of the logarithm in Eq. (3.19) must be positive:

$$\exists\ \tau_\mathrm{over}\ \Leftrightarrow\ \frac{F_\mathrm{min}}{F_\mathrm{P}N_\mathrm{n}} > -1\ \Rightarrow\ K_\mathrm{I} < N_\mathrm{n}F_\mathrm{P}\sigma^2\sqrt{2\pi e}\ . \tag{3.22}$$

Note that, if the condition is not verified, then, within our approximation, overlap is impossible and the system reduces to a purely two-dimensional one.

Secondly, the condition $\tau_{\text{dev}} > \tau_{\text{over}}$ leads to the relation:

$$\tau_{\text{dev}} > \tau_{\text{over}} \quad \Leftrightarrow \quad K_{\text{I}} < N_{\text{n}} \left(1 - \frac{1}{e}\right) \sigma^2 \sqrt{2\pi e} F_{\text{P}} \ . \tag{3.23}$$

When this condition is satisfied, the time two colliding agents need to deviate from their original trajectory is longer than the time required for the two agents to cross each other. Consequently, collisions between agents result in low or limited deviations.

Using the non-dimensional parameter set of Eq. (3.5), Eqs. (3.21), (3.22) and (3.23) can be rewritten as:

$$\widetilde{\Gamma} > \frac{\sqrt{\widetilde{K}_\theta}}{\widetilde{R}_0} \ , \tag{3.24}$$

$$\widetilde{K}_{\text{I}} < N_{\text{n}} \widetilde{F}_{\text{P}} \sqrt{2\pi e} \ , \tag{3.25}$$

$$\widetilde{K}_{\text{I}} < N_{\text{n}} \widetilde{F}_{\text{P}} \sqrt{2\pi e} \left(1 - \frac{1}{e}\right) \ . \tag{3.26}$$

Correspondingly, the timescales can be rewritten in units of $\sqrt{M/K_{\text{EL}}}$ as:

$$\widetilde{\tau}_{\text{damp}} = \frac{\widetilde{\Gamma} \widetilde{R}_0^2}{\widetilde{K}_\theta} \ , \tag{3.27}$$

$$\widetilde{\tau}_{\text{osc}} = \frac{\widetilde{R}_0}{\sqrt{\widetilde{K}_\theta}} \ , \tag{3.28}$$

$$\widetilde{\tau}_{\text{dev}} = \frac{\widetilde{\Gamma} N_{\text{n}}}{\widetilde{K}_{\text{I}}} \sqrt{2\pi e} \ , \tag{3.29}$$

$$\widetilde{\tau}_{\text{over}} = -\frac{\widetilde{\Gamma} N_{\text{n}}}{\widetilde{K}_{\text{I}}} \sqrt{2\pi e} \log \left(1 - \frac{\widetilde{K}_{\text{I}}}{N_{\text{n}} \widetilde{F}_{\text{P}}} \frac{1}{\sqrt{2\pi e}}\right) \ . \tag{3.30}$$

3.4.3 Phase diagram

Equations (3.24), (3.25) and (3.26) identify three regions in the three-dimensional space with axes $(\widetilde{F}_{\text{P}}, \widetilde{K}_{\text{I}}, \widetilde{\Gamma})$, thus defining a phase diagram as represented in Fig. 3.4a for a selected set of values of the structural parameters $(\widetilde{R}_0, \widetilde{K}_\theta, N_{\text{n}})$.

In Fig. 3.4a, the green plane corresponds to $\widetilde{\Gamma} = \sqrt{\widetilde{K}_\theta}/\widetilde{R}_0$. Above this plane friction is relevant, the response of an agent to a deformation is slow and, as a consequence, deformations are persistent.

The blue plane corresponds to $\widetilde{K}_{\text{I}} = N_{\text{n}} \sqrt{2\pi e} \widetilde{F}_{\text{P}}$. For parameter sets between this plane and the plane $\widetilde{F}_{\text{P}} = 0$ the agents cannot cross each other, so in this region the dynamics of the system is determined by excluded volume effects.

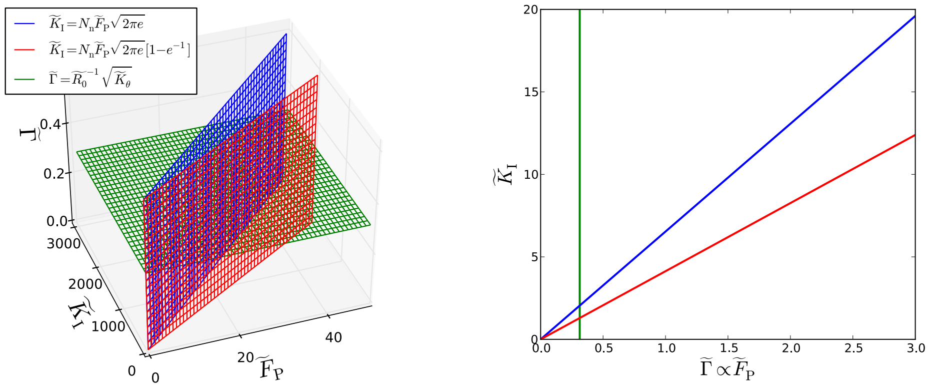

(a) (b)

Figure 3.4: (a) Three-dimensional phase diagram in the space $(\widetilde{F}_\mathrm{P}, \widetilde{K}_\mathrm{I}, \widetilde{\Gamma})$, corresponding to propulsion force, interaction parameter and friction term. The region above the green plane denotes the friction dominated region. The region between the blue plane and $\widetilde{F}_\mathrm{P} = 0$ corresponds to the area where overlap between the agents is impeded. The region between the red and the blue planes delimits the region in which overlap between the agents is still possible but deviations have a strong influence on the solution of the collisions. (b) Two-dimensional diagram, obtained under the constraint of constant ratio $\widetilde{F}_\mathrm{P}/\widetilde{\Gamma} = 0.11$. The plane is divided according to the relevance of friction, overlap and deformations, in a manner and colour-coding analogous to the three-dimensional case. The parameters used in these plots are: $N_\mathrm{n} = 15$, $\widetilde{K}_0 = 2.22$ and $\widetilde{R}_0 = 4.76$.

The red plane corresponds to $\widetilde{K}_\mathrm{I} = N_\mathrm{n}\sqrt{2\pi e}\widetilde{F}_\mathrm{P}\,(1 - 1/e)$ and identifies an overlap dominated region between the red plane and the plane $\widetilde{K}_\mathrm{I} = 0$. This area corresponds to a system in which the agents are quick to cross over each other, which implies that collisions cause only little deformations. On the contrary, the region between the red and the blue plane is characterised by high overlap times if compared to the deviation times. It follows that there deformations of the agents upon collision are pronounced. Note, in addition, that the time required for an agent to recover its shape after a deformation is friction dependent.

Constraint In the following we work under the constraint of a constant ratio $F_\mathrm{P}/\Gamma = c$. In this case, the phase diagram reduces to a planar cut through the phase diagram as shown in Fig. 3.4b, because $\widetilde{\Gamma} \propto \widetilde{F}_\mathrm{P}$:

$$\widetilde{\Gamma} = \widetilde{F}_\mathrm{P}\,\frac{\sigma}{c}\sqrt{\frac{K_\mathrm{EL}}{M}}\ . \qquad (3.31)$$

3.5 Simulations

3.5.1 FLAME

Simulations are performed using FLAME (`www.flame.ac.uk`), an enabling tool to create agent-based models. Defining agent-based models within the FLAME framework, a simulation program is automatically generated able to run efficiently on high performance computers. Despite the final code being created automatically, the user has complete control over the definition and implementation of the models. In fact, the user is in charge of the definition of the agents, their properties and actions via a combination of XML declaration files and a sequence of functions written in C.

In our case, we only have a single C function in which we integrate the equation of motion for each node using a 4^{th} order Runge-Kutta method. On the other hand, FLAME is in charge of managing the communication between the agents, that is the computationally most expensive piece of code in agent-based modelling, because in general the action of an agent depends on the configuration of all the others. FLAME implements the communication via a so called message board, where the information about each agent is routinely posted. At each iteration, each agent reads from the board the relevant information about the other agents and reacts accordingly, based on the user-defined C functions. At the end of this reaction, the agent writes its up to date information onto the board. Since each agent acts at iteration i based on the configuration of the system at $i-1$, the order with which the agents are updated is irrelevant.

3.5.2 Neighbours

To limit the amount of information that has to be processed at each iteration, we assume that an agent can only be influenced by the agents that are within its neighbourhood (blue agents in Fig. 3.5). The neighbourhood is defined as the agent's bounding box plus a frame of thickness Δ, that should be larger than or equal to the width of a node.

The assumption of such a neighbourhood is physically motivated by the fact that the interaction between the agents is short-range and due to volume exclusion. Specifically, the interaction range is of order σ, the width of the Gaussian potential assigned to each node.

3.5.3 Overlap

By assigning a Gaussian potential to each node, we effectively introduce a short-range, repulsive interaction between two agents. However, since a Gaussian bump is no hard-core potential, agents are allowed to cross each other (Fig. 3.3b). In order to avoid numerical problems due to the discrete structure of the agents and in order to keep the number of agents falling in the neighbour box manageable also at large densities, we assume that two intersecting agents are invisible to each other. As an example, consider in Fig. 3.5 the

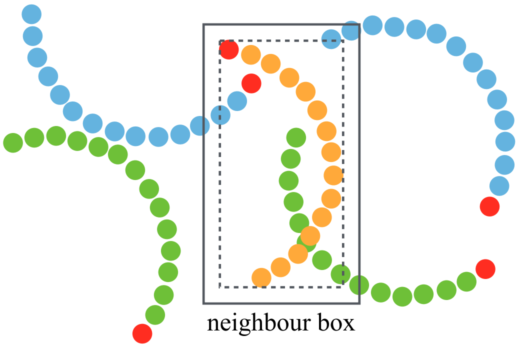

Figure 3.5: Scheme of the procedure used to identify the neighbours of each agent. Neighbours of the orange agent are considered all the agents that have at least one node inside the box delimited by the solid black line. The box consists of the bounding box of the orange agent plus a frame of thickness larger or equal than the width of a node.

green sporozoite within the neighbour box: it and the orange agent are invisible to each other as long as they are intersecting.

Apart from being computationally convenient, this implementation of the relation with the neighbours is also consistent with experimental observations, where intersecting sporozoites glide seemingly without affecting each other, probably due to a relevant role of the third dimension in the whirl dynamics (3.2a).

3.5.4 Set up

Simulations are performed using a set of identical agents and various pairs of interaction and friction parameters to span the $(\widetilde{\Gamma}, \widetilde{K}_{\mathrm{I}})$ plane. The agents move in a square box with periodic boundary conditions. Simulations start with the agents arranged such that their centres of mass lie on a square lattice, but the orientation of each agent is chosen randomly from a uniform distribution in $[0, 2\pi]$. We maintain constant the ratio $\widetilde{F}_{\mathrm{P}}/\widetilde{\Gamma}$, so that the steady state velocity of the agents is constant and, as explained in Sec. 3.4.3, the system can be interpreted based on a two-dimensional phase diagram. While varying $\widetilde{K}_{\mathrm{I}}$, $\widetilde{\Gamma}$ and $\widetilde{F}_{\mathrm{P}}$ we keep the quantities $\widetilde{K}_{\theta}$ and $\widetilde{R}_0$ constant so that, as a consequence, $\widetilde{\tau}_{\mathrm{osc}}$ does not vary.

3.6 Results

We span the $(\widetilde{\Gamma}, \widetilde{K}_{\mathrm{I}})$ plane by considering $N_{\mathrm{a}} = 400$ agents moving in a box of side $6\widetilde{L}$ with periodic boundary conditions. The choice of the number $N_{\mathrm{a}} = 400$ is a compromise between the computational cost and the observed self-organisation of the system. The role of the density of the agents is discussed in Sec. 3.7.3. The values of the fixed parameters are $\widetilde{R}_0 = 4.76$ and $\widetilde{K}_{\theta} = 2.22$, while the ratio $\widetilde{F}_{\mathrm{P}}/\widetilde{\Gamma} = 0.11$ and $\widetilde{L} = 66.67$. The value of $\widetilde{L}$

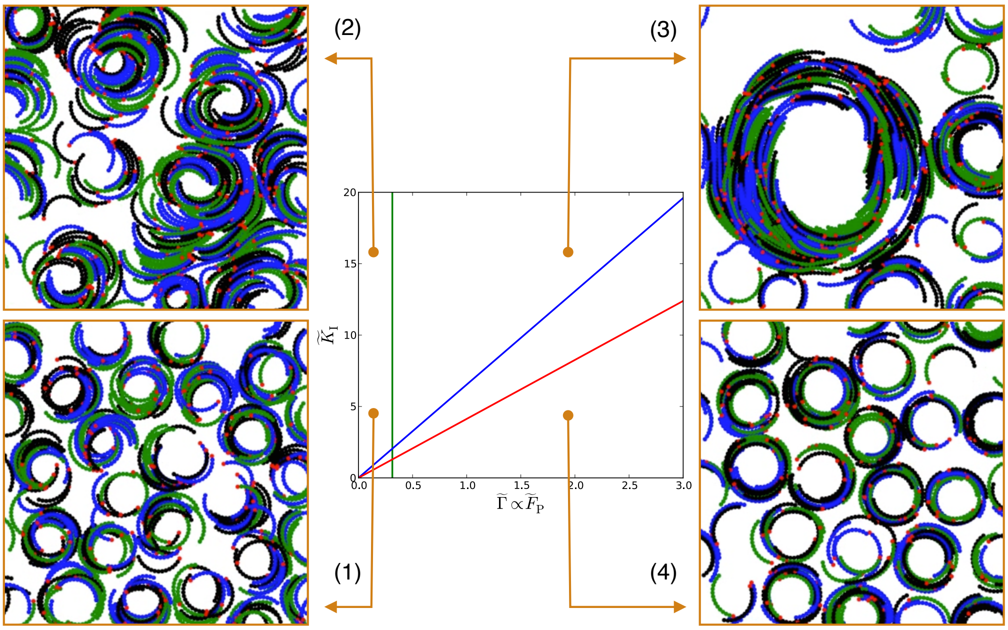

Figure 3.6: Different organisation regimes of the system for various pairs $(\widetilde{\Gamma}, \widetilde{K}_{\mathrm{I}})$. Regimes (1) and (2) are characterised by low friction, implying a fast recovery from deformations. At low values of $\widetilde{K}_{\mathrm{I}}$, overlap is favoured and not-so-compact whirl-like patterns appear. At high $\widetilde{K}_{\mathrm{I}}$, volume exclusion leads to more disordered structures. High friction regimes (3) and (4) are characterised by persistent deformations. Because of the high $\widetilde{K}_{\mathrm{I}}$, in (3) overlap is deterred and whirls are dense, large and unstable. Finally, in (4), overlap is favoured, so whirls form and stay stable thanks to limited deformations and weak interactions between the agents.

is such that the ratio $6\sigma/L \simeq 0.1$, thereby reflecting the experimentally measured aspect ratio of sporozoites [21].

3.6.1 Regimes

Figure 3.6 shows a representative sample of the typical simulation outcomes for different pairs of friction and interaction parameters. Independently of the values of $\widetilde{\Gamma}$ and $\widetilde{F}_{\mathrm{P}}$, provided they are both positive, the system evolves to form whirl-like structures, whose dimensions, shape and stability are parameter dependent. Importantly, the formation of the whirls stems from the curvature of the agents, as explained in more detail in Sec. 3.7.2, where we study a population of agents with mixed curvatures.

We can qualitatively distinguish four main regimes. Regimes (1) and (2) (Fig. 3.6) are characterised by low friction, which leads to a low $\widetilde{\tau}_{\mathrm{damp}}$ (Eq. 3.27), that causes a fast recovery from deformations. In (1), a low $\widetilde{K}_{\mathrm{I}}$ leads to a short overlap time $\widetilde{\tau}_{\mathrm{over}}$ and a diverging deviation time $\widetilde{\tau}_{\mathrm{dev}}$, so that two colliding agents are more likely to overlap rather than to deform and deviate. Under these conditions, the system arranges into stable whirl-like structures consisting of weakly interacting agents. By labelling a whirl as stable, we mean that its shape and size remain almost constant throughout the simulation time. Because of the low friction, inertia is not negligible and collisions between the agents are semi-elastic, thereby preventing the whirls from acquiring compactness.

Increasing $\widetilde{K}_\mathrm{I}$ leads to (2). Overlap is rare, because $\widetilde{\tau}_\mathrm{over}$ is large compared to $\widetilde{\tau}_\mathrm{dev}$. The dynamics of the system in regime (2) is highly influenced by excluded volume interactions. Collisions are frequent and mostly resolved by deviations and deformations rather than overlap. However, because of the low friction the system has a relevant elastic component: colliding agents bounce against each other and the recovery from deformations is quick. The whirls that form under these conditions are thicker because of excluded volume but, as in (1), low friction prevents the whirls from acquiring compactness and stability.

With high interaction parameters, that deter overlap, and high frictions, we find regime (3). This is characterised by a preference for deformations over overlap, with the presence of high friction that makes the deformations of the agents more persistent. This regime is characterised by the formation of whirls that are compact but systematically unstable. In fact, referring to Fig. 3.7, a typical newly born whirl has a size compatible with the rest trajectory of an agent. However, the whirl evolves by progressively increasing its size till it opens up and transforms in what we will call a swarm. As a next step, the curvature of the agents bends the swarm and leads to the formation of a new whirl. We trace the reason of the whirl evolution in that $\widetilde{\tau}_\mathrm{damp}$ is high, so deformations are persistent, and $\widetilde{\tau}_\mathrm{over}$ is high, so that deformations are favoured over overlap. Indeed, the agents in a whirl are deformed due to the mutual interaction that deters overlap. At the same time, relaxation from a deformation is slowed down by friction. The net consequence of excluded volume interaction is the straightening of the agents, so the whirls become bigger and finally open up. In other words, a whirl in these conditions is subject to an effective pressure, tending to disrupt it. This effect is not balanced by the tendency of the agents to restore their shape, which would generate a counterbalancing pressure with the effect of keeping the size of the whirl stable.

High frictions and low interaction parameters lead to configurations in which overlap is likely and collisions are inelastic. Deformations are persistent because of the high friction, but the fact that overlap is favoured over deviations decreases the relevance of the longer relaxation time. The system evolves to form whirls that are stable and of size compatible with the rest trajectory of an agent. The stability of these whirls lies in the possibility to overlap, so that in this case we obtain stable multi-layered whirls.

At agent speed of $1\,\mu\mathrm{m\,s}^{-1}$ the simulation time amounts to 16 min. The typical configurations emerge before half of the simulation time. Though dynamic, the appearance of the system is qualitatively stable.

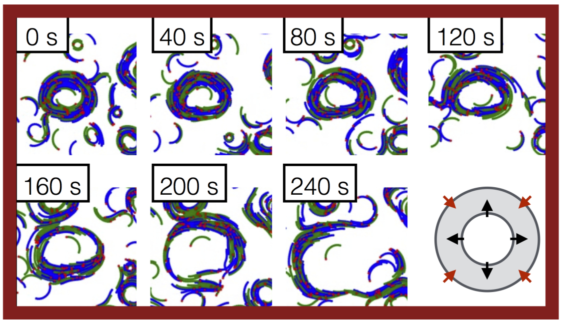

Figure 3.7: A newly formed whirl typically encloses an area comparable with that of the unperturbed trajectory of a single agent. High values of $\widetilde{K}_{\mathrm{I}}$ favour deviations over overlap, resulting in deformations of the agents. High frictions $\widetilde{\Gamma}$ render the deformations persistent, thereby forcing the whirl to grow via progressive straightening of the agents, till it finally breaks and opens up. The times in this figure are computed under the assumption of a typical agent's speed of $1\,\mu\mathrm{m}\,\mathrm{s}^{-1}$.

3.6.2 Analysis of the whirls

In order to quantify the dynamics of the whirl-like structures that emerge during the simulation time, we developed a routine in Python, able to automatically detect the whirls and follow their evolution throughout the simulation time. The simulation output required for the analysis described in this section are the coordinates of the nodes of the agents and their corresponding velocities at each recorded time step. The analysis routine couples a morphological analysis of the position of the nodes with an analysis of their velocity field. Let us first describe the steps necessary to study the output of a single time step.

1. Consider the simulation box and divide it into bins the side of that is comparable with the width of a node 2σ. In order to manage the structures that form close to the periodic boundary, paste together four identical boxes and allow an extra border slightly larger than the agent's length L.

2. Consider the coordinates of the nodes and build a binary image by placing each node into the corresponding histogram bin.

3. Consider the velocities of the nodes and build the matrices storing the mean velocity per bin in the x and y directions.

4. Use morphological tools to isolate the holes in the binary image built from the coordinates. Considering as potential whirls only close aggregates of agents, the presence of a whirl implies the presence of a hole, but a hole does not necessarily correspond to a whirl.

5. Fit an ellipse to each of the isolated holes. If a hole is the centre of a whirl, then the ideal velocity field on the ellipse is given by its tangent vectors, oriented counterclock-

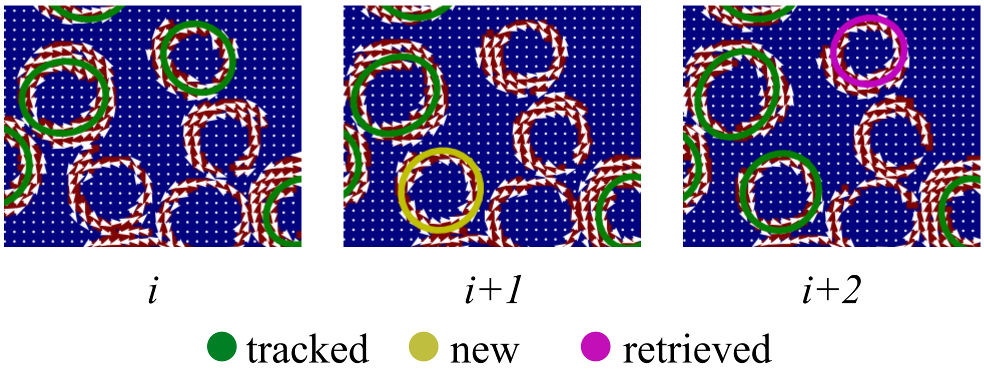

Figure 3.8: Classification of the whirls. Our algorithm detects the whirls at each recorded time point by coupling a morphological argument with the velocity field of the system. Each whirl is fitted with an ellipse, whose parameters are used for later whirl quantification. The algorithm is able to detect the newly formed whirls, follow the same whirl across the simulation time, and retrieve it if it is lost for a limited number of frames.

wise. Bin this ideal velocity field in the discretised velocity field of the sporozoites that was identified above.

6. Compute the scalar product between the binned, ideal velocity field of the ellipse and the mean velocity of the sporozoites in the same bins. If the result is above a user defined threshold, the ellipse is accepted as one belonging to a whirl (coloured ellipses in Fig. 3.8).

After the whirls are successfully identified, we can perform quantitative measurements using the fitted ellipses, such as area, orientation and eccentricity. The algorithm outlined above is only able to characterise the system at a single time step. In order to study the time evolution of the whirls, we labeled each whirl and managed the labels across the different frames. The matching of an ellipse in one frame with the corresponding ellipse in a neighbouring frame is implemented via a comparison of the ellipse's parameters.

Figure 3.8 shows a sample output of the time tracking. A whirl with a green fitted ellipse has a match with a whirl in the previous frame, a yellow ellipse denotes the appearance of a new whirl, while a purple ellipse identifies a whirl that is not present in the last frame but has a match in the second-to-last frame.

3.6.3 Detailed quantification

Using the routine described above, we quantify the time evolution of the whirls. In particular, we monitor:

- n_w, the number of whirls at each time step;
- $\langle A_\mathrm{w} A_0^{-1} \rangle$, the mean area enclosed by each whirl at each time step. We represent the

mean whirl area with reference to $A_0 = \pi\kappa_0^{-2}$, the area of the unperturbed trajectory of an agent with curvature κ_0;

- τ_{age}, the mean age of the whirls at each time step.

Time is measured in seconds under the experimentally consistent assumption that the mean speed of the agents is $1\,\mathrm{\mu m\,s^{-1}}$ and agents are $10\,\mathrm{\mu m}$ long [27]. With this length, the curvature of the agents reads $\kappa_0 = 0.24\,\mathrm{\mu m^{-1}}$, which is consistent with the average curvature measured in a population of sporozoites [27]. This set up allows to compare the evolution of the simulated system with the evolution of the experimental system.

Let us first compare regime (3) and (4) of Fig. 3.6. For low interaction parameters $\widetilde{K}_{\mathrm{I}}$ (black lines in Fig. 3.9a) we observe an initial period that is needed for the system to organise into whirl-like structures. After this time lag, the number of whirls and their mean area both remain stable. In particular, the mean area of the whirls is stable around $1.5A_0$, meaning that the agents in a whirl are slightly straightened as an effect of the interaction with the heighbours. The stability of the whirls is also apparent by looking at the age of the whirls τ_{age}, that grows monotonously with time.

In contrast, at high interaction parameters (cyan lines in Fig. 3.9a), the behaviour of the system is more irregular. The decrease of n_{w} with time is consistent with the fact that the agents tend to aggregate into few large whirls. These whirls are not stable and their area tends to exceed A_0 several times. As a consequence of the growing area, the whirls open up to swarm. This causes a sharp drop in the mean whirl area as well as in the mean age of the whirls.

Regimes (1) and (2) of Fig. 3.6 are characterised by low friction. At low interaction parameters (black lines in Fig. 3.9b), n_{w} and the mean whirl area are stable. However, note that the mean area is closer to A_0 than in the high friction case. This happens because low frictions correspond to quickly solved deformations. Consistently with the high friction case, at low friction and high interaction parameters (cyan lines in Fig. 3.9b) there are less whirls. In this case, the mean whirl area is significantly below A_0, consistently with the fact that, in these conditions, the agents are basically embedded into one another. High interaction parameters cause the whirls to open up also in the presence of low friction, as can be seen from the cyan line in the $\langle\tau_{\mathrm{age}}\rangle$ plot in Fig. 3.9b.

3.6.4 The effect of friction

To better investigate the role of friction in our simulations, let us consider how the dependence of selected quantities on $\widetilde{K}_{\mathrm{I}}$ changes with varying $\widetilde{\Gamma}$. To this aim, we define the quantity $\widetilde{K}_{\mathrm{I}}^{*} = \widetilde{K}_{\mathrm{I}}(N_{\mathrm{n}}\sqrt{2\pi e}\widetilde{F}_{\mathrm{P}})^{-1}$. This way, the blue line in the diagram of Fig. 3.4b, corresponding to Eq. (3.25), is identified by $\widetilde{K}_{\mathrm{I}}^{*} = 1$, while the red line, corresponding to Eq. (3.26), is identified by $\widetilde{K}_{\mathrm{I}}^{*} = 1 - 1/e$.

We first compute the mean number of whirls as a function of $\widetilde{K}_{\mathrm{I}}^{*}$. The quantity $\langle n_{\mathrm{w}}\rangle$ is the number of whirls per frame averaged over the last fifth of the simulation time.

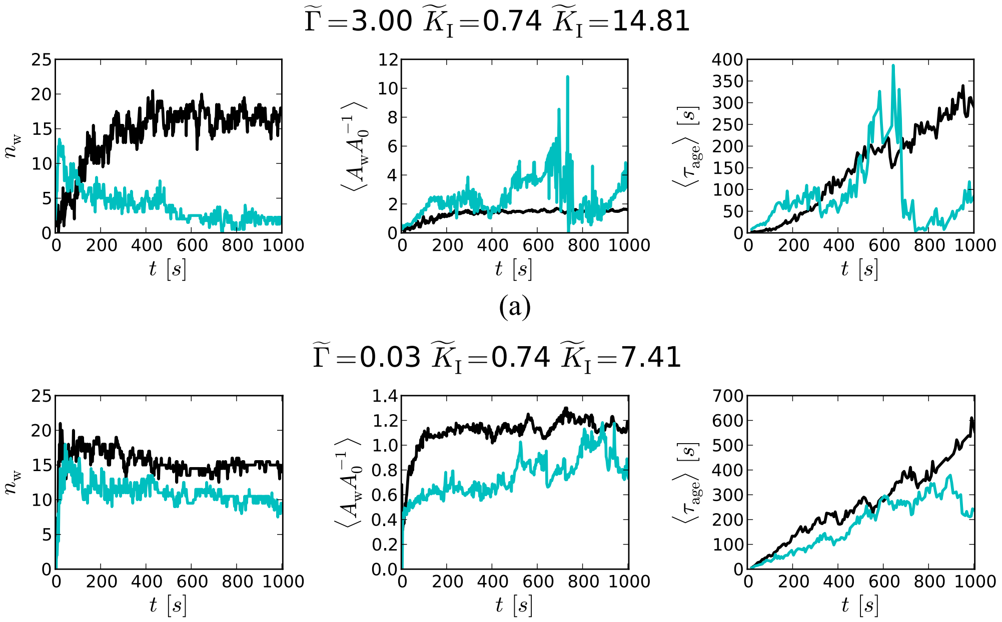

(a)

(b)

Figure 3.9: Comparison of the number of whirls n_w, normalised mean size $\langle A_\mathrm{w}A_0^{-1}\rangle$ and mean age τ_age for low (black) and high (cyan) interaction parameters. (a) At high frictions, whirls are stable in size and number at low $\widetilde{K}_\mathrm{I}$ (black), while at high $\widetilde{K}_\mathrm{I}$ (cyan) the agents tend to aggregate in few whirls of unstable size, that are prone to collapse. (b) Low frictions show the same phenomenon, although in a milder manner. High values of $\widetilde{K}_\mathrm{I}$ (cyan) lead to less whirls and fluctuating sizes.

Typically, $\langle n_\mathrm{w}\rangle = 0$ if there is no interaction between the agents, it peaks before $\widetilde{K}_\mathrm{I}^* = 1$ and then decreases (3.10a). Increasing friction shifts the peak towards lower $\widetilde{K}_\mathrm{I}^*$, while the decrease of $\langle n_\mathrm{w}\rangle$ at higher interaction parameter becomes faster.

As a second step, we compute the mean angle $\alpha = \langle \kappa_0 L\rangle$, averaging over the agents over the last fifth of each simulation. Figure 3.10b shows that the agents tend to straighten with increasing interaction parameter. Increasing the friction makes the straightening more pronounced. This is coherent with the increased persistency of the deformations.

We can therefore say that increasing $\widetilde{\Gamma}$ decreases the number of whirls while, at the same time, reduces the curvature of the agents. In other words, high values of $\widetilde{\Gamma}$ favour the formation of dense swarms rather than whirls.

3.6.5 Spatial ordering

In order to quantify the spatial ordering of the system we measure the pair correlation function $g(r)_t$ (as done, for example, in [98]):

$$g(r)_t = g(|\mathbf{r} - \mathbf{r}'|)_t = \rho_0^{-2}\langle \rho(\mathbf{r},t)\rho(\mathbf{r}',t)\rangle_t \tag{3.32}$$

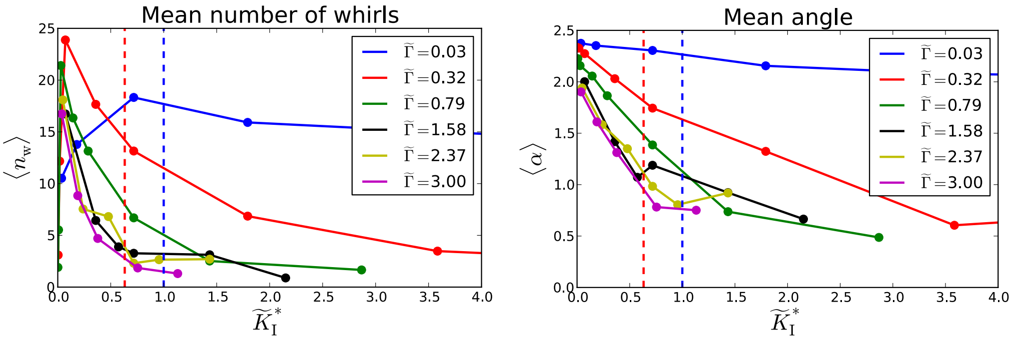

(a) (b)

Figure 3.10: (a) Mean number of whirls for different frictions $\widetilde{\Gamma}$ as a function of the normalised interaction parameter $\widetilde{K}_\mathrm{I}^*$. Increasing friction causes a more pronounced decrease in $\langle n_\mathrm{w} \rangle$ with growing $\widetilde{K}_\mathrm{I}^*$. In addition, the $\widetilde{K}_\mathrm{I}^*$ corresponding to the peak in $\langle n_\mathrm{w} \rangle$ is lower at higher frictions. (b) The agents tend to straighten as a result of increasing interaction parameters, that is to say a decrease in the chance of overlap. The straightening is more rapid the higher the friction, because of the pronounced persistency of the deformations.

with $\rho(\mathbf{r}, t)$ the number density of the nodes at position $\mathbf{r}$ and time t. The pair correlation function is averaged over the last fifth of the simulation time, when the configuration of the system is qualitatively stable, though dynamic.

Figure 3.11 shows that the system exhibits no long range spatial ordering. In general, for both low and high frictions, low interaction parameters favour the formation of stable whirls of size comparable with the trajectory of a free sporozoite (blue curves, the peaks are compatible with an agent's length, i.e. with the size of one whirl). At low friction (Fig. 3.11a), increasing the interaction parameter leads to a loss of spatial ordering, determined by the frequent collisions that have a relevant elastic component. At high friction (Fig. 3.11b), increasing the interaction parameter leads to a longer correlation length, motivated by the fact that the friction dominated collisions result in large aggregates of agents, that can become comparable with the size of the simulation box, thereby leading to major border effects.

3.7 Other features

3.7.1 Gaussian propulsion forces

Instead of considering the propulsion force constant for each agent, we now consider a Gaussian distribution of propulsion forces, so that also the ratio $\widetilde{F}_\mathrm{P}/\widetilde{\Gamma}$ and the steady state speed of the agents are Gaussian distributed. We consider as above $N_\mathrm{a} = 400$ agents migrating within a square simulation box of size $6\widetilde{L}$ with periodic boundary conditions. In particular, the standard deviation is set to $0.25\widetilde{F}_\mathrm{P}^0$, and the ratio $\widetilde{F}_\mathrm{P}^0/\widetilde{\Gamma} = 0.11$.

In general, in a system of agents with Gaussian distributed propulsion forces, the changes

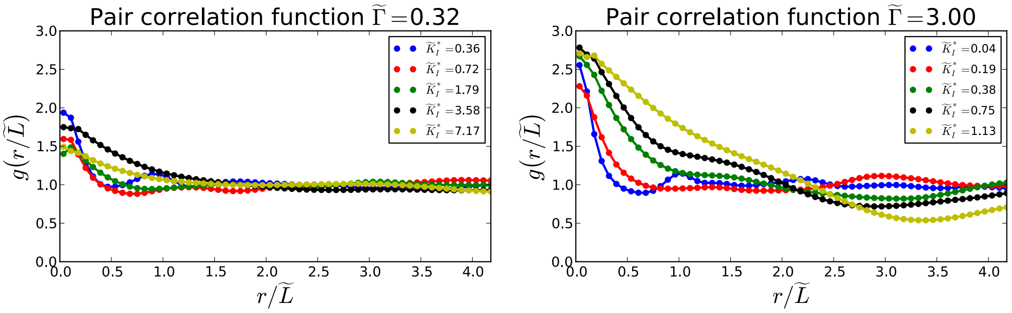

(a) (b)

Figure 3.11: (a) At low frictions, despite the formation of stable whirls, the system exhibits no long range order. In fact, the spatial correlation is lost aroung $r/\widetilde{L} \simeq 1$, which identifies the typical length associated to a single whirl. (b) At high frictions whirls are systematically unstable: their size increases till they rupture and, particularly at high interaction parameters, their size can become comparable with that of the simulation box. Consequently, correlations are long range but do not correspond to spatial ordering, but rather to border effects.

in whirl size are less dramatic than in the case of uniform propulsion. In particular, the whirls are less prone to deform, rupture and swarm as represented in Fig. 3.7. In Fig. 3.12 the black lines refer to a system with uniform propulsion, while the green lines refer to a system with Gaussian distributed propulsion forces.

At low interaction parameters (Fig. 3.12a) there is no obvious difference in the whirl properties and evolution between the Gaussian and uniform cases. However, at higher interaction parameters (Fig. 3.12b), when overlap becomes unlikely, the system with Gaussian propulsion forms more whirls and with a more stable shape. This feature is visible from the $\langle A_{\mathrm{w}} A_0^{-1} \rangle$ plot, in which the green line does not show any of the prominent peaks that characterise the black line. In fact, whirls in the case of Gaussian propulsion deform less than those in the case of uniform propulsion. This is a consequence of the presence of agents with different speeds. Indeed, the typical arrangement of the agents in a whirl is mixed, but the fastest agents tend to be confined in the middle of the whirl, while the slower ones define the outer and inner borders of the whirl (Fig. 3.13). In other words, the effect of the slow agents is to channel the fast ones, thereby limiting the deformations of the whirls.

Attraction Motivated by the increased stability in shape and size of the whirls formed by agents with Gaussian distributed propulsion forces, we now investigate whether a short range attractive interaction between the agents can contribute to further stabilise the structures. To this aim, we assign to each pair of nodes (i, j) belonging to different agents

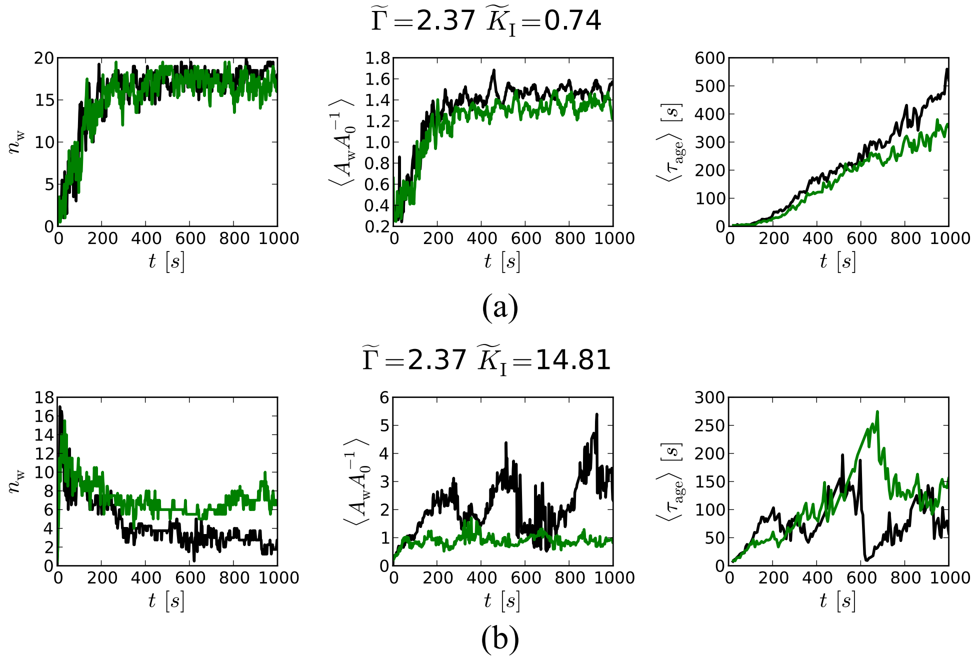

Figure 3.12: Comparison of whirls properties in time for the case of uniform propulsion (black) and of Gaussian propulsion (green). (a) At low interaction parameters $\widetilde{K}_{\rm I}$ there is no difference between the two cases, because the interactions between the agents are limited. (b) At high values of $\widetilde{K}_{\rm I}$, the system with the Gaussian distributed propulsion forces typically forms more whirls and these whirls are stable in size.

a distance dependent energy:

$$E_{\rm attr}^{i,j} \propto \frac{1}{1+\exp(-2\lambda(d_{i,j}-d_0))} \tag{3.33}$$

with $d_0 = 4\sigma$. As a consequence, nodes i and j are attracted towards each other by a force with magnitude proportional to λ:

$$F_{\rm attr}^{i,j} \propto \frac{2\lambda\exp(-2\lambda(d_{i,j}-d_0))}{[1+\exp(-2\lambda(d_{i,j}-d_0))]^2} \quad . \tag{3.34}$$

With $\lambda = 0$ we retrieve the case of Gaussian propulsion discussed in the first part of this section, while increasing λ the agents tend to stick to each other. Note that, with this set up, the agents tend to aggregate but loose the ability to slide along each other, because of the discretisation given by the presence of the nodes. In order to avoid this issue due to the agents not being defined as continuous, we allow the attractive interaction to displace the nodes only in a direction orthogonal to their direction of movement. Wether the displacement takes place to the left or to the right depends on the neighbours' density to the left or to the right of the direction of motion of the node, respectively.

Despite considering values of λ spanning three orders of magnitude, we do not find any

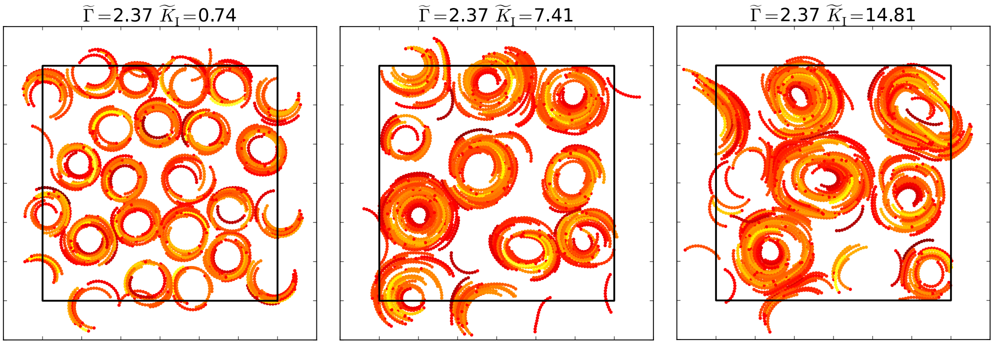

(a) (b) (c)

Figure 3.13: Snapshot of simulations with the agents propelled by Gaussian distributed $\widetilde{F}_{\mathrm{P}}$. Faster agents (towards yellow) typically localise in the bulk of a whirl, while the slower agents (towards red/brown) preferentially localise at the internal and external borders of the whirls. Effectively, this prevents swarming and improves the stability of the whirls at high interaction parameters, both in terms of shape and size preservation.

relevant influence on the properties stemming from the Gaussian propulsion (Fig. 3.14). There could be several reasons behind this result. On one side, the interaction scheme may be insufficiently accurate. For example, it could be a better option to devise an interaction scheme that has also an influence on the propulsion force. Furthermore, we have considered a simple viscous interaction between the agent and the substrate. It is possible that this has to be refined before implementing the details of a mutual attraction scheme.

3.7.2 Different curvatures

Let us now consider the usual $N_{\mathrm{a}} = 400$ agents migrating within a square simulation box of size $6\widetilde{L}$ with periodic boundary conditions. We set the constant ratio $\widetilde{F}_{\mathrm{P}}/\widetilde{\Gamma} = 0.11$, while we vary the rest curvature of the agents. In particular, let us consider a system consisting of $N_{\mathrm{a}}/2$ straight agents and $N_{\mathrm{a}}/2$ agents with curvature κ_0.

As Fig. 3.15 shows for a representative friction $\widetilde{\Gamma} = 2.37$, straight agents (in green) tend to arrange into straight moving clusters, while bent agents (in blue) are responsible for whirl formation. This separation of behaviours is sharp at low $\widetilde{K}_{\mathrm{I}}$, when overlap is favoured and mutual deformations of the agents are very limited (Fig. 3.15a). As the interaction parameter grows, straight and bent agents start to mix, generating whirls and swarms that include both populations (Figs. 3.15b and 3.15c).

3.7.3 The effect of density

We know from the previous part of this chapter that moderate-to-high frictions, coupled to low interaction parameters, lead to the formation of stable whirls when we consider a number of agents $N_{\mathrm{a}} = 400$. Keeping a square simulation box of size $6\widetilde{L}$ with periodic

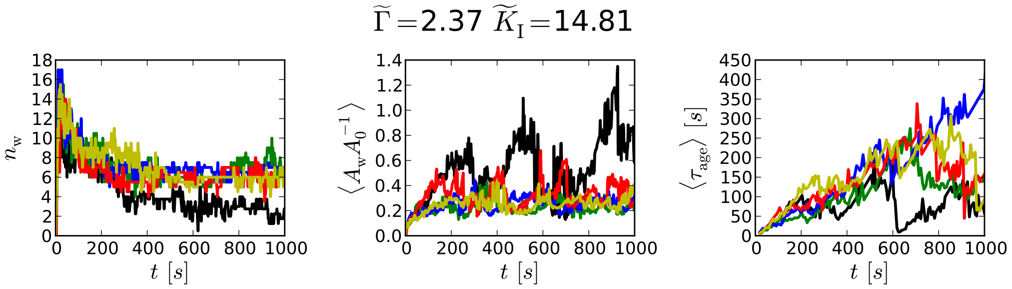

Figure 3.14: Time dependence of whirl properties for agents with Gaussian distributed propulsion forces and mutual short range attraction. Irrespective of the attraction being strong or weak, it does not modify significantly the stability of the Gaussian propelled whirls. The black curves refer to uniform propulsion and the green to Gaussian propulsion with no attraction. The blue, red and yellow curves refer to Gaussian propelled agents with attraction parameter $\lambda = 5$, 50, 200, respectively.

boundary conditions, we now consider the effect of the density of agents on the whirl formation.

Figure 3.16 refers to systems with $\widetilde{\Gamma} = 2.37$ and $\widetilde{K}_{\mathrm{I}} = 0.74$ and varying number of agents. The black, green, blue, red and yellow curves refer, respectively, to $N_{\mathrm{a}} = 400$, 324, 225, 100 and 64. The formation and evolution of the whirls is strongly influenced by the density: the presence of more agents leads to more whirls and long-lived.

At higher interaction parameters the whirls are systematically unstable at $N_{\mathrm{a}} = 400$. This feature is also present at lower densities, although oscillations in the whirl area are less pronounced because of the lower number of agents colliding in a whirl.

3.7.4 Size of the box

The size of the simulation box becomes relevant when the diameter of the whirls becomes comparable with the side of the box. In this case, a whirl appears as a swarm. To test this, we have performed control simulations in a smaller simulation box.

3.8 Conclusion and outlook

In this chapter we have presented an agent-based model, that focuses on the geometrical and structural aspects of self-organised whirls of sporozoites, as observed in the salivary glands of malaria infected mosquitos following preparation. Despite the model being an overly simplified representation of collective sporozoite movement, it is backed up by firmly grounded assumptions and a solid mathematical framework.

Our work provides relevant insights and predictions that are worth reviewing in this conclusive section. As intuitive as it is fundamental, the formation of whirls is tightly linked to the model parasites being curved objects (Fig. 3.15). The curvature leads to

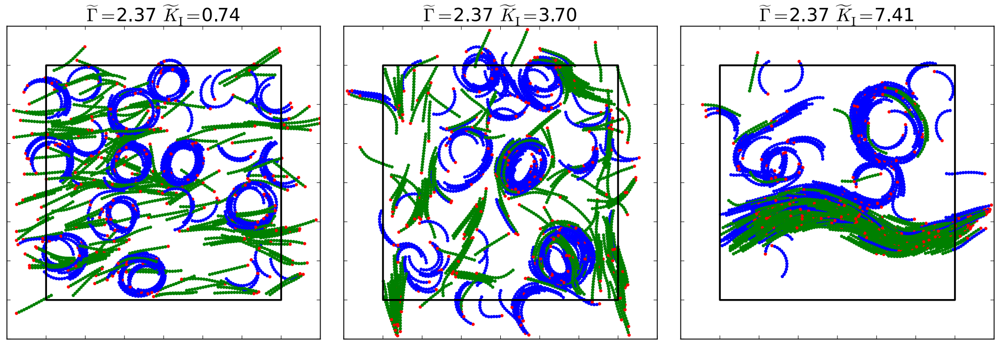

(a) (b) (c)

Figure 3.15: Snapshots of simulations of a population of agents propelled by a constant $\widetilde{F}_P$ and with mixed curvatures. Straight agents (green) tend to form forward moving clusters, while bent agents (blue) are responsible for whirl formation. (a) At low interaction parameters the separation of the structures is sharp. (b,c) Increasing $\widetilde{K}_I$ progressively leads to whirls and swarms involving both straight and bent agents.

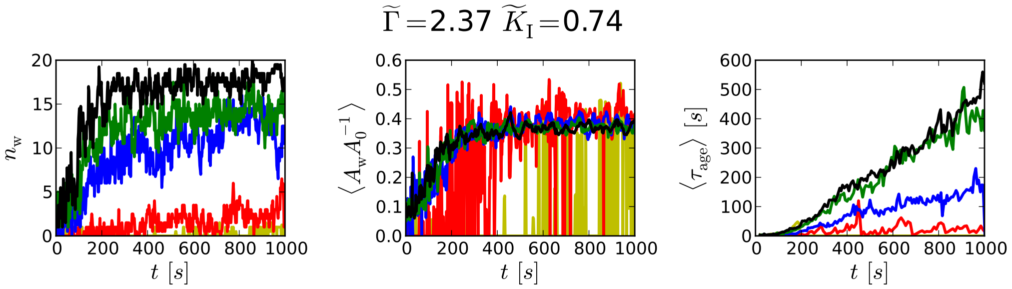

Figure 3.16: At low interaction parameters whirl formation is strongly influenced by the number of agents in the system. Increasing $N_{\rm a}$ leads to more whirls and long-lived. The black, green, blue, red and yellow curves refer, respectively, to $N_{\rm a} = 400$, 324, 225, 100 and 64.

the formation of whirls, but it is alone not enough to guarantee their stability. Indeed, we show that friction, overlap between the agents and their speeds are key factors determining whether whirl-like structures can maintain their size and shape.

In particular, stable whirls are associated with relatively high frictions and overlap probabilities (Fig. 3.6). This is coherent with the idea of the salivary gland as a three-dimensional system delimited by the basal lamina, onto which sporozoites can adhere forming whirls. Such scenario is compatible with whirls having a well defined three-dimensional structure, as well as with the presence within the gland of a bulk of free, motile sporozoites, that could move from the bulk to the membrane and vice-versa.

Additionally, in the model, the stability of the whirls significantly improves if the population of agents shows a distribution of steady state velocities instead of a unique value. In this case, the faster agents form the bulk of the whirls, while the slower agents are localised at the boundaries (Fig. 3.13), effectively implementing confinement.

Overlap between the agents is supported by our qualitative experimental observations, as discussed in Sec. 3.1. In contrast, the prediction about stability being related to the different speeds must be taken more carefully. In our model, each agent is characterised by a constant ratio $\widetilde{F}_\mathrm{P}/\widetilde{\Gamma}$, but in the real system the speeds of individual sporozoites differ on average and vary over time in a not yet fully understood manner [27]. However, from our simplified model we can safely conclude that the speed dynamics plays a role that may be profoundly related to the stability of the whirls and is worth investigating in detail.

For future work, we think that it would be appropriate to consider specific interaction schemes between the agents and the substrate, instead of limiting the treatment to a viscous term. Similarly, the study of interactions between the agents, other than excluded volume, should be extended. While currently there is no experimental evidence of sporozoites plainly sticking to each other within a whirl, this does not rule out some complex, short-range interaction. In fact, sporozoite gliding relies on transmembrane adhesive protein complexes, that allow the parasites to bind to a variety of substrates in a non-specific manner [35]. The idea that the same propulsion machinery could allow for binding between two or more sporozoites, thereby adding compactness to the whirls, is compatible with this scenario.

We think that further experimental work targeting the predictions and open questions of our model could significantly increase the understanding of the formation and stability of sporozoite whirls. It would also allow to define the priority levels of the various features of this complex system, so that the theoretical model could be extended accordingly and be more comparable and predictive.

A promising experimental effort planned for the near future is the three-dimensional imaging of whirl-like structures. Should imaging reveal that whirls typically have a well defined, stable three-dimensional structure, then our model should be extended to include realistic descriptions of both adhesion to the basal lamina and mutual adhesion between the sporozoites. On the other hand, should imaging prove that whirls are typically monolayered, the extension of the model could concern only the adhesion to the basal lamina, neglecting any attraction between the sporozoites. In parallel, the model should deal with the presence of a bulk of non-adherent sporozoites, that could join or leave the plane of imaging.

4 Stick-slip motion for a rod with translational and rotational friction

This chapter is dedicated to the study of a stochastic bond model combining translational and rotational friction. We are motivated by the observation that, for sporozoites gliding circularly on a flat substrate, the two frictional terms must play a comparable role.

We introduce the problem of friction and the various modelling approaches in Sec. 4.1, focusing on the relation with biological systems. Section 4.2 presents our theoretical framework for the study of combined translational and torsional stochastic friction. There we identify several scaling regimes: such analysis is of high importance in the interpretation of the results presented in Sec. 4.3. We then conclude in Sec. 4.4.

4.1 Introduction

Sliding friction between two surfaces moving relatively to each other occurs in a wide range of physical and biological systems [99]. While traditionally studied on a macroscopic level, the modern understanding focuses more on the relation with the underlying microscopic processes. High precision experiments of sliding friction can be performed, for example, using the surface force apparatus or atomic force microscopy. These studies helped a better understanding of biological systems involving sliding friction [100], like rolling adhesion of white blood cells in the vasculature [16], or spreading and migration of animal cells over planar substrates [39]. In the latter case, the surface of the cell moves relatively to the substrate mainly due to retrograde flow of the actin cytoskeleton.

A generic theoretical framework for the study of sliding friction is provided by multi-contact (or bond) models [42]. This class of models considers an ensemble of bonds that form and rupture at the interface between two surfaces moving relatively to each other [50, 101, 102]. Depending on the system, bonds might represent, among others, van der Waals contacts, capillary bridges, asperities or molecular bonds. Bonds are typically assigned local elasticity, rupture rate and rate of bond formation. Both experiments and bond models dealing with the forced sliding of surfaces typically find, at intermediate driving speeds, enhanced fluctuations in the velocity of the driven surface [42, 50–52]. This phenomenon is commonly referred to as *stick-slip regime*.

Interestingly, the conceptual framework to model biomolecular bonds is the same as for many inert physical systems, because both cases rely on the thermally activated crossing of

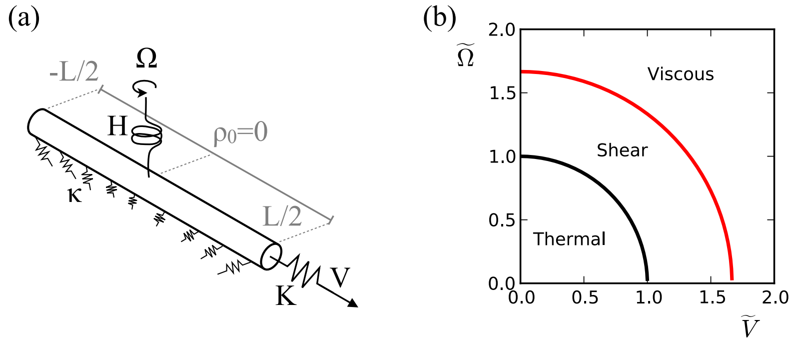

Figure 4.1: (a) A rod is driven by linear and rotational springs driven by fixed speeds. Stochastic bonds connect the rod to the substrate and lead to stick-slip behaviour. (b) Phase diagram, based on Eq. (4.4), showing the boundaries between the thermal and the shear regime (black), and between the shear and the viscous regime (red). Parameters: $M = L = 1$, $\xi = 0.5$, $\rho_0 = 0$, $V_\beta = 0.12$ and $V_{\text{sh}} = 0.2$.

a force dependent energy barrier. Without relative movement of the two opposing surfaces, adhesive biological systems have been modelled as an ensemble of discrete bonds [43, 103]. With movement, the equations include convection terms and often can be solved in a mean field approximation [45–49]. These models predict not only stick-slip regimes at intermediate driving speeds, but also biphasic relations between flow speed and traction force, as observed experimentally, for example for the retraction of filopodia by neuronal cells [53] or actin retrograde flow over adhesion sites [54].

Although much progress has been achieved with the help of stochastic bond models, up to now they have been used mainly to study unidirectional sliding friction. However, there exist important situations in which translocation is combined with rotation. One instructive example is the migration of malaria parasites on flat surfaces and in obstacle arrays [38]. Since these are crescent-shaped cells that glide in circular trajectories, rotational friction is expected to play a similarly important role as does translational friction. Experimentally it has been shown that malaria parasites exhibit stick-slip behaviour as well as a complicated dynamics of their adhesion sites [27], but a fundamental understanding of the underlying bond dynamics is still missing. Similar issues also arise for other migrating cells, like turning keratocytes [104], as well as for synthetic microgliders or passive friction with rotation, for example in the case of torsional bearings [105].

Note that the stochastic dynamics at the adhesive interface does not necessarily differ for a system driven by external forces versus a self-propelled system like a cell. In fact, self-propelled particles are often described by a Langevin equation for a massive particle driven by an effective force and balanced by viscous interactions with the environment [89, 106]. Within such approach, mass describes persistency of motion and the motility force describes the effective outcome of a more complex force distribution at the sub-cellular level. Circular motion of self-propelled particles has been discussed before for swimming bacteria and synthetic microswimmers [55, 89, 107], but it has not been addressed yet in the context of gliding cells.

Here we introduce and analyse a model for stick-slip motion with both translational and rotational components. Our model can be applied to a slider driven by an external force as well as to an active glider moving over a substrate. We consider a moving rod that is connected to the substrate by bonds that open and close stochastically. The rod undergoes both translation and rotation due to linear and rotational springs that are pulled and rotated with constant linear and angular speeds, respectively. Our main finding is that the rotational component strongly enhances the stick-slip regime and that patches of closed bonds form at the interface between the moving object and the substrate if the association rate is velocity dependent. These findings are reminiscent of the complex adhesion dynamics observed during the migration of naturally curved malaria parasites [27].

4.2 Friction model

4.2.1 Definition

Our modelling approach is motivated by earlier work on translational sliding friction [50]. Consider a straight rod of mass M and length L, driven by both a linear and a rotational spring as shown schematically in Fig. 4.1a. The linear spring has elastic constant K and moves with a fixed speed V in the direction of the rod. The rotational spring is anchored to the rod at ρ_0, has spring constant H and is rotated with a fixed angular speed Ω. Attached to the rod are N_b equally spaced springs, each with zero rest length and elastic constant κ. Together they generate the adhesive force F_b and the adhesive torque T_b. We separate the movement of the centre of mass $\mathbf{R}$ from that of the orientation angle θ:

$$M\ddot{\mathbf{R}} + \xi\dot{\mathbf{R}} + F_\mathrm{b}\hat{\boldsymbol{\theta}} + K(L_\mathrm{tot} - Vt)\hat{\boldsymbol{\theta}} = 0 \ , \tag{4.1}$$

$$I\ddot{\theta} + \eta\dot{\theta} + T_\mathrm{b} + H(\theta_\mathrm{tot} - \Omega t) = 0 \ . \tag{4.2}$$

Here L_tot is the total length of the two-dimensional trajectory described by the centre of mass and θ_tot is the total angle by which the rod has rotated. The terms ξ and η are linear and angular viscosities, respectively.

The adhesive force and torque undergo fluctuations due to stochastic opening and closing of the bonds. We introduce the quantities q_b to represent the status of a bond: $q_\mathrm{b} = 1$ for a close bond and $q_\mathrm{b} = 0$ otherwise. We then have:

$$F_\mathrm{b} = \sum_{\mathrm{b}=1}^{N_\mathrm{b}} q_\mathrm{b} f_{\mathrm{b}||}, \ \ T_\mathrm{b} = \sum_{\mathrm{b}=1}^{N_\mathrm{b}} q_\mathrm{b}(\rho_\mathrm{b} - \rho_0) f_{\mathrm{b}\perp} \ . \tag{4.3}$$

Here $f_{\mathrm{b}||}$ and $f_{\mathrm{b}\perp}$ are the components respectively parallel and orthogonal to the rod of the force exerted by a bond. The position of the bond on the rod is given by ρ_b.

In modelling bond dynamics, we assume the usual slip bond dissociation rate, $k_{\text{off}} = k^0_{\text{off}} \exp(f/f^*)$, that introduces a spontaneous dissociation rate k^0_{off} and a critical force f^*, beyond which the rupture rate increases dramatically [43]. This also defines a thermal velocity $V_\beta = k^0_{\text{off}} f^*/\kappa$ at which the rate of detachment of a null length bond equals the rate of decrease of the energy barrier upon stretching. For association, we allow for a velocity dependent rate, $k_{\text{on}}(v) = k^*_{\text{on}} + (k^0_{\text{on}} - k^*_{\text{on}})g(v)$ with a step function $g(v) = (1 + \exp((v - V_{\text{sh}})/dv))^{-1}$. With this setup, rebinding becomes less likely if the driving speed exceeds a critical speed V_{sh}, which in general we expect to be larger than V_β.

Because this paper is motivated by the case of self-propelled objects, here we focus on low friction cases. Taking into account inertia effects ($M/\xi > \xi/K$ and $I/\eta > \eta/(HL^2)$) allows to study the effect of persistent movement on the dynamics of the stochastic bonds.

4.2.2 Timescales

More specifically, from the equations of motion 4.1 and 4.2 we can extract several relevant timescales. Considering the translational dynamics, we have the typical relaxation time of the driving spring $t_V = \xi/K$ and the timescale regulating inertia effects $t_M = M/\xi$. Similarly, for the rotational dynamics, we have the typical time for relaxation of the driving rotational spring $t_\Omega = \eta/(HL^2)$ and the timescale associated to inertia effects during rotation $t_I = I/\eta$. We can further define two timescales of bond relaxation, namely $t_{\text{b}} = \xi/\kappa$ for the translational case and $t'_{\text{b}} = \eta/(\kappa r_b^2)$ for the rotational case.

These timescales are represented in Fig. 4.2 as functions of the friction coefficients ξ and η. In the limit of high friction inertia plays a negligible role and t_M and t_I tend to zero (light blue curves). In contrast, for sufficiently low friction, t_M compares with t_V (grey in Fig. 4.2a) and t_I compares with t_Ω (grey in Fig. 4.2b), which implies that the driving springs are influenced by the mass of the rod. It follows that, in the event of a sudden rupture of the bonds connecting the rod to the substrate, the non-negligible mass of the rod can generate oscillations of the driving springs.

4.2.3 Scaling regimes

With the assumption $V_\beta < V_{\text{sh}}$, we expect three different regimes. Below V_β bonds break spontaneously (*thermal regime*). Between V_β and V_{sh}, bonds break by shear force (*shear regime*). Above V_{sh}, rebinding becomes less likely and the movement is mainly opposed by the viscous forces (*viscous regime*). However, in our case we consider both translation and rotation, thus these regimes occur in a two-dimensional phase space of linear and angular velocities. By comparing the bond velocity $|\mathbf{v} + \boldsymbol{\omega} \times (\rho_{\text{b}} - \rho_0)\hat{\boldsymbol{\theta}}|$ with either $V_{\text{c}} = V_\beta$ or $V_{\text{c}} = V_{\text{sh}}$, we obtain the following conditions for the transition lines:

$$\left[V^2 + \Omega^2 \left(\frac{MV}{\xi} - \rho_{\text{b}} + \rho_0\right)^2\right]^{\frac{1}{2}} = V_{\text{c}} \ . \tag{4.4}$$

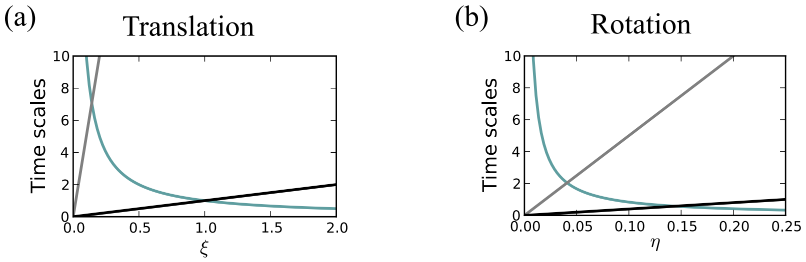

Figure 4.2: Friction dependent timescales of the model. (a) Translation. The timescale regulating inertia effects $t_M = M/\xi$ (light blue), the timescale of bond relaxation $t_\mathrm{b} = \xi/\kappa$ (black) and the typical relaxation time of the driving spring $t_V = \xi/K$ (grey). (b) Rotation. The timescale regulating inertia effects $t_I = I/\eta$ (light blue), the position dependent timescale of bond relaxation $t'_\mathrm{b} = \eta/(\kappa r_\mathrm{b}^2)$ at $r_\mathrm{b} = L/2$ (black) and the typical relaxation time of the rotational driving spring $t_\Omega = \eta/(HL^2)$ (grey). At low frictions, the inertia timescale and the relaxation time of the driving springs are comparable. In this situation, the rod can generate oscillations in the driving springs. Parameters: $M = L = \kappa = 1$, $K = 0.02$, $H = 0.02$, $I = ML^2/12$.

The corresponding phase diagram is shown in Fig. 4.1b, with the linear speed expressed as $\widetilde{V} = V/V_\beta$ and the angular speed expressed as $\widetilde{\Omega} = \Omega/(2V_\beta/L)$. Equation (4.4) also shows that different regimes are simultaneously present on the rod given a non-zero Ω, in marked contrast to the purely translational case.

In the following, we present results from numerical simulations performed using a parameter set that is representative of the typical behaviour of the system: $M = L = \kappa = 1$, $\rho_0 = 0$, $K = 0.02$, $H = 0.02$, $\eta = 0.01$, $\xi = 0.5$, $k^0_\mathrm{off} = k^0_\mathrm{on} = 30$, $k^*_\mathrm{on} = 0$, $f^* = 0.004$, $dv = 0.05$ and $V_\mathrm{sh} = 0.2$. Times $\widetilde{t}$ are measured in units of $t_\mathrm{b} = \xi/\kappa$. It is necessary to define ξ also in the case of pure rotation, because stochasticity in the bond dynamics in general leads to non-zero velocities along the rod.

4.3 Results

4.3.1 Pure translation

We first discuss the case of pure translation ($\Omega = 0$, $H = 0$). As reported earlier [50], if the slider is driven with a velocity V close to V_sh, we obtain a stick-slip behaviour with a well defined period, an example of which is shown in Fig. 4.3a for a simulation with $N_\mathrm{b} = 300$ bonds.

Since all positions are equivalent in this case, the dynamics is uniform along the rod. Although a finite mass and the velocity dependent rebinding rate are essential to get the observed periodic behaviour, these two conditions are not required to obtain stick-slip behaviour in general. In fact, it has been shown that also an overdamped system ($M = 0$) with constant association rate ($g(v) = 0$) shows a stick-slip regime, albeit with a much less regular time course [42, 47, 49].

This stems from the presence of two conceptually different stick-slip regimes. The first one is that associated to the bistability of the relation between the speed of the rod and the traction force exerted by the close bonds [45]. The second one is that studied in our model and first proposed, though not explicitly identified, in [50]. The source of the regularity in the stick-slip patterns in our system is the combination of two contributions: the first is inertia and the second is the transition speed V_{sh}, that corresponds to a sharp drop in the binding rate. Driving the rod at speeds slightly above V_{sh} leads to a rapid decrease in the number of close bonds, because the binding rate drops, while the close bonds become increasingly stretched and then open. For simplicity, suppose that all the bonds are broken and the binding rate is zero for speeds of the rod above V_{sh}. The sudden decrease in the potential energy of the system must be transferred into kinetic energy of the rod and/or dissipated due to viscosity.

In the low friction case ($t_V \sim t_M$) the rod gains significant kinetic energy as a consequence of a rupture cascade. Before viscosity can have any effect, the speed of the rod decreases below V_{sh} due to the compression of the driving spring. The bonds start closing in the presence of a loaded driving spring, that then relaxes and accelerates the rod to a speed slightly above V_{sh}, thus discouraging rebinding and causing the cycle to repeat.

In case of an overdamped system, the potential energy released following a rupture cascade is instantly lost due to viscosity only. There is no change in the kinetic energy of the rod and the driving spring is not influenced by the bond rupture cascade. It follows that there cannot be any spring dependent regular stick-slip period for driving speeds around V_{sh}.

To better understand the interplay between traction force and velocity, we can use a mean field approximation. Defining $r = k_{\mathrm{off}}/k^0_{\mathrm{off}}$, $r^*_{\mathrm{on}} = k^*_{\mathrm{on}}/k^0_{\mathrm{off}}$, and $\Delta r = (k^0_{\mathrm{on}} - k^*_{\mathrm{on}})/k^0_{\mathrm{off}}$, a self-consistent derivation [49] leads to the force-velocity relation:

$$F(v) = N f^* \frac{r^*_{\mathrm{on}} + \Delta r\, g(v)}{r^*_{\mathrm{on}} + \Delta r\, g(v) + r} \ln r \ . \tag{4.5}$$

Note that, because of the self-consistent derivation, r depends non-linearly on v ($v = V_\beta r \log r$). A similar biphasic relation has been found before numerically [50]. For $\Delta r = 0$, this expression simplifies to the one given in [49].

The relation in Eq. 4.5 shares with that in [49] the biphasic character, namely the existence of a maximum in the traction force at finite speed. It has been shown in a number of works [45–47, 101, 108] that this feature is associated with the emergence of collective bond behaviour at the transition between static and kinetic friction. However, while the force-velocity relationship for a constant on-rate ($\Delta r = 0$) increases in a much steeper manner than it decreases with speed, this is no longer true in our case. In fact, introducing $\Delta r > 0$ causes $F(v)$ to decrease more steeply around $v = V_{\mathrm{sh}}$. Stick-slip around V_{sh} is not associated to the bistability of the force-velocity relationship. Instead V_{sh} is a critical velocity that generates a periodic stick-slip behaviour for low frictions only, i.e. in

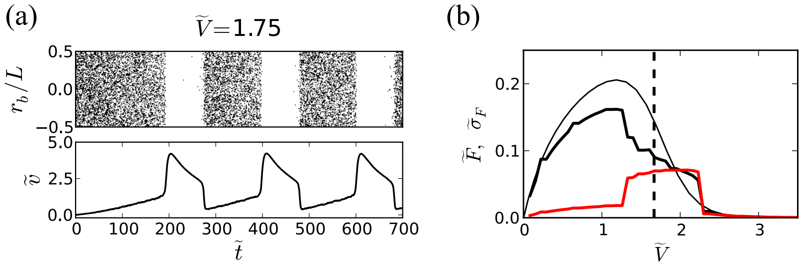

Figure 4.3: Stick-slip motion for translational driving. (a) Time dependence of bond configuration and speed. Close bonds are represented as black dots. (b) Mean field force-velocity relation $\widetilde{F}(\widetilde{V})$ (thin black), versus that determined numerically (thick black). The two curves differ around the transition velocity $\widetilde{V}_{\mathrm{sh}}$, that corresponds to an increase in the fluctuations in the traction force $\widetilde{\sigma}_F$ (red). $\widetilde{F}$ and $\widetilde{\sigma}_F$ are normalised by Nf^*.

the case of persistent movement.

Figure 4.3b shows that the mean field result for $F(v)$ (thin black line, Eq. 4.5) corresponds well to the numerical result (thick black line). Deviations occur around the dashed line, where $v \simeq V_{\mathrm{sh}}$. As shown by the thick red line ($\widetilde{\sigma}_{\mathrm{F}}$), this corresponds to the region in which the adhesion force strongly fluctuates. The quantity $\widetilde{\sigma}_F$ is the standard deviation of the adhesion force throughout the simulation time.

4.3.2 Pure rotation

The case of pure rotation ($V = 0$, $K = 0$) is characterised by a position dependent bond dynamics and by the simultaneous presence of the different bond regimes on the rod. From Eq. (4.4), the *shear*-to-*viscous* transition is localised on the rod around $\rho_{\mathrm{b}}^{\pm} = \rho_{\mathrm{c}} \pm \Omega^{-1}[V_{\mathrm{sh}}^2 - V^2]^{1/2}$. Stick-slip patterns localise around $\rho_{\mathrm{b}}^{\pm}$, and extend along the rod in a parameter dependent manner (Fig. 4.4a).

For $V = 0$ we can derive an analytical expression for the bond profile. In steady state the probability p_{on} of a bond being close satisfies $0 = -\langle p_{\mathrm{on}} k_{\mathrm{off}} \rangle_t + (1 - \langle p_{\mathrm{on}} \rangle_t) k_{\mathrm{on}}$, where $\langle . \rangle_t$ denotes an average over time. We can rewrite $\langle p_{\mathrm{on}} k_{\mathrm{off}} \rangle_t$ as $k_{\mathrm{off}}(t^*) \langle p_{\mathrm{on}} \rangle_t$, with t^* a typical timescale for bond ageing defined as $t^* = (k_{\mathrm{off}}^0 + \kappa |\rho_{\mathrm{b}}| \Omega / f^*)^{-1}$. The bond profile is then given by $\langle p_{\mathrm{on}} \rangle_t = (1 + k_{\mathrm{off}}(t^*)/k_{\mathrm{on}})^{-1}$, where in k_{on} we use $v = \Omega |\rho_{\mathrm{b}}|$. Figure 4.4b compares the predicted (cyan) with the simulated (solid black line) bond profiles in the presence of stick-slip patterns. The agreement between the predicted and simulated curves deteriorates where stick-slip patterns are present, while we find very good agreement for low and high $\widetilde{\Omega}$ values.

Similarly to the case of pure translation, we can derive a torque-velocity relationship $T(\omega)$ via a self-consistent mean field treatment:

$$T(\omega) = \frac{Nf^*}{L} \int_{-\frac{L}{2}}^{\frac{L}{2}} d\rho \, \rho \frac{r_{\mathrm{on}}^* + \Delta r \, g(\rho\omega)}{r_{\mathrm{on}}^* + \Delta r \, g(\rho\omega) + r} \ln r \quad . \tag{4.6}$$

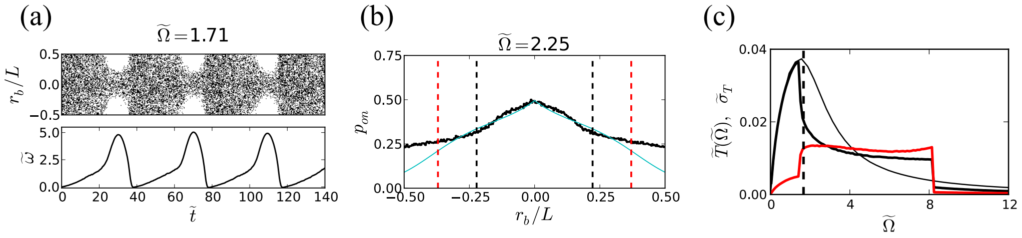

Figure 4.4: Stick-slip motion for rotational driving. (a) Stick-slip dynamics localises in the regions of the rod around the predicted *shear*-to-*viscous* transition. (b) Simulated (solid black line) and theoretical (cyan) bond profiles. The simulated bond pattern deviates from the predicted one in the regions of the rod where stick-slip occurs. The black and red dashed lines denote the *thermal*-to-*shear* and the *shear*-to-*viscous* transitions. (c) Mean field torque-velocity relation $\widetilde{T}(\widetilde{\Omega})$ (thin black), compared with its numerical counterpart (thick black). The deviation from the mean field prediction starts at $\Omega = 2V_{\text{sh}}/L$ and corresponds to increased fluctuations of the torque (red). Traction torque and its fluctuations are normalised by Nf^*L.

In Fig. 4.4c we show the mean field result (thin black line), integrated numerically, compared with the result from the simulation (thick black line). The two curves show good agreement, that deteriorates around the dashed line, corresponding to $\Omega = 2V_{\text{sh}}/L$. This deviation corresponds to the presence of stick-slip bond patterns and, consequently, increased fluctuations in the traction torque. Such fluctuations $\widetilde{\sigma}_T$ are represented as a thick red line in Fig. 4.4c and are computed as the standard deviation of the traction torque throughout the simulation time.

As for the translational case, the appearance of stick-slip is due to the combination of inertia and the transition speed V_{sh}. For a rod driven by the rotational speed only, the linear speed of each bond depends on its position r_{b}. Given Ω, only a fraction of the bonds is moving at speeds around V_{sh} and, consequently, periodic stick-slip only involves parts of the rod. As before, the periodicity in stick-slip stems from the transformation of kinetic energy in potential energy of the driving spring and vice-versa. The region around the anchorage point $\rho_0 = 0$, also centre of mass, of the driving rotational spring always allows a patch of attached bonds, because the velocity of the centre of mass averages to zero.

4.3.3 Translation and rotation

When the rod is driven by both the translational and the rotational springs ($V, \Omega > 0$, $K, H > 0$), the complexity of bond dynamics increases, combining the features of the two limiting situations discussed before (Figs. 4.3 and 4.4). At low values of $\widetilde{\Omega}$ the translation dominates the behaviour of the bonds. Similarly, the rotation determines the bond pattern at low values of $\widetilde{V}$. The typical outcome of the interplay between translation and rotation is a stick-slip pattern localised on the rod (Fig. 4.5a,b,c), matched by regular variations in $\widetilde{\omega}$, $\widetilde{v}_{||}$ and $\widetilde{v}_{\perp}$ (respectively the velocities angular, parallel and orthogonal to

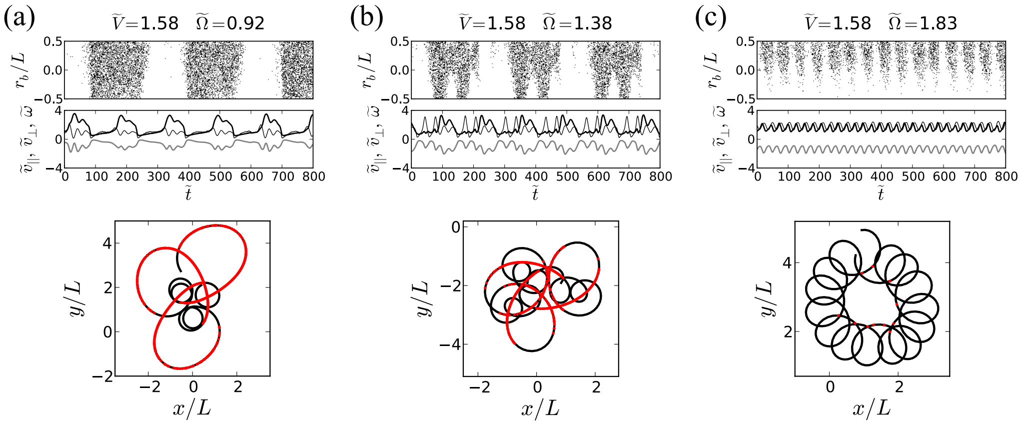

Figure 4.5: Stick-slip motion for roto-translational driving. Both $\widetilde{V}$ and $\widetilde{\Omega}$ contribute to the onset of shear and the bonds form stick-slip patterns that localise on the rod with increasing $\widetilde{\Omega}$. The angular speed of the rod (thin black), the translational speed along the rod (thick black) and perpendicular to it (thick grey) spike upon collective bond detachment. The trajectory of the centre of mass of the rod shows longer stretches (red) corresponding to slip phases.

the rod). This stems from the combination of the *shear*-to-*viscous* transitions at $\rho_{\mathrm{b}}^{\pm}$ with translational speeds high enough to influence the bonds along the whole rod. The complex stick-slip patterns influence the trajectory of the centre of mass of the rod. While constant translational and rotational speeds result in a spiralling trajectory, with radius increasing at speed $MV\Omega/\xi$, the bond dynamics leads to complex trajectories of the centre of mass, with longer stretches associated to slip periods and tighter loops associated to stick configurations.

In Fig. 4.6 we show the fluctuations in the density of closed bonds for different pairs of $\widetilde{V}$ and $\widetilde{\Omega}$. Such fluctuations are computed as the standard deviation of the density of close bonds throughout the simulation time. Our focus in on the low friction case (Fig. 4.6a), for which we can distinguish two main areas in which fluctuations are high, one associated with $\widetilde{V} < \widetilde{\Omega}$ and one with $\widetilde{\Omega} < \widetilde{V}$, both starting at the line of the phase diagram corresponding to the transition from the shear to the viscous regime. While the extension of the anomalous fluctuations beyond this line is parameter dependent, we can identify several persistent features. Bond patterns in the area corresponding to $\widetilde{V} < \widetilde{\Omega}$ are very similar to Fig. 4.4a, apart from the centre of the pattern, that is shifted to $\rho_c = \rho_0 + MV/\xi$. Patterns in the area corresponding to $\widetilde{\Omega} < \widetilde{V}$ are similar to Fig. 4.3a, but become more and more asymmetric with growing $\widetilde{\Omega}$, leading to localised stick-slip patterns in the area where $\widetilde{V}$ and $\widetilde{\Omega}$ assume comparable intermediate values ($\widetilde{\Omega} \sim \widetilde{V} \sim 2$ in Fig. 4.5d).

In the high friction case (Fig. 4.6b) the *shear*-to-*viscous* transition is not associated with anomalous fluctuations, as can be seen from the colormaps and the corresponding scales. This is due to the fact that, for sufficiently high friction, the rod is not able to generate oscillations in the driving springs.

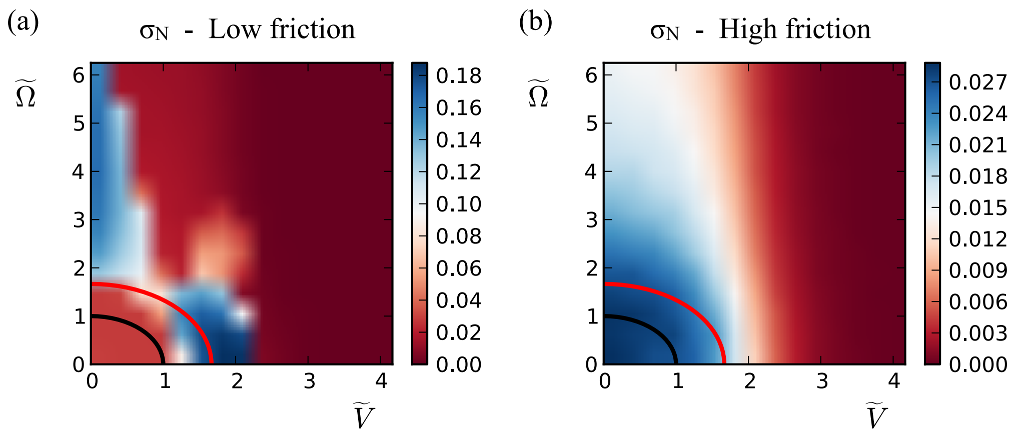

Figure 4.6: Fluctuations in the density of close bonds on the rod. (a) Low friction. Two regions of anomalous fluctuations (blue) can be distinguished, a first, for low $\widetilde{V}$, associated with stick-slip patterns similar to those of Fig. 4.4a and a second, for low $\widetilde{\Omega}$, associated with bond patterns similar to those of Fig. 4.3a. For comparable intermediate $\widetilde{V}$ and $\widetilde{\Omega}$ the bond dynamics is characterised by localised stick-slip patterns ($\widetilde{\Omega} \sim \widetilde{V} \sim 2$ in this case). (b) High friction. The transition velocity V_{sh} is no longer associated with anomalous fluctuations because, for sufficiently high friction, the rod is not able to generate oscillations in the driving springs.

4.4 Conclusion

Here we have studied the behaviour of a rod subject to both translation and rotation. We have shown that the simultaneous presence of both translational and rotational friction, modelled using stochastic bonds, leads to behaviours that are much more complex than in the purely translational case analysed in a previous study [50]. Most importantly, rotation implies that different regimes of bond dynamics are simultaneously present along the rod. Combined with a velocity dependent association rate for the bonds, this leads to the formation of localised adhesion patches. Such stick-slip bond patterns are heterogeneous (Fig. 4.5a,b,c) and are observed in a large region of the $(\widetilde{V}, \widetilde{\Omega})$-plane of the driving speeds (Fig. 4.6a).

The appearance of regularly spaced bond patterns is inherently linked to the presence of the transition speed V_{sh} in the on-rate of the bonds, as well as to the presence of inertia in the system. Without inertia, i.e. in the case of high friction, no regular stick-slip is observed, because the massless rod cannot force the driving springs to oscillate (Fig. 4.6b).

We can connect our findings to the problem of cell motility and the adhesion dynamics between the cell and its substrate. Our results suggest that the observation of regular stick-slip behaviour in motile cells can be linked to persistency in the cell motion in the presence of a change in the adhesion dynamics. For example, in the case of malaria parasites, experiments have shown a semi-regular, dynamic adhesion pattern during circular gliding [27]. We think that the link between persistent motion and stick-slip behaviour deserves further investigations, both in the direction of biological systems, to better understand the complexity of cell motility, but also in the context of inert physical systems like, for example, torsional bearings [105].

5 Circular gliding: theoretical model and experimental data

In this chapter we investigate the connection between the microscopic gliding system of sporozoites and the corresponding changes in the shape of the cell.

In the first part, from Sec. 5.2 to Sec. 5.6, we propose a minimal, experimentally motivated, theoretical description of the gliding machinery of sporozoites. We link the features of the propulsion machinery and its temporal dynamics to the deformations of a thin bent rod, that is meant to capture the effects of the natural curvature of a sporozoite.

In the second part, in Secs. 5.7 and 5.8, we analyse experimental time series of the speed and curvature of gliding Plasmodium *berghei* sporozoites. We interpret the results focusing on the quantitative relation between the propulsion machinery and the shape of the parasites.

Credit for the experimental images we analyse in this chapter goes to the Frischknecht group (Heidelberg University Clinics), specifically to Konrad Beyer. We acknowledge Tamas Haraszti (Spatz group, Heidelberg University) for his help in the development of the image processing routine discussed in Sec. 5.7.1.

5.1 Introduction

Sporozoites are elongated and naturally bent cells that, on a flat substrate, move along their longest dimension describing regular, approximately circular trajectories. The current hypothesis is that motility is possible thanks to a conveyer belt system within the parasite, responsible for translocating transmembrane protein complexes from the front to the rear end of the cell [24, 26].

Sporozoite gliding, however, is in general no smooth process and the migration of the parasite can be perturbed, and temporarily impeded, by the formation and rupture of discrete adhesion sites. Recent experiments using reflection interference contrast microscopy have localised the adhesion areas at the front and rear end of gliding sporozoites [27]. These adhesion sites are dynamic: they mature and rupture according to a yet to be understood process. The adhesion site at the rear end is believed to exert the most visible influence on gliding. In fact, it has been reported that the formation of an adhesion site at the rear end of a sporozoite is linked to a pronounced stretching of the cell body, that results in a transient decrease of its curvature. The original shape of the cell is recovered when the

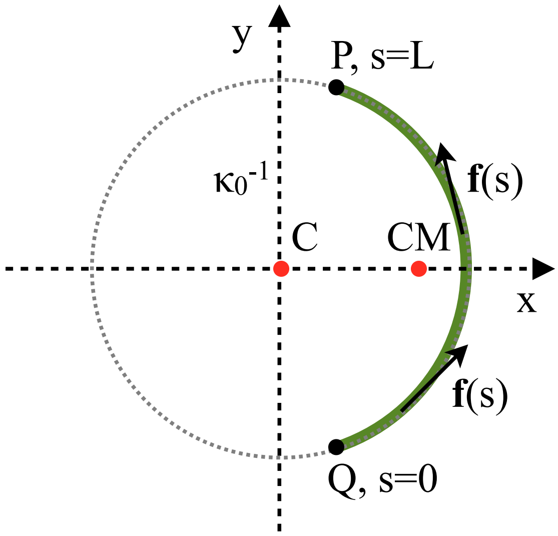

Figure 5.1: A sporozoite is modelled as a one-dimensional bent rod matching a circle of radius κ_0^{-1}. The rod is propelled by a force $\mathbf{f}(s)$ distributed tangentially along its length. The propulsion force results in a net translational force and torque applied at the centre of mass CM.

rear adhesion site ruptures and the parasite can relax. Importantly, this also corresponds to a peak in the speed of the parasite [27].

Motivated by these experimental observations, in this chapter we first present a theoretical model for gliding motility. The model takes into account the peculiar geometry of the parasite and explicitly considers both the conveyer belt and the adhesion sites. In the second part of the chapter, we analyse newly acquired experimental data showing the time dependence of the speed and curvature of Plasmodium *berghei* sporozoites, and draw a connection between the theoretical model and the experimental system.

5.2 Model for a circular glider

We model a sporozoite as a one-dimensional stiff bent rod of length L, with uniform curvature κ_0, so that we can define the angle spanned by the rod as $\alpha = L\kappa_0$. The rod is propelled on a plane by a force per unit length $\mathbf{f}(s)$ that is applied tangentially. There are no a priori constraints on $\mathbf{f}(s)$ (Fig. 5.1).

Let us parametrise the rod in terms of the arc length $s \in [0, L]$, so that the rod is described by the planar curve:

$$\mathbf{r}(s) = \frac{1}{\kappa_0}\begin{pmatrix}\cos\left(\kappa_0\left(s - L/2\right)\right)\\ \sin\left(\kappa_0\left(s - L/2\right)\right)\end{pmatrix}, \tag{5.1}$$

and the generic propulsion force per unit length $\mathbf{f}(s)$ can be written as:

$$\mathbf{f}(s) = f(s) \begin{pmatrix} -\sin\left(\kappa_0\left(s - L/2\right)\right) \\ \\ \cos\left(\kappa_0\left(s - L/2\right)\right) \end{pmatrix} \quad . \tag{5.2}$$

Suppose that $f(s)$ has the following functional form:

$$f(s) = F\delta(s - L) + G\delta(s) + c \ , \tag{5.3}$$

where F and G are point forces localised at the end points of the rod and c is a force density along the rod. Connecting this to the propulsion machinery of a sporozoite, the force density c accounts for a minimal representation of the conveyer belt, while F and G represent the adhesion sites typically observed at the front and rear end of the cell.

The propulsion force $\mathbf{f}(s)$ generates a net translational force $\mathbf{F}_{\mathrm{CM}}$ on the centre of mass of the rod and a torque $\mathbf{T}$ around it, which are calculated as:

$$\mathbf{F}_{\mathrm{CM}} = \int_0^L ds \left[\mathbf{f}(s) \cdot \hat{\mathbf{d}}_{\mathrm{CM,s}}\right] \hat{\mathbf{d}}_{\mathrm{CM,s}} \ , \tag{5.4}$$

$$\mathbf{T} = \int_0^L ds \, \mathbf{d}_{\mathrm{CM,s}} \times \mathbf{f}(s) \ , \tag{5.5}$$

where $\hat{\mathbf{d}}_{\mathrm{CM,s}} = \mathbf{d}_{\mathrm{CM,s}}/|\mathbf{d}_{\mathrm{CM,s}}|$ and $\mathbf{d}_{\mathrm{CM,s}}$ is the vector connecting the centre of mass of the rod to the point on the rod corresponding to the arc-length s:

$$\mathbf{d}_{\mathrm{CM,s}} = \frac{1}{\kappa_0} \begin{pmatrix} \cos(\kappa_0(s - L/2)) - \frac{2}{L\kappa_0}\sin(L\kappa_0/2) \\ \sin(\kappa_0(s - L/2)) \end{pmatrix} \quad . \tag{5.6}$$

5.2.1 Calculation of the torque

We substitute $\mathbf{f}(s)$ and $\hat{\mathbf{d}}_{\mathrm{CM,s}}$ in Eq. (5.5). Since the torque is orthogonal to the plane of the rod we can neglect the vector notation:

$$T = \frac{1}{\kappa_0} \int_0^L ds \, f(s) \left[1 - \frac{2}{L\kappa_0} \sin\left(\frac{L\kappa_0}{2}\right) \cos(\kappa_0(s - L/2))\right] \quad . \tag{5.7}$$

The integration yields:

$$\begin{aligned} T =& \frac{c}{\kappa_0} \int_0^L ds \left[1 - \frac{2}{L\kappa_0} \sin\left(\frac{L\kappa_0}{2}\right) \cos(\kappa_0(s - L/2))\right] + \\ &+ \frac{F+G}{\kappa_0} \left[1 - \frac{2}{L\kappa_0} \sin\left(\frac{L\kappa_0}{2}\right) \cos\left(\frac{L\kappa_0}{2}\right)\right] && (5.8) \\ =& \frac{cL}{\kappa_0} \left[1 - \left(\frac{2}{L\kappa_0}\right)^2 \sin^2\left(\frac{L\kappa_0}{2}\right)\right] + \frac{F+G}{\kappa_0} \left[1 - \frac{1}{L\kappa_0} \sin(L\kappa_0)\right] \quad . && (5.9) \end{aligned}$$

Note that the conveyer belt and the adhesion sites correspond to two independent contributions in the final expression Eq. 5.9.

5.2.2 Calculation of the force

To compute the translational force acting on the centre of mass, it is useful to define a reference frame on the rod, with the y axis pointing in the direction connecting the end points P and Q, and the x axis crossing the rod at $s = L/2$ (Fig. 5.1). Let us consider separately the x and y components of $\mathbf{F}_{\mathrm{CM}} = (F^x_{\mathrm{CM}}, F^y_{\mathrm{CM}})$:

$$\begin{aligned}
F^x_{\mathrm{CM}} =& \int_0^L ds\, \frac{f(s)}{|\mathbf{d}_{\mathrm{CM,s}}|^2}(\hat{f}(s)^x d^x_{\mathrm{CM,s}} + \hat{f}(s)^y d^y_{\mathrm{CM,s}}) d^x_{\mathrm{CM,s}} \qquad (5.10)\\
=& \frac{1}{\kappa_0^2}\frac{2}{L\kappa_0}\sin\left(\frac{L\kappa_0}{2}\right)\int_0^L ds\, \frac{f(s)}{|\mathbf{d}_{\mathrm{CM,s}}|^2}\sin\left(\kappa_0(s-L/2)\right)\\
&\left[\cos\left(\kappa_0(s-L/2)\right) - \frac{2}{L\kappa_0}\sin\left(\frac{L\kappa_0}{2}\right)\right] \quad , \qquad (5.11)\\
F^y_{\mathrm{CM}} =& \int_0^L ds\, \frac{f(s)}{|\mathbf{d}_{\mathrm{CM,s}}|^2}(\hat{f}(s)^x d^x_{\mathrm{CM,s}} + \hat{f}(s)^y d^y_{\mathrm{CM,s}}) d^y_{\mathrm{CM,s}} \qquad (5.12)\\
=& \frac{1}{\kappa_0^2}\frac{2}{L\kappa_0}\sin\left(\frac{L\kappa_0}{2}\right)\int_0^L ds\, \frac{f(s)}{|\mathbf{d}_{\mathrm{CM,s}}|^2}\sin^2\left(\kappa_0(s-L/2)\right) \quad . \qquad (5.13)
\end{aligned}$$

The explicit expression for the distance between the centre of mass of the rod and its point at arc-length s is:

$$|\mathbf{d}_{\mathrm{CM,s}}|^2 = \frac{1}{\kappa_0^2}\left[1 + \left(\frac{2}{L\kappa_0}\right)^2 \sin^2\left(\frac{L\kappa_0}{2}\right) - \frac{4}{L\kappa_0}\sin\left(\frac{L\kappa_0}{2}\right)\cos(\kappa_0(s-L/2))\right] \quad . \tag{5.14}$$

To compute the component F^y_{CM}, denoting $a = L\kappa_0/2$, it is necessary to evaluate the following integral $\jmath$:

$$\begin{aligned}
\jmath =& \frac{1}{\kappa_0}\int_{-a}^{a} dx\, \frac{1-\cos^2 x}{1+\left(\frac{\sin a}{a}\right)^2 - 2\frac{\sin a}{a}\cos x} \qquad (5.15)\\
=& \frac{1}{8\kappa_0}\frac{1}{\sin^2 a}\Big[2a^2 x - 2(2a^2+\cos(2a)-1)\tan^{-1}\left(\frac{(a+\sin a)\tan\left(\frac{x}{2}\right)}{a-\sin a}\right)\\
&+ x\sin^2 a + 4a\sin a\sin x - x\cos^2 a + x\Big]_{-a}^{a} \qquad (5.16)\\
=& \frac{1}{8\kappa_0}\frac{1}{\sin^2 a}\Big[4a^3 - 4(2a^2+\cos(2a)-1)\tan^{-1}\left(\frac{(a+\sin a)\tan\left(\frac{a}{2}\right)}{a-\sin a}\right)\\
&+ 10a\sin^2 a - 2a\cos^2 a + 2a\Big] \quad . \qquad (5.17)
\end{aligned}$$

We can now write explicitly F^x_{CM} and F^y_{CM}:

$$F^x_{\mathrm{CM}} = \frac{1}{\kappa_0^2}\frac{1}{|\mathbf{d}_{\mathrm{CM},0}|^2}(F-G)\frac{2}{L\kappa_0}\sin^2\left(\frac{L\kappa_0}{2}\right)\left[\cos\left(\frac{L\kappa_0}{2}\right)-\frac{2}{L\kappa_0}\sin\left(\frac{L\kappa_0}{2}\right)\right] \quad , \tag{5.18}$$

$$F^y_{\mathrm{CM}} = \frac{1}{\kappa_0^2}\frac{1}{|\mathbf{d}_{\mathrm{CM},0}|^2}(F+G)\frac{2}{L\kappa_0}\sin^3\left(\frac{L\kappa_0}{2}\right)+\frac{2}{L\kappa_0}\sin\left(\frac{L\kappa_0}{2}\right)c\jmath \ . \tag{5.19}$$

Coherently with the symmetry of the system, the component F^x_{CM} is non-zero only when $F \neq G$ and is not influenced by the conveyer belt. On the contrary, F^y_{CM} depends on both the conveyer belt and adhesion sites. However, F^y_{CM} can be separated into a sum of a term only dependent on the sum of the forces at the end points $F + G$ and a term only dependent on the homogeneous force density c.

5.3 Physical assumptions

Now that we have determined analytical expressions for the net force and torque acting on the centre of mass of the rod (Eqs. (5.9), (5.18) and (5.19)), it is appropriate to consider some physical assumptions to better connect the theoretical model with actual sporozoite motility. Because cell migration is a friction dominated process, it is legitimate to assume that inertia effects in sporozoite gliding are negligible [109].

We therefore introduce a translational friction coefficient ξ and a rotational friction coefficient η. Coherently, we define the translational speed of the centre of mass as $v = |\mathbf{F}_{\mathrm{CM}}|/\xi$ and the rotational speed as $\omega = T/\eta$, so that the centre of mass of the rod describes a circular trajectory with radius

$$\rho = \frac{v}{\omega} = \frac{|\mathbf{F}_{\mathrm{CM}}|}{T}\frac{\eta}{\xi} \quad . \tag{5.20}$$

Because sporozoites on a flat substrate describe circular trajectories with a radius determined by the curvature of the cell [22, 27], we require that the radius ρ in Eq. (5.20) coincide with the distance $d_{\mathrm{CM,C}}$ between the centre of mass of the rod and its geometrical centre (Fig. 5.1):

$$d_{\mathrm{CM,C}} = \frac{1}{\kappa_0}\frac{2}{L\kappa_0}\sin\left(\frac{L\kappa_0}{2}\right) \quad , \tag{5.21}$$

$$\frac{\xi}{\eta} = \frac{|\mathbf{F}_{\mathrm{CM}}|}{T}\left[\frac{1}{\kappa_0}\frac{2}{L\kappa_0}\sin\left(\frac{L\kappa_0}{2}\right)\right]^{-1} \quad . \tag{5.22}$$

We study the ratio ξ/η for the case of a rod propelled by the conveyer belt in the absence of adhesion sites ($F = G = 0$ and $c > 0$), a parameter choice that drives the centre of mass on a circular trajectory the centre of which matches the geometrical centre of the rod. Note that for $F = G = 0$ the factor c cancels out in the ratio $|\mathbf{F}_{\mathrm{CM}}|/T$ (Eq. (5.22)), so that there is no dependence on the actual strength of the conveyer belt.

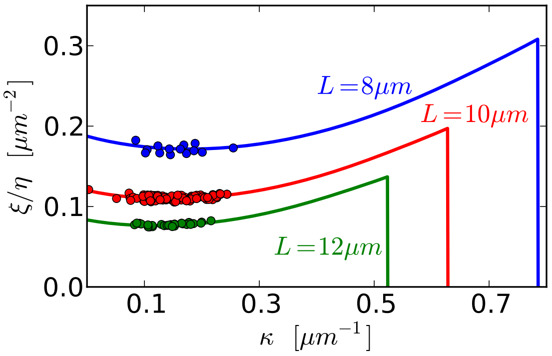

Figure 5.2: The solid lines show the ratio ξ/η for a selection of values of the rod's length L. The curves correspond to $F = G = 0$ and are independent of c. The dots correspond to experimentally measured pairs of sporozoite length and curvature, and are colour-coded based on the measured length. The dots localise around the minima of the curves ξ/η. In the framework of our simple model, this means that sporozoites are more likely to present curvatures corresponding to low translational frictions and high orientational constraints. Data acquired by Lucas Schütz (Frischknecht group).

The solid lines in Fig. 5.2 show the ratio ξ/η for a selection of values of the rod's length L. We terminate the curves at the maximum curvature $2\pi/L$, at which the rod assumes a circular shape. The dots superimposed to the solid lines denote values of ξ/η computed from experimentally measured pairs of sporozoite length and curvature. The dots are colour-coded based on the measured sporozoite length. Curvature and length measurements were performed by Lucas Schütz (Frischknecht group), starting from images of fluorescent Plasmodium *berghei* sporozoites gliding on a flat substrate.

Interestingly, Fig. 5.2 shows that the dots corresponding to the measured length-curvature pairs are distributed around the minimum of the ξ/η curve. In the framework defined by our minimal model, this means that sporozoites are more likely to present curvatures corresponding to low translational frictions and high orientational constraints.

Imposing a condition on the radius of the trajectory of the centre of mass, as in Eq. (5.22), does not represent a constraint on the actual orientation of the bent rod. In order for the centre of the trajectory to coincide with the geometrical centre of the rod, the centre of mass must translate parallel to the line connecting the end points of the rod. In the absence of adhesion sites ($F = G = 0$), as well as in the case of equally strong adhesive forces ($F = G \neq 0$) this condition is verified for any curvature in $[0, 2\pi/L]$. However, with $F \neq G$ the translation of the centre of mass takes place parallel to the end points only in the extreme cases, that is to say curvature 0 (straight rod) or $2\pi/L$ (circular rod).

This simple rationale makes clear that the adhesion sites, that effectively introduce an asymmetry in the propulsion machinery, disturb gliding not only by modifying the speed, but also by perturbing the orientation of the rod. While so far we have dealt with a stiff rod, in the following we introduce the possibility of bending as a response to unequal forces at its end points.

5.4 Asymmetry and deformation

We now relax the condition on the stiffness of the rod and allow for global changes in curvature by introducing a quadratic bending energy as $E_\kappa = h_\kappa(\kappa - \kappa_0)^2$. Denoting with L_{PQ} the distance between the end points of the rod, the force along the line connecting them reads:

$$\frac{dE_\kappa}{dL_{\mathrm{PQ}}} = 2h_\kappa(\kappa - \kappa_0)\frac{d\kappa}{dL_{\mathrm{PQ}}} \quad . \tag{5.23}$$

Knowing that $L_{\mathrm{PQ}} = (2/\kappa)\sin(L\kappa/2)$ we obtain:

$$\frac{d\kappa}{dL_{\mathrm{PQ}}} = \left[-\frac{2}{\kappa^2}\sin\left(\frac{L\kappa}{2}\right) + \frac{L}{\kappa}\cos\left(\frac{L\kappa}{2}\right)\right]^{-1} \quad . \tag{5.24}$$

Under a propulsion force along the rod $\mathbf{f}(s)$ as in Eq. (5.2), we can express the force along the line connecting the end points also as $(F - G)\cos(L\kappa/2)$ because the tangential continuous component c does not deform the rod. It follows that:

$$2h_\kappa\frac{\kappa - \kappa_0}{F - G} = -\frac{1}{\kappa^2}\sin(L\kappa) + \frac{L}{\kappa}\cos^2\left(\frac{L\kappa}{2}\right) \quad . \tag{5.25}$$

If it exists, the solution to this equation κ^* gives the equilibrium curvature of the rod.

To better study Eq. (5.25), it is convenient to define a typical length-scale κ_0^{-1} and a typical force scale $h_\kappa\kappa_0^3$. We write $G = F + \Delta F$ and observe that the integral $\jmath$ has dimension of length, while c is a force per unit length. In its non-dimensional form, Eq. (5.25) reads:

$$2\frac{1 - \widetilde{\kappa}}{\Delta\widetilde{F}} = -\frac{1}{\widetilde{\kappa}^2}\sin(\widetilde{L}\widetilde{\kappa}) + \frac{\widetilde{L}}{\widetilde{\kappa}}\cos^2\left(\frac{\widetilde{L}\widetilde{\kappa}}{2}\right) \quad , \tag{5.26}$$

with $\widetilde{\kappa} = 1$ corresponding to $\kappa = \kappa_0$ of the dimensional case. Equation (5.26) can be interpreted graphically with the help of Fig. 5.3a, in which the left hand side of Eq. (5.26) is represented in green, and the right hand side in blue. For $\Delta\widetilde{F} = 0$, corresponding to the case of symmetric propulsion along the rod, the left hand side of Eq. (5.26) is a vertical line that intersects the right hand side in $\widetilde{\kappa}^* = 1$. For a rod with length $\widetilde{L}$ such that $\pi/\widetilde{L} > 1$, increasingly negative values of $\Delta\widetilde{F}$ cause a decrease in the curvature, that tends to zero for an infinitely negative $\Delta\widetilde{F}$. On the contrary, positive values of $\Delta\widetilde{F}$ lead to an increase in curvature, that is limited by the maximum value $\pi/\widetilde{L}$.

For rods with length such that $\pi/\widetilde{L} < 1$ the behaviour is the opposite, so that the rod tends to close to a circle for a negative ΔF, while it straightens towards π/L for a positive ΔF. However, in our model of sporozoite gliding, this second case is not relevant, because, to our knowledge, sporozoites spanning an angle greater than π have not been observed so far. Figure 5.3b shows a scatter plot of values of sporozoite length and curvature (blue

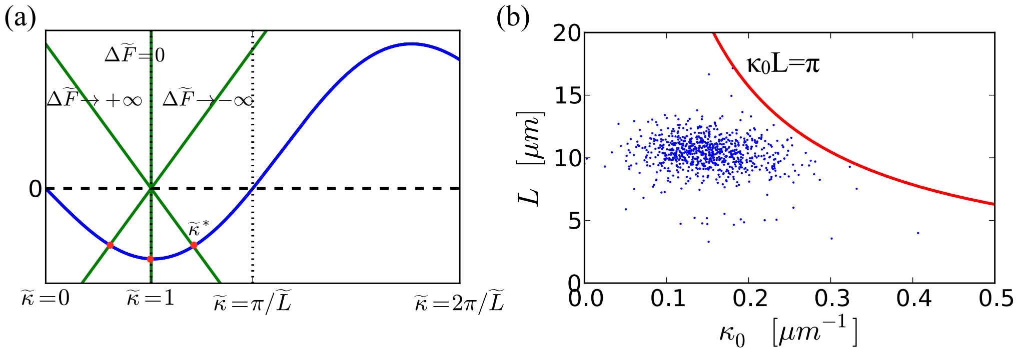

Figure 5.3: (a) Graphical solution of Eq. (5.26). The left hand side is in green, the right hand side in blue. For $\pi/\widetilde{L} > 1$ the solution $\widetilde{\kappa}^* \in [0, \pi/\widetilde{L}]$. For $\Delta\widetilde{F} > 0$ $\widetilde{\kappa}^* < 1$, corresponding to a stretched rod. (b) Scatter plot of N=895 experimentally measured pairs of sporozoite curvature and length (κ_0, L) (blue dots). The comparison with the red solid line ($\kappa_0 L = \pi$) reveals that there are no sporozoites spanning an angle larger than π. Data acquired by Lucas Schütz (Frischknecht group).

dots); the solid red line corresponds to $L\kappa_0 = \pi$. Note that all the measured (L, κ_0) pairs lie below this line (measurements by Lucas Schütz, Frischknecht group).

In the light of these observations, we limit our analysis to the case of moderately curved rods ($L\kappa_0 < \pi$). Connecting the model to sporozoite gliding, negative values of ΔF correspond to the rear adhesion site impeding the translocation of the cell and/or to the front part of the cell moving forward at an increased speed. Positive values of ΔF, instead, correspond to the rear pushing the cell forward and/or the front adhesion site impeding the translocation.

According to our model, any ΔF causes a change in the equilibrium curvature κ^* of the sporozoite. Whether the curvature increases or decreases depends on the relative strength of the adhesion sites and on the rest configuration of the sporozoite. Importantly, the angle $L\kappa_0$ spanned by the cell in its rest configuration is predicted to determine the maximum and minimum curvatures that can be assumed.

5.5 Adhesion dynamics

In this section we connect the deformation of the rod with the dynamics of adhesion. We set $F = 0$, thus limiting our study to the dynamics of the adhesion site at the rear end of the rod. This choice is motivated by the fact that the role of a sporozoite's rear adhesion site is more apparent than that of the front one. Indeed, the formation of a rear adhesion site has been linked experimentally to a decrease in the curvature of the sporozoite because of stretching [27].

As done in Eq. (5.26), in the following lengths are measured in units of κ_0^{-1} and forces in units of $h_\kappa \kappa_0^3$. In order not to clutter the expressions with symbols, in the text and

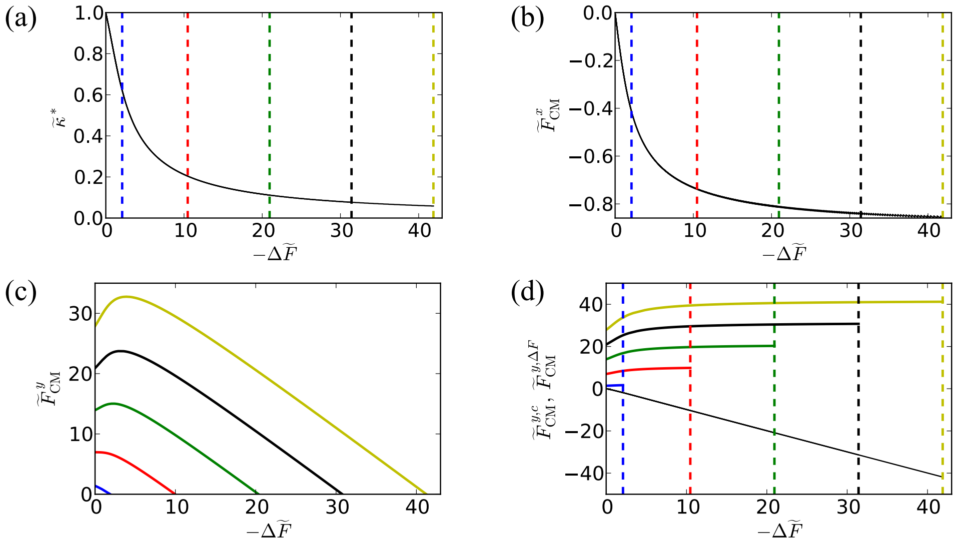

Figure 5.4: Dependence on the stretching force $\Delta\widetilde{F}$. (a) The equilibrium curvature $\widetilde{\kappa}^*$ decreases with increasing stretching down to $\widetilde{\kappa}^*(\widetilde{L}\widetilde{c})$, where $\widetilde{L}\widetilde{c}$ is the maximum stretching allowed. (b) Growing stretching generates a force $\widetilde{F}^x_{\mathrm{CM}}$. The growth of its magnitude slows with increasing stretching. (c) The force $\widetilde{F}^y_{\mathrm{CM}}$ develops a maximum at finite stretching for sufficiently high values of $\widetilde{c}$. (d) The maximum in $\widetilde{F}^y_{\mathrm{CM}}$ stems from the competition between $\widetilde{F}^{y,c}_{\mathrm{CM}}$ (thin black) and $\widetilde{F}^{y,\Delta F}_{\mathrm{CM}}$ (solid lines in colour). A higher $\widetilde{c}$ leads to steeper $\widetilde{F}^{y,c}_{\mathrm{CM}}$ and therefore to the maximum observed in (c). The blue, red, green, black and yellow line denote, respectively, $\widetilde{c} = 1, 5, 10, 15, 20$.

equations we drop the tilde notation, that is no longer necessary because from now on all quantities are intended in their non-dimensional form. Nevertheless, we maintain the tilde notation in the figures, in order to ease the comparison between dimensional and non-dimensional plots.

For clarity, we rewrite here explicitly the components of the force on the centre of mass and the equation determining the equilibrium curvature of the rod in their non-dimensional form. For $F = 0$ the equations for the equilibrium curvature and the force on the centre of mass read:

$$2\frac{1-\kappa}{\Delta F} = -\frac{1}{\kappa^2}\sin(L\kappa) + \frac{L}{\kappa}\cos^2\left(\frac{L\kappa}{2}\right) \quad , \tag{5.27}$$

$$F^x_{\mathrm{CM}} = -\Delta F \frac{1}{\kappa^2}\frac{1}{|\mathbf{d}_{\mathrm{CM},0}|^2}\frac{2}{L\kappa}\sin^2\left(\frac{L\kappa}{2}\right)\left[\cos\left(\frac{L\kappa}{2}\right) - \frac{2}{L\kappa}\sin\left(\frac{L\kappa}{2}\right)\right] \quad , \tag{5.28}$$

$$F^y_{\mathrm{CM}} = \frac{1}{\kappa^2}\frac{1}{|\mathbf{d}_{\mathrm{CM},0}|^2}\Delta F \frac{2}{L\kappa}\sin^3\left(\frac{L\kappa}{2}\right) + \frac{2}{L\kappa}\sin\left(\frac{L\kappa}{2}\right) c\jmath \ . \tag{5.29}$$

Note that only F^y_{CM} is influenced by the conveyer belt parameter c. The equilibrium curvature κ^* and the component F^x_{CM} depend solely on the stretching force ΔF.

We fix the length of the rod at $L = 2\pi/3$, consistently with the angle spanned by a typical sporozoite (Fig. 5.3b). Figure 5.4 shows the dependence of curvature and force on ΔF for different values of the conveyer belt parameter c. Here, and throughout the rest of this chapter, the blue, red, green, black and yellow line denote, respectively, $c = 1, 5, 10, 15, 20$. For each c, we consider negative values of $\Delta F \in [-Lc, 0]$, an interval consistent with the facts that Lc is the maximum possible force exerted on the centre of mass by the conveyer belt, and that the rod is not allowed to reverse its direction of motion. In order to ease visualisation we plot $-\Delta F$ on the x axis.

Figure 5.4a and 5.4b show the equilibrium curvature and the component F^x_{CM} for growing stretching. As expected, the rod straightens and its curvature κ^* tends to zero. A non-zero component F^x_{CM} builds up with increasing stretching. However, as the rod stretches, $|F^x_{\text{CM}}|$ grows more slowly, a fact that points towards its limited influence on the magnitude of the total force on the centre of mass F_{CM}. As already mentioned, κ^* and F^x_{CM} depend on the conveyer belt only via the maximum possible stretching. The maximum stretching values Lc are represented by the vertical dashed lines, colour-coded according to the strength of the conveyer belt.

Figure 5.4c represents the component F^y_{CM}, namely the component of the propulsion force in the direction connecting the end points of the rod. Interestingly, for increasing conveyer belt strengths c, the propulsion force in the y direction shows a maximum at finite stretching values.

The reason for that is the competition between the buildup of ΔF and the conveyer belt system. Let us separate F^y_{CM} into a term only dependent on ΔF and a term only dependent on c: $F^y_{\text{CM}} = F^{y,\Delta F}_{\text{CM}} + F^{y,c}_{\text{CM}}$ (Eq. (5.29)). The term $F^{y,\Delta F}_{\text{CM}}$ is shown in Fig. 5.4d as the thin black line, while $F^{y,c}_{\text{CM}}$ is shown in colour for the same values of c defined above and colour-coded accordingly. The conveyer belt term $F^{y,c}_{\text{CM}}$ increases monotonously with increasing stretching, but cannot exceed Lc. On the other hand, $F^{y,\Delta F}_{\text{CM}}$ decreases monotonously with increasing stretching. The appearance of the maximum in F^y_{CM} depends on the gradient of $F^{y,c}_{\text{CM}}$ at small stretching values: if c is high enough for $F^{y,c}_{\text{CM}}$ to be steeper than $-F^{y,\Delta F}_{\text{CM}}$, then a maximum appears, otherwise F^y_{CM} is monotonously decreasing with growing stretching.

In the following we take a step further and introduce a temporal dependence in ΔF. We aim at modelling a plausible temporal dynamics of the formation and rupture of the adhesion sites at the rear end of a sporozoite. We study the relation between $\Delta F(t)$, $\kappa^*(t)$ and the magnitude $F_{\text{CM}}(t)$ of the force acting on the centre of mass. Because in our system inertia effects are negligible, F_{CM} is representative of the speed of the centre of mass of the rod. We have checked that F^x_{CM} only has a very limited influence on F_{CM}, so that to a first approximation $F_{\text{CM}} \simeq F^y_{\text{CM}}$.

Note that we are working under the simplifying assumption that, as a response to ΔF, the rod assumes the curvature κ^* corresponding to mechanical equilibrium. This amounts to separating the timescale of adhesion formation and rupture from the timescale of deformation.

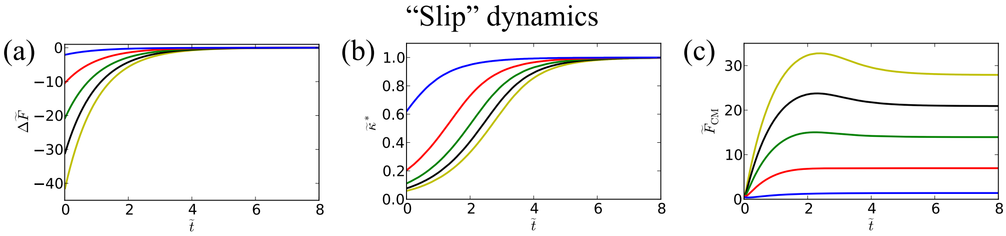

Figure 5.5: (a) Relaxation of the stretching force $\Delta\widetilde{F}$ based on Eq. (5.30) for various values of $\widetilde{c}$. (b) The equilibrium curvature follows the relaxation of $\Delta\widetilde{F}$ according to a non-linear, $\widetilde{c}$-dependent relation. (c) The magnitude of the force on the centre of mass develops a maximum at finite time, i.e. finite stretching, with increasing $\widetilde{c}$. The blue, red, green, black and yellow line denote, respectively, $\widetilde{c} = 1, 5, 10, 15, 20$.

5.5.1 Slip

Consider a rod propelled by a conveyer belt of strength c and with a mature adhesion site at the rear end. The adhesion site impedes migration and the rod is subject to a stretching force $\Delta F_0 < 0$ and has the corresponding curvature $\kappa^*(\Delta F_0) < 1$.

Suppose that the adhesion site suddenly ruptures at time $t_0 = 0$ and, as a consequence, the stretching decreases exponentially with a typical timescale τ_{deg}:

$$\Delta F(t) = \Delta F_0 e^{-t} \quad , \tag{5.30}$$

where t is measured in units of τ_{deg}.

The time dependences of ΔF, κ^* and F_{CM} are represented in Fig. 5.5 for different values of the non-dimensional strength of the conveyer belt c. The blue, red, green, black and yellow lines correspond, respectively, to $c = 1, 5, 10, 15, 20$.

We have set $\Delta F_0 = -Lc$, based on the facts that Lc is the maximum possible force exerted on the centre of mass by the conveyer belt and that the rod is not allowed to reverse its direction of motion. A comparison of Figs. 5.5a and 5.5b shows that the curvature relaxes monotonously to $\kappa^* = 1$ following the evolution of ΔF. Figure 5.5c highlights the effect of the conveyer belt on F_{CM}. Coherently with the time independent case we have studied at the beginning of this section (Fig. 5.4), higher values of c lead to the emergence of a maximum in the force, and consequently to a speed peak during slipping.

5.5.2 Stick

Consider a rod under perfect gliding conditions, meaning $F = G = 0$ and $c > 0$, so that it has constant unit curvature. Suppose that at time $t_0 = 0$ an adhesion site starts developing at the rear end, so that the rod is subject to a stretching force of increasing magnitude.

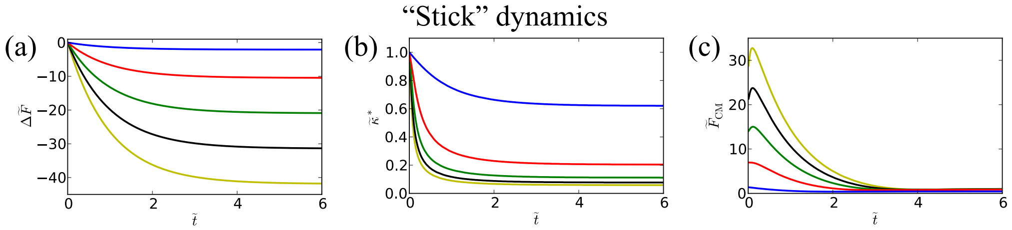

Figure 5.6: (a) Buildup of the stretching force $\Delta\widetilde{F}$ based on Eq. (5.31) for various values of $\widetilde{c}$. (b) The equilibrium curvature decreases following the variation of $\Delta\widetilde{F}$ according to a non-linear, $\widetilde{c}$-dependent relation. (c) The magnitude of the force on the centre of mass develops a maximum at finite time, i.e. finite stretching, with increasing $\widetilde{c}$. The blue, red, green, black and yellow line denote, respectively, $\widetilde{c} = 1, 5, 10, 15, 20$.

Let us describe the buildup of the stretching force as:

$$\Delta F(t) = \Delta F_{\mathrm{min}}(1 - e^{-t}) \ , \tag{5.31}$$

where the time t is measured in units of τ_{adh}, the typical timescale of maturation for the adhesion site. We set $\Delta F_{\mathrm{min}} = -Lc$ and represent the time dependences of ΔF, κ^* and F_{CM} in Fig. 5.6 for different values of the non-dimensional strength of the conveyer belt c.

A comparison of Figs. 5.6a and 5.6b shows that the curvature decreases as stretching becomes more pronounced. Because our choice of F_{min} depends on c, a stronger conveyer belt supports stronger adhesion sites and therefore leads to more pronounced deformations of the rod.

Let us consider the maximum in F_{CM} that appears at sufficiently high values of c (Fig. 5.6c). This maximum has the same origin as the one observed in the slip dynamics (Fig. 5.5c), i.e. it stems from the dependence of F^y_{CM} on ΔF (Fig. 5.4c).

However, there are relevant differences between the two cases. In the slip case the maximum appears after about $2\tau_{\mathrm{deg}}$ and corresponds to a peak significantly broader than the timescale at which stretching degrades. This can be seen in Fig. 5.5c, in which time is measured in units of τ_{deg}.

On the contrary, in the stick case, the maximum appears significantly before τ_{adh} and the peak is narrower. This can be seen in Fig. 5.5c, in which time is measured in units of τ_{adh}.

To interpret these differences, let us compare Figs. 5.5b with 5.6b. During sticking, the curvature reacts with a timescale shorter than that of adhesion maturation. During slipping, the curvature reacts more slowly than the timescale of adhesion depletion. The cause of this difference lies in the non-linear dependence of κ^* on ΔF (Fig. 5.4a). To prove that, consider, without loss of generality, $\tau_{\mathrm{adh}} = \tau_{\mathrm{deg}} = 1$. Based on the definitions in

Eq. (5.30) and Eq. (5.31), with $\Delta F_0 = \Delta F_{\mathrm{min}} = -Lc$ we can write:

$$\Delta F(t)_{\mathrm{stick}} = \Delta F_0 - \Delta F(t)_{\mathrm{slip}} \ . \tag{5.32}$$

If the time dependences of curvature increase and decrease would follow symmetric trends, then it would hold:

$$\kappa^*(t)_{\mathrm{stick}} = 1 - \kappa^*(t)_{\mathrm{slip}} \tag{5.33}$$

$$\Rightarrow \ \ \kappa^*(\Delta F(t)_{\mathrm{stick}}) = 1 - \kappa^*(\Delta F(t)_{\mathrm{slip}}) \tag{5.34}$$

$$\Rightarrow \ \ \kappa^*(\Delta F_0 - \Delta F(t)_{\mathrm{slip}}) = 1 - \kappa^*(\Delta F(t)_{\mathrm{slip}}) \ . \tag{5.35}$$

The last equation would be satisfied only if κ^* were a linear function of the stretching ΔF. Instead, κ^* depends non-linearly on ΔF, and stick and slip lead to different behaviours in the curvature. As we will see in the following, this is consistent with experimental measurements of sporozoite speed and curvature.

5.6 Model: summary and implications

To summarise, in this minimal theoretical model for gliding we have taken into account three key features that characterise sporozoite migration on flat substrates, namely the curvature of the cell, its bending stiffness and its gliding machinery. In particular, we have based our description of the gliding machinery on the current experimental knowledge, that points in the direction of a conveyer belt responsible for propulsion along the cell body. Adhesion sites at the front and rear end of the cell are believed to influence the gliding motility and, in particular, the adhesion site at the rear end has already been linked experimentally to deformations in the cell body, because its presence induces stretching [27].

Approximating a sporozoite as a bent rod, we have linked the buildup of an adhesion site at the rear end with changes in the curvature of the rod. Importantly, we have identified the strength of the conveyer belt as a key player in determining the force acting on the centre of mass of the rod at various levels of stretching. In fact, a sufficiently strong conveyer belt causes such force to peak at finite stretching values.

Finally, we have postulated two simple time dependences for the stretching force ΔF for stick and slip events separately. In both cases, the force on the centre of mass shows a maximum depending on the strength of the conveyer belt. However, the features of this maximum, such as its location and the width of the corresponding peak, are different. We have proven that such differences stem from the non-linear relation between the equilibrium curvature and ΔF.

In conclusion, even with very simple structural assumptions and an elementary temporal dynamics for the stretching force, the behaviour of a sticking and slipping rod is not trivial.

Non-linearity, that is inherent in our system due to the curvature of sporozoites, causes the rod to behave differently during sticking and slipping events. This gives a first effective measure of the complexity associated to sporozoite gliding.

Finally, from our model we deduce that the presence of the conveyer belt is necessary to observe a speed peak during a slip event. Our model also predicts that the height of this peak be the same irrespective of how much the rod is stretched when the rear adhesion site starts degrading. This prediction may turn out to be inaccurate because of our simplifying assumptions, like the independence of the conveyer belt strength on time or stretching status.

We also predict that a peak in speed could be observed during stretching. While this prediction is grounded in basic features of the model, its observation may be challenging. One reason for that is the predicted narrowness of the peak, another that c may not be constant during stretching.

Another factor to take into account during stretching is that a sporozoite is likely to react to the buildup of stretching with a certain temporal delay τ. In other words, a refinement of our model would be to consider $\kappa^*(t) = \kappa^*(\Delta F(t-\tau))$. In addition to taking into account the time dependence of the conveyer belt and possible delays in the deformation, further refinements of the model could stem from the introduction of noise terms and stochasticity in the formation and depletion of the adhesion sites. In general, the model would greatly benefit from targeted experimental investigations, for instance focusing on the temporal dynamics of adhesion formation and depletion.

In the remaining part of this chapter, we analyse experimental time series of speed and curvature of Plasmodium *berghei* sporozoites. We highlight, whenever possible, the connections between our minimal theoretical model and the results of the analysis.

5.7 Analysis of the speed and curvature of sporozoites

5.7.1 Data and first processing

To investigate the relationship between the speed and curvature of sporozoites, we consider movies of fluorescent GFP-expressing Plasmodium *berghei* sporozoites gliding on a flat surface. The movies were recorded using a spinning disc microscope at 10 frames per second (fps) for a total time of 120 s by Konrad Beyer (Frischknecht group). From the movies we are able to isolate 8 sporozoites, characterised by stable gliding and an ideal image quality throughout the recording time. An example is represented in Fig. 5.7a.

For each frame of the movie, we apply to each of the selected sporozoites a simple image processing routine to determine its centroid and average curvature. The routine, adapted from a preliminary version kindly provided by Tamas Haraszti (Spatz group, Heidelberg University), performs the following steps:

- corrects the background, smoothes the image and then thresholds it, in order to

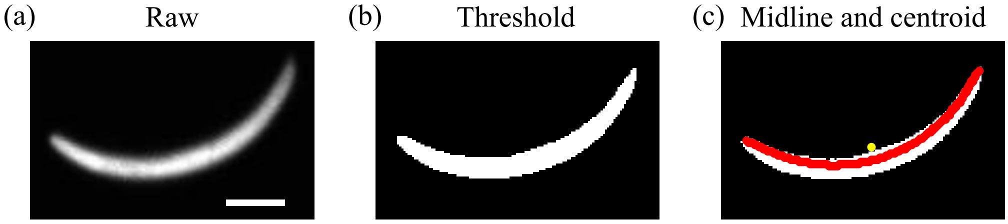

Figure 5.7: (a) Raw image of a fluorescent GFP-expressing sporozoite gliding on a flat surface (Konrad Beyer, Frischknecht group) (b) Thresholding after background correction and smoothing. (c) The thresholded sporozoite with its midline (red) and centroid (yellow). The midline results from an active contour algorithm [110].

isolate the sporozoite (Fig. 5.7b);

- computes the centroid of the thresholded sporozoite (yellow dot in Fig. 5.7c).
- applies an active contour algorithm that detects the midline of the sporozoite (red line in Fig. 5.7c) [110];
- evaluates the mean curvature of the sporozoite using the midline.

We determine the mean curvature of a sporozoite by considering the end points of the midline together with each point in between. For each set of three points we compute the radius of the circumscribed circle, then invert the average of the radii thus computed to obtain the mean sporozoite curvature.

From the information on the position of the centroid we extract the speed of the sporozoite, thus obtaining the time dependent speed and curvature of each sporozoite.

Speed and curvature signals, normalised to zero mean and unit variance for better comparison, are represented in Fig. 5.8 for two sample sporozoites. In particular, Fig. 5.8a shows the signals of a neatly gliding sporozoite, for which stick-slip events are clearly distinguishable and co-localised with pronounced changes in curvature (see Figs. 5.8a(i) and (ii)). On the other hand, Fig. 5.8b represents a more complex case, in which changes in curvature can be detected but the speed of the centre of mass is oscillating more noisily.

Speed peaks, that characterise slip events and are associated to a net forward movement of the parasite [27], reveal that the parasite is propelled forward during slipping. Indeed, because of the overdamped nature of the system, in the absence of propulsion forward displacement would not be observed. This argument supports the presence of a conveyer belt propulsion system competing with the adhesion sites.

5.7.2 Wavelet analysis

The gliding motility of sporozoites on a flat surface is characterised by irregular changes in speed and curvature and, because of that, it is referred to as stick-slip motility [27]. Figure

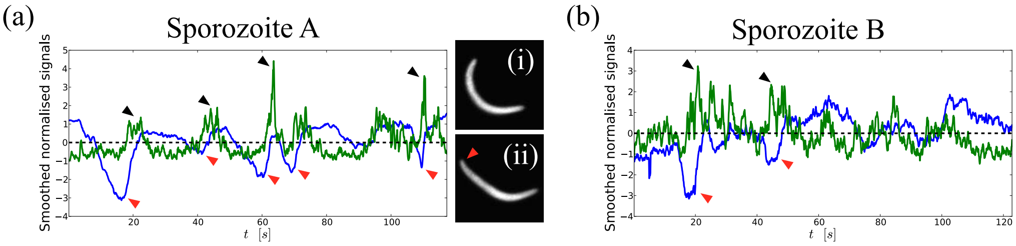

Figure 5.8: Normalised speed (green) and curvature (blue) for two sporozoites. Red arrowheads point to low curvatures, corresponding to stick events. Black arrowheads point to speed peaks, corresponding to slip events. (a) Sporozoite A shows frequent and neat stick-slip events, matched by clear deformations in the cell body; (i) and (ii) show the sporozoite respectively undeformed and stretched (Konrad Beyer, Frischknecht group). The red arrowhead in (ii) locates the sticking rear end of the cell. (b) Sporozoite B is more complex and shows a less regular dynamics with two clear stick-slip events.

5.8 shows that speed peaks co-localise with regions of low curvature, strongly suggesting that the two features are related to each other.

The presence of speed peaks and abrupt curvature changes implies that we are dealing with non-stationary signals. The statistical properties of the signal, like mean and standard deviation, in general depend on the time point at which they are computed. As a consequence, the signal analysis must take into account the temporal information. This first observation already excludes the Fourier transform as a viable analysis tool. The Fourier power spectrum, in fact, only informs about the frequencies that, on average, dominate the signal, without providing any directly interpretable information concerning when which frequencies are actually dominating. In addition, the spectrum resulting from Fourier analysis is strongly affected by border effects due to the finite length of the signals.

Borrowing an effective metaphor from [111], we can imagine the Fourier spectrum as the average note of a melody, which is clearly an inaccurate summary of the music itself. We need instead a technique able to formally describe the music while preserving the temporal information written on the pentagram. An appropriate tool for that is the wavelet transform [111, 112], that allows to decompose the signal in both time and frequency, thereby providing an outcome analogous to a time dependent power spectrum.

5.7.3 Preliminary information

In order to guarantee the clarity of the results presented in the next section, here we report a few necessary definitions, redirecting the reader to [112] and references therein for further details.

A *wavelet function* $\psi(\eta)$ is a function with zero mean, localised in both time and frequency space. The function depends on a non-dimensional parameter η, that, for our purposes, we can think of as a temporal parameter. The wavelet we are working with is the real Morlet wavelet, consisting of a cosine wave wrapped by a Gaussian (Fig. 5.9). The

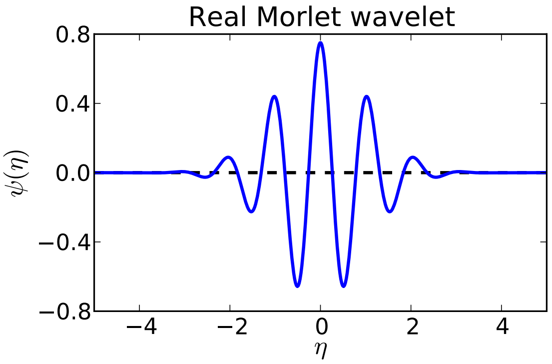

Figure 5.9: Real Morlet wavelet (Eq. (5.36)) with $\omega_0 = 5$. The purpose of wavelets is to filter signals locally to determine which scales dominate which regions, providing as an output the equivalent of a time dependent power spectrum.

real Morlet wavelet is expressed as:

$$\psi(\eta) = C\pi^{-\frac{1}{4}} e^{-\frac{\eta^2}{2}} \cos(\omega_0 \eta) \ , \tag{5.36}$$

where C is a normalisation factor.

Given a discrete sequence x_n, its *continuous wavelet transform* is defined as:

$$W_n(s) = \sum_{n'=0}^{N-1} x_{n'} \psi^* \left[\frac{(n'-n)\delta t}{s} \right] \ . \tag{5.37}$$

Effectively, $W_n(s)$ is a convolution of the sequence x_n with the wavelet ψ conjugated, translated by n and scaled by s. The parameter n identifies the time point under study in the signal, while s measures the width of the wavelet and, consequently, the amplitude of the interval centred in n that contributes to the coefficient $W_n(s)$. The combined presence of the rescaling and the translation provides a 2D output that allows to localise the dominant scales s as a function of time n. Scales s can be related to corresponding Fourier periods via wavelet dependent relations. Because wavelets are localised functions, from them one can only derive approximate periods, known as *pseudo-periods*.

For a signal X, the *wavelet power spectrum* is defined as $|W_n(s)|^2$. For two signals X and Y, the *cross wavelet power spectrum* $|W_n(s)^X W_n(s)^Y|$ quantifies the covariance between the two sequences. It is also possible to define the *global wavelet power spectrum* as the average of the power spectrum over n, thereby obtaining information about the dominant scales, but loosing the information about when such dominance actually occurs in the signal. The global wavelet spectrum has been shown to provide a reliable estimate of the true power spectrum of a time series [113].

In the case of signals of finite length, border effects must be accounted for. The localisation of the wavelet function guarantees that border effects due to the finiteness of the signal are reduced in comparison to the Fourier case. Border effects in wavelet analysis are quantified by the *cone of influence* (COI): given a wavelet power spectrum, the COI identifies the regions for which edge effects are important. The COI is wavelet dependent and is related to the decay of the autocorrelation of the wavelet power at each scale.

Finally, we need a tool to determine the significance of the power spectrum, i.e. how much the power spectrum of the signal rises above the power spectrum associated to the noise in the signal itself. In order to do that, one needs to assume an appropriate background spectrum. Because sporozoites are propelled by a complex molecular machinery, it is appropriate to assume the presence of autocorrelated background noise in both the speed and curvature signals. As proposed in [112], we assume red noise as a background and compute the background power spectrum as outlined in section 4 of that paper. We point out that, although this is a reasonable and common assumption, future work should address also the determination of the optimal background to perform the signal analysis with.

In the following we carry out a wavelet analysis for the speed and curvature signals using the MATLAB Wavelet Toolbox. As already mentioned, we use a real Morlet wavelet (MATLAB's 'morl') and analyse the spectra of speed and curvature separately, but also their cross spectrum to visualise a possible relation between the signals. In computing average quantities, we exclude the coefficients belonging to the cone of influence, because they are influenced by edge effects.

5.7.4 Results

In this section we present the results of the wavelet analysis for the two representative sporozoites, among the 8 available, already mentioned in the context of Fig. 5.8.

We point out that a wavelet analysis has already been proposed in [27] for time series of sporozoite speeds, focusing on the global wavelet spectrum. There are two important differences between that first study and our case, of which the first one concerns the sampling frequency. In [27] data are acquired at 2 frames per second (fps), while our 10 fps allow for greater precision in the study of the stick-slip events. The second, and more important, difference is that we have simultaneous measurements of both sporozoite speed and curvature. This allows for a first, insightful study of the quantitative relation between sporozoite migration and the deformations of the cell body.

In order to ease the visual interpretation of the two-dimensional wavelet power spectra, let us consider two elementary examples, namely a harmonic wave $\cos(t)$ and a smooth step function $(1 + e^{(t-t_0)/dt})^{-1}$. Figure 5.10 shows the power spectra with the temporal coordinate on the x axis and the pseudo-periods on the y axis.

The harmonic wave (Fig. 5.10a) appears as a sequence of regularly spaced areas of high power, with the power peaks localised at the wave period 2π. There exist a restricted interval of scales for which wavelets are a good match to the signal. Because the power spectrum consists of the wavelet coefficients squared, peaks in intensity are spaced by half the wave period. The emergence of a typical period is analogous to the case of the Fourier

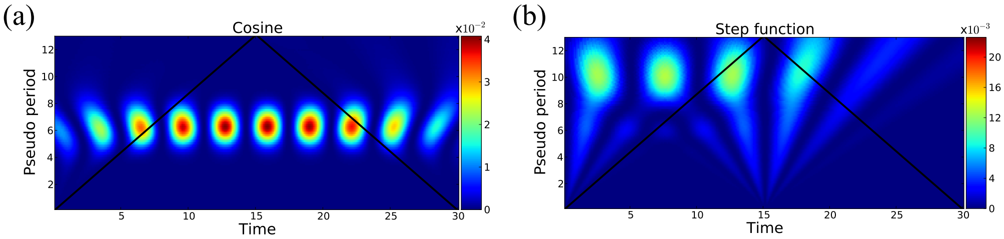

Figure 5.10: Example of wavelet power spectra for two representative functions. (a) The spectrum of $\cos(t)$ consists of a sequence of regularly spaced areas of high power, with power peaks localised at the period 2π. (b) The smooth step function $(1+e^{(t-t_0)/dt})^{-1}$, with $dt = 10^{-4}$ and $t_0 = 15$ shows a power spectrum consisting of regions of high power radiating from t_0. The upper left and right corners of the spectra belong to the cone of influence (black line) and are not significant because of edge effects.

spectrum, that spikes at the defining frequency of a harmonic function. The step function, in contrast, produces a wavelet power spectrum characterised by regions of high power radiating from t_0 ($t_0 = 15$ in Fig. 5.10b). Again, the situation is coherent with the Fourier case, which requires an infinite range of frequencies to describe a step function.

The COI is delimited by the black solid lines in Fig. 5.10: the upper left and right corners of the spectra suffer from edge effects. The coefficients $W_n(s)$ in these areas are not taken into account for the analysis of the power spectra.

Let us now turn our attention to the analysis of the speed signal in Fig. 5.11. Figure 5.11a(i) shows the speed signal after smoothing via a sliding average, while Fig. 5.11a(ii) represents the corresponding wavelet power spectrum. From that we recognise patterns corresponding to regularly spaced power peaks at two or more preferred scales, or pseudo-periods τ. We identify two dominant periods of approximately $\tau_1 \simeq 25s$ and $\tau_2 \simeq 10s$. We recognise in τ_1 the typical time interval between two speed peaks in Fig. 5.11a(i). The co-localisation between regions of low curvature and speed peaks (Fig. 5.8) implies that τ_1 also sets the timescale of deformations of the cell body.

The period τ_2 suggests instead the presence of less powerful, more frequent peaks in the speed, that could be linked to the molecular propulsion machinery of the cell. We speculate that the molecular propulsion machinery could function at a characteristic timescale τ_1 and that τ_2 represents the typical period of an adhesion cycle. To a first approximation, we can imagine the dynamics of the propulsion machinery and that of the adhesion sites to be independent of each other, thus recovering the framework of the theoretical model presented in the first part of this chapter.

By observing the spectrum of the curvature signal in Fig. 5.11b(ii), we see regions of higher power localised at pseudo-periods compatible with τ_1, while we do not identify peaks in power corresponding to τ_2. This indeed suggests that not all the speed dynamics is responsible for deformations of the sporozoite, but these rather stem from the speed dynamics associated with the longer timescale, that we interpret as the timescale of adhesion.

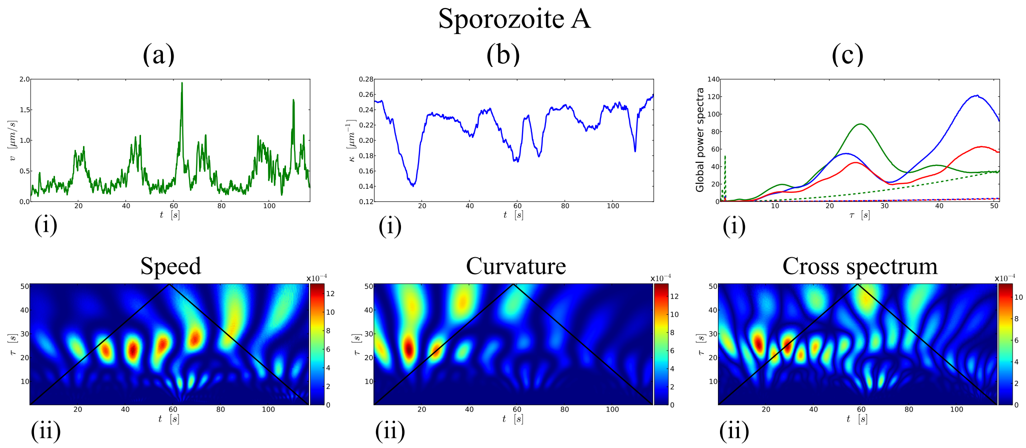

Figure 5.11: (a) (i) Speed of the sporozoite after smoothing via a sliding average. (ii) Wavelet spectrum of the speed. There are two characteristic periods: $\tau_1 \sim 25s$, associated to the stick-slip events, and $\tau_1 \sim 10s$, possibly related to the molecular propulsion machinery. (b) (i) Curvature of the sporozoite after smoothing via a sliding average. (ii) Wavelet spectrum of the curvature. There are power peaks around τ_1, matching the speed spectrum. In the curvature spectrum τ_2 is not present, suggesting that not all the speed dynamics translates into shape changes. (c) (i) Global power spectra corresponding to speed (green), curvature (blue) and cross spectrum (red). All share a peak around $\tau \sim 25s$, while at $\tau \sim 10s$ one can see the secondary speed peak not matched by a local maximum in the curvature. (ii) Cross wavelet spectrum: the covariance between speed and curvature is particularly meaningful around τ_1.

The cross wavelet spectrum in Fig. 5.11c(ii) shows neatly the covariance between speed and curvature, particularly intense around τ_1. The cross wavelet spectrum, however, is not a particularly intuitive tool, mostly because it is influenced by both the features of the single spectra and their mutual relationship.

In Fig. 5.11c(i) we show the global spectra corresponding to speed, curvature and cross wavelet spectrum (respectively the green, blue and red solid lines). The dashed lines, with an analogous colour-coding, denote the 95% confidence level, evaluated based on a red noise spectrum [112]. After discussing in detail the two-dimensional wavelet spectra, it is clear how the global power spectrum provides information of only limited quality. By averaging over time it is no longer possible to recognise the temporal dynamics of the areas of higher power. This is not particularly evident in the case of Fig. 5.11, for which τ_1 and τ_2 are rather stable over time. However, the situation is more apparent in Fig. 5.12, in which the dominant periods depend on time. From the two-dimensional spectrum of the speed (Fig. 5.12a(ii)) we can locate area of higher power at different pseudo-periods. The two-dimensional spectrum of the curvature (Fig. 5.12b(ii)), as in the previous case, also shows peaks in power, but matching the longer periods only. However, since the preferred period are more variable in this case, averaging over time returns a poor global power spectrum (Fig. 5.12c(i)), that does not reveal the relation between the two signals.

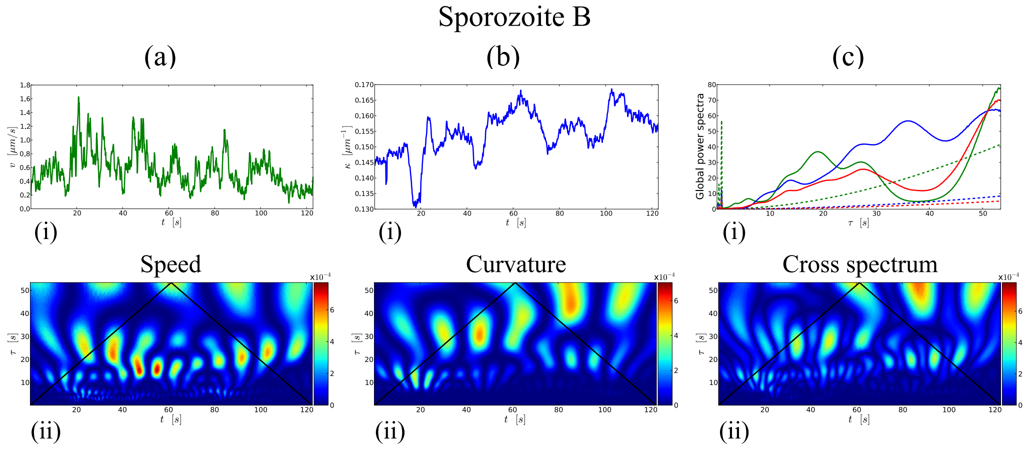

Figure 5.12: (a) (i) Speed of the sporozoite after smoothing via a sliding average. (ii) Wavelet spectrum of the speed. There are multiple, time dependent typical periods, the shortest possibly related to the molecular propulsion machinery. (b) (i) Curvature of the sporozoite after smoothing via a sliding average. (ii) Wavelet spectrum of the curvature. There are multiple time dependent typical periods, matching the longer among those in the speed spectrum, suggesting that not all the speed dynamics translates into shape changes. (c) (i) Global power spectra corresponding to speed (green), curvature (blue) and cross spectrum (red). This plot is less informative because of the time dependence of the dominating periods. (ii) Cross wavelet spectrum: the covariance between speed and curvature is meaningful but shows a time dependence.

5.8 Conclusion and outlook

With the analysis in this chapter we quantitatively related the speed and the curvature of gliding sporozoites. As, in general, these signals are non-stationary, we selected the wavelet transform as an appropriate tool to decompose the signals in both time and frequency space. This allowed to recognise at which time points particular frequencies dominate the signals.

Our results show that speed and curvature are characterised by multiple periodicities, typically time dependent. The speed appears to be a spectrally richer signal than the curvature. In fact, there are less periodicities associated with the curvature than there are for the speed. Additionally, periodicities in the curvature match only the longer among the speed periodicities. We therefore hypothesise that the speed dynamics does not always lead to changes in curvature, that may be a collateral effect of the speed features at longer periods.

Although they would doubtlessly benefit from refinements, we point out that our results are consistent with the theoretical model proposed in the first part of this chapter. In particular, the detection of multiple, simultaneously relevant timescales, among which only the longer seem to be relevant also for the curvature, points in the direction of a separation between the dynamics of the conveyer belt and that of the adhesion sites, that are linked to the deformations of the cell.

The model successfully links the peaks in the speed signal with the presence of the conveyer belt, in accordance with the experimental observation of speed peaks co-localised with regions of low curvatures. For future work, we aim at refining some assumptions, for instance the time independence of the conveyer belt or the absence of noise terms and stochasticity in the adhesion dynamics.

In the near future, the quantitative study of sporozoite migration as proposed in this chapter will benefit from ongoing experiments targeting the adhesion dynamics of sporozoites. In particular, the results will allow us to implement in the model an experimentally motivated temporal dynamics for adhesion. The groups involved in these developments are the Frischknecht group and the group of Dr. Heike Böhm (Heidelberg University).

On a shorter timescale, the analysis could benefit from the study of a higher number of cells, with longer acquisition times in order to observe more stick-slip events for each cell. This would lead to a better understanding of the interchange between dominant timescales in the signals and their relation. For comparison and to validate the results, we also propose to carry out the same analysis using mutant parasites characterised by different gliding properties than the wild type cells.

6 Summary and conclusion

Malaria ranks among the most dangerous infectious diseases. It is transmitted to vertebrate hosts by protozoan parasites of the genus *Plasmodium* via the bite of an infected *Anopheles* mosquito.

As we explained in Chapter 1, the malaria parasites are characterised by a complex life cycle, involving various stages of parasite development and replication [3, 4]. Traditionally, the study of malaria belongs to the biological and medical fields. However, studies engaging with the biophysical aspects of malaria are extremely insightful and promising [18, 19].

In this thesis we focused on the tight connection between malaria and the biophysical problem of cell migration. In fact, cell motility is fundamental for the malaria parasites to successfully complete their life cycle. The most motile developmental stage of the life cycle is represented by Plasmodium sporozoites. They show active migration in the mosquito, in the skin of the host right after a mosquito bite, and in the liver of the host, that they reach by invading a blood capillary and flowing passively with the blood stream [3–5, 11]. Remarkably, sporozoites are naturally bent and elongated cells, and describe trajectories determined by their geometrical features [21, 22]. They are driven by a complex, not yet fully understood, actomyosin-based propulsion machinery that allows smooth gliding, perturbed by the formation and rupture of dynamic adhesion sites [23–25, 27].

The problem of sporozoite motility is linked to various topics that have a history in the physics literature. The study of self-propelled particles, the emergence of collective behaviours, the problem of friction as well as data-driven biophysical modelling are all meaningful examples that we considered throughout this thesis [55, 61, 63, 100].

In developing our models for sporozoite migration we focused on the geometrical and mechanical aspects of the systems. We adopted multiple strategies depending on the problem under study: a cell level approach for the study of trajectories and structure formation, a microscopic approach for the investigation of cell adhesion via stochastic bonds, a data-driven approach to explore the connection between the gliding machinery and the shape of the cell.

In tight collaboration with the group of Prof. Dr. Friedrich Frischknecht (Heidelberg University Clinics), devoted to the experimental study of malaria with a strong focus on sporozoite motility, we developed four experimentally motivated, predictive physical models, which we presented in this thesis and summarise in this conclusion.

In Chapter 2 we investigated sporozoite migration in structured environments. This work was motivated by previous experimental work studying sporozoites moving through arrays of cylindrical obstacles [36]. These structured environments were devised in order to approximate the complexity of the host skin, through which sporozoites rapidly migrate right after injection by a mosquito bite. Choosing a cell level approach, we modelled a sporozoite as a self-propelled bent rod with bending flexibility, moving in an array of hard circular obstacles. The rod can either avoid an obstacle via a bending energy minimisation scheme, or via a stochastic reorientation of its direction of motion. We focused on the geometrical determinants of the system and quantified the migration patterns of the model sporozoites in environments with different structural properties. We concluded that the bending flexibility of the rod plays a key role in allowing migration through the obstacle arrays, generating trajectories that are quantitatively heterogeneous depending on the structural properties of the environment. We predicted that sporozoites should be sensitive to local structural anisotropies and, in addition, that they should associate preferably to obstacles that represent a geometrical fit to the cell shape. Finally, we showed that model sporozoites can loop around three-dimensional cylindrical obstacles, in a manner very similar to when sporozoites associate to and circle around a blood vessel before invading it [5]. Overall, much of the complexity observed in experiments studying sporozoite migration likely stems from the geometrical and mechanical properties of the system. The findings and predictions of our model motivated new experimental efforts, currently in progress in the Frischknecht group. The work presented in Chapter 2 has been published in [38].

In Chapter 3 we studied the collective behaviour of sporozoites. This work was motivated by the recent experimental observation of sporozoites arranged in stable, yet motile, whirl-like structures following preparation of salivary glands of malaria infected mosquitos (Frischknecht group). We described the system using a mathematical model, that predicts the appearance of various parameter dependent regimes. We further simulated the system using an agent-based approach, modelling each sporozoite as a flexible chain of springs and nodes. We showed that the curvature of the sporozoites is essential for the formation of whirl-like structures. The stability of the structures, however, depends on viscosity, on the distribution of speeds in the population and on the ability of the model sporozoites to overlap with each other. We concluded that sporozoite dynamics in the third dimension is a key factor to whirl stability. This is driving new experimental work, focusing primariy on three-dimensional imaging. The work presented in Chapter 3 is part of a collaborative effort, studying sporozoite whirls theoretically, experimentally, and by means of image processing. Together with the Schwarz group, the collaboration involves the Frischknecht group and the group of Dr. Heike Böhm (Heidelberg University).

In Chapter 4 we moved from the cell level approach adopted in the previous two chapters to a more microscopic approach, in order to investigate the adhesion dynamics of gliding sporozoites. In particular, we developed a model for stochastic friction applied to a straight rod that undergoes both translation and rotation. The motivation for this work was provided by studies of sporozoites gliding circularly on flat substrates and exhibiting a complex adhesion dynamics [27], to which both translational and rotational friction must contribute. We considered a rod of finite mass driven by a translational and a rotational spring. Our results showed that ensembles of spring-like stochastic bonds with a velocity dependent on-rate lead to complex, periodic bond patterns localised on the rod (stick-slip). As inertia is essential for this periodic stick-slip behaviour, we hypothesise that the observation of regular stick-slip behaviour in motile cells is linked to persistency in the cell motion in the presence of a complex adhesion dynamics.

In Chapter 5 we presented a theoretical model for gliding sporozoites combined with a detailed analysis of time series of sporozoite speed and curvature. Our motivation came from previous studies of stick-slip behaviour during sporozoite gliding [27]. It has been shown that the curvature of gliding sporozoites decreases following the development of an adhesion site at the rear end of the parasite. The release of this rear adhesion site is associated to a peak in the sporozoite speed and to the relaxation of the curvature to its original value. In our model we considered three key elements, namely the curvature of sporozoites, their bending flexibility and a minimal description of their gliding machinery, featuring a conveyer belt and adhesion sites at the cell ends. We linked the dynamics of adhesion formation and rupture to the deformations of the cell. We explicitly considered the geometrical non linearity given by the bent cell shape, and showed that the presence of a conveyer belt is essential for the observation of speed peaks. In the second part of the chapter, we studied time series of sporozoite speed and curvature using wavelet analysis. This represents the first study to quantitatively relate sporozoite speed and curvature. We identified multiple relevant periodicities in the speed signals. Observing that only the longer periodicities find a match in the curvature spectrum, we concluded that the speed dynamics only partly translates into shape changes, which strongly suggests a separation between the adhesion and the conveyer belt dynamics.

Overall, in this thesis we adopted a biophysical approach to the study of sporozoite migration, that proved successful in complementing challenging biological experiments and quantification problems. In Chapter 2 we could formalise the dependence of sporozoite migration patterns on the geometrical features of the environment, abstracting from the details of the cell propulsion machinery and the unavoidable biological variance present in a population of sporozoites. In Chapter 3 modelling allowed to investigate and infer the structural features of an ensemble of self-organised sporozoites, a system too complex to be fully controllable experimentally. Our predictive results are driving new, targeted imaging efforts. In Chapter 4 we used stochastic bond dynamics to connect friction and persistency in the cell motion with the appearance of stick-slip bond patterns similar to those observed during sporozoite gliding. Finally, in Chapter 5, we proposed a first model linking the propulsion machinery of sporozoites to changes in cell shape. We showed that speed and curvature time series allow to investigate the connection between the molecular machinery of propulsion and the variations in cell shape, triggering new experiments and providing perspective for further modelling.

In conclusion, we used theoretical modelling, computer simulations, together with a careful analysis of simulated and experimental data to understand the problem of sporozoite gliding. Our models, focusing on various systems and approaches, explain the experimental observations using physical arguments, and generate predictions that are currently fuelling new experimental efforts. We are now a step closer to unraveling the complexity behind sporozoite gliding. We believe that ours is only the first of many progresses in this direction, and that the study of malaria parasites will benefit greatly from targeted biophysical modelling.

Bibliography

[1] World Health Organisation. World malaria report. 2014.

[2] G Snounou. Detection and identification of the four malaria parasite species infecting humans by PCR amplification. In *Species Diagnostics Protocols*, pages 263–291. Springer, 1996.

[3] L Bannister and G Mitchell. The ins, outs and roundabouts of malaria. *Trends Parasitol*, 19(5):209–13, 2003.

[4] R Ménard, J Tavares, I Cockburn, M Markus, F Zavala, and R Amino. Looking under the skin: the first steps in malarial infection and immunity. *Nat Rev Microbiol*, 11(10):701–12, 2013.

[5] R Amino, S Thiberge, B Martin, S Celli, S Shorte, F Frischknecht, and R Ménard. Quantitative imaging of Plasmodium transmission from mosquito to mammal. *Nat Med*, 12(2):220–4, 2006.

[6] AG Maier, BM Cooke, AF Cowman, and L Tilley. Malaria parasite proteins that remodel the host erythrocyte. *Nat Rev Microbiol*, 7(5):341–54, 2009.

[7] P Horrocks, RA Pinches, SJ Chakravorty, J Papakrivos, Z Christodoulou, SA Kyes, BC Urban, DJP Ferguson, and CI Newbold. PfEMP1 expression is reduced on the surface of knobless Plasmodium falciparum infected erythrocytes. *J Cell Sci*, 118(11):2507–18, 2005.

[8] DA Fedosov, B Caswell, S Suresh, and GE Karniadakis. Quantifying the biophysical characteristics of Plasmodium-falciparum-parasitized red blood cells in microcirculation. *P Natl Acad Sci USA*, 108(1):35–9, 2011.

[9] JP Shelby, J White, K Ganesan, PK Rathod, and DT Chiu. A microfluidic model for single-cell capillary obstruction by Plasmodium falciparum-infected erythrocytes. *P Natl Acad Sci USA*, 100(25):14618–22, 2003.

[10] M Ho, MJ Hickey, AG Murray, G Andonegui, and P Kubes. Visualization of Plasmodium falciparum–endothelium interactions in human microvasculature mimicry of leukocyte recruitment. *J Exp Med*, 192(8):1205–12, 2000.

[11] AK Mueller, F Kohlhepp, C Hammerschmidt, and K Michel. Invasion of mosquito salivary glands by malaria parasites: prerequisites and defense strategies. *Int J Parasitol*, 40(11):1229–35, 2010.

[12] M Prudêncio, A Rodriguez, and MM Mota. The silent path to thousands of merozoites: the Plasmodium liver stage. *Nat Rev Microbiol*, 4(11):849–56, 2006.

[13] AF Cowman and BS Crabb. Invasion of red blood cells by malaria parasites. *Cell*, 124(4):755–66, 2006.

[14] J Pinder, R Fowler, L Bannister, A Dluzewski, and G Mitchell. Motile systems in malaria merozoites: how is the red blood cell invaded? *Parasitol Today*, 16(6):240–5, 2000.

[15] E Nagao, O Kaneko, and JA Dvorak. Plasmodium falciparum-infected erythrocytes: Qualitative and quantitative analyses of parasite-induced knobs by atomic force microscopy. *J Struct Biol*, 130(1):34–44, 2000.

[16] RP McEver and C Zhu. Rolling cell adhesion. *Annu Rev Cell Dev Bi*, 26:363, 2010.

[17] CB Korn and US Schwarz. Dynamic states of cells adhering in shear flow: from slipping to rolling. *Phys Rev E*, 77(4):041904, 2008.

[18] S Dasgupta, T Auth, NS Gov, TJ Satchwell, E Hanssen, ES Zuccala, DT Riglar, AM Toye, T Betz, J Baum, et al. Membrane-wrapping contributions to malaria parasite invasion of the human erythrocyte. *Biophys J*, 107(1):43–54, 2014.

[19] M Abkarian, G Massiera, L Berry, M Roques, and C Braun-Breton. A novel mechanism for egress of malarial parasites from red blood cells. *Blood*, 117(15):4118–24, 2011.

[20] A Callan-Jones, OE Albarran Arriagada, G Massiera, V Lorman, and M Abkarian. Red blood cell membrane dynamics during malaria parasite egress. *Biophys J*, 103(12):2475–83, 2012.

[21] M Kudryashev, S Münter, L Lemgruber, G Montagna, H Stahlberg, K Matuschewski, M Meissner, M Cyrklaff, and F Frischknecht. Structural basis for chirality and directional motility of Plasmodium sporozoites. *Cell Microbiol*, 14(11):1757–68, 2012.

[22] JP Vanderberg. Studies on the motility of Plasmodium sporozoites. *J Protozool*, 21(4):527–37, 1974.

[23] SHI Kappe, CA Buscaglia, and V Nussenzweig. Plasmodium sporozoite molecular cell biology. *Annu Rev Cell Dev Biol*, 20:29–59, 2004.

[24] GN Montagna, K Matuschewski, and CA Buscaglia. Plasmodium sporozoite motility: an update. *Front Biosci*, 17:726–44, 2012.

[25] S Hegge, S Münter, M Steinbüchel, K Heiss, U Engel, K Matuschewski, and F Frischknecht. Multistep adhesion of Plasmodium sporozoites. *FASEB J*, 24(7):2222–34, 2010.

[26] J Baum, AT Papenfuss, B Baum, TP Speed, and AF Cowman. Regulation of apicomplexan actin-based motility. *Nat Rev Microbiol*, 4(8):621–8, 2006.

[27] S Münter, B Sabass, C Selhuber-Unkel, M Kudryashev, S Hegge, U Engel, JP Spatz, K Matuschewski, US Schwarz, and F Frischknecht. Plasmodium sporozoite motility is modulated by the turnover of discrete adhesion sites. *Cell Host Microbe*, 6(6):551–62, 2009.

[28] MJ McBride. Bacterial gliding motility: multiple mechanisms for cell movement over surfaces. *Annu Rev Microbiol*, 55(1):49–75, 2001.

[29] T Mignot, JW Shaevitz, PL Hartzell, and DR Zusman. Evidence that focal adhesion complexes power bacterial gliding motility. *Science*, 315(5813):853–6, 2007.

[30] M Sun, M Wartel, E Cascales, JW Shaevitz, and T Mignot. Motor-driven intracellular transport powers bacterial gliding motility. *P Natl Acad Sci USA*, 108(18):7559–64, 2011.

[31] R Ross. On some peculiar pigmented cells found in two mosquitos fed on malarial blood. *Brit Med J*, 2(1929):1786, 1897.

[32] M Kudryashev, S Lepper, W Baumeister, M Cyrklaff, and F Frischknecht. Geometric constrains for detecting short actin filaments by cryogenic electron tomography. *BMC Biophys*, 3(1):6, 2010.

[33] M Cyrklaff, M Kudryashev, A Leis, K Leonard, W Baumeister, R Menard, M Meissner, and F Frischknecht. Cryoelectron tomography reveals periodic material at the inner side of subpellicular microtubules in apicomplexan parasites. *J Exp Med*, 204(6):1281–7, 2007.

[34] S Hegge, K Uhrig, M Streichfuss, G Kynast-Wolf, K Matuschewski, JP Spatz, and F Frischknecht. Direct manipulation of malaria parasites with optical tweezers reveals distinct functions of Plasmodium surface proteins. *ACS nano*, 6(6):4648–62, 2012.

[35] N Perschmann, JK Hellmann, F Frischknecht, and JP Spatz. Induction of malaria parasite migration by synthetically tunable microenvironments. *Nano Lett*, 11(10):4468–74, 2011.

[36] JK Hellmann, S Münter, M Kudryashev, S Schulz, K Heiss, AK Müller, K Matuschewski, JP Spatz, US Schwarz, and F Frischknecht. Environmental constraints guide migration of malaria parasites during transmission. *PLoS Pathog*, 7(6):e1002080, 2011.

[37] S Hegge, M Kudryashev, A Smith, and F Frischknecht. Automated classification of Plasmodium sporozoite movement patterns reveals a shift towards productive motility during salivary gland infection. *Biotechnol J*, 4(6):903–13, 2009.

[38] A Battista, F Frischknecht, and US Schwarz. Geometrical model for malaria parasite migration in structured environments. *Phys Rev E*, 90(4):042720, 2014.

[39] US Schwarz and SA Safran. Physics of adherent cells. *Rev Mod Phys*, 85(3):1327, 2013.

[40] T Erdmann and US Schwarz. Stochastic force generation by small ensembles of myosin II motors. *Phys Rev Lett*, 108(18):188101, 2012.

[41] Y Wu, Y Jiang, D Kaiser, and M Alber. Social interactions in myxobacterial swarming. *PLoS Comput Biol*, 3(12):e253, 2007.

[42] A Vanossi, N Manini, M Urbakh, S Zapperi, and E Tosatti. Colloquium: Modeling friction: From nanoscale to mesoscale. *Rev Mod Phys*, 85(2):529, 2013.

[43] GI Bell. Models for the specific adhesion of cells to cells. *Science*, 200(4342):618–27, 1978.

[44] T Erdmann and US Schwarz. Stochastic dynamics of adhesion clusters under shared constant force and with rebinding. *J Chem Phys*, 121(18):8997–9017, 2004.

[45] M Srinivasan and S Walcott. Binding site models of friction due to the formation and rupture of bonds: state-function formalism, force-velocity relations, response to slip velocity transients, and slip stability. *Phys Rev E*, 80(4):046124, 2009.

[46] Y Li, P Bhimalapuram, and AR Dinner. Model for how retrograde actin flow regulates adhesion traction stresses. *J Phys-Condens Mat*, 22(19):194113, 2010.

[47] B Sabass and US Schwarz. Modeling cytoskeletal flow over adhesion sites: competition between stochastic bond dynamics and intracellular relaxation. *J Phys-Condens Mat*, 22(19):194112, 2010.

[48] BL Bangasser, SS Rosenfeld, and DJ Odde. Determinants of maximal force transmission in a motor-clutch model of cell traction in a compliant microenvironment. *Biophys J*, 105(3):581–92, 2013.

[49] P Sens. Rigidity sensing by stochastic sliding friction. *Europhys Lett*, 104(3):38003, 2013.

[50] AE Filippov, J Klafter, and M Urbakh. Friction through dynamical formation and rupture of molecular bonds. *Phys Rev Lett*, 92(13):135503, 2004.

[51] O Ben-David, SM Rubinstein, and J Fineberg. Slip-stick and the evolution of frictional strength. *Nature*, 463(7277):76–9, 2010.

[52] A Schirmeisen, L Jansen, and H Fuchs. Tip-jump statistics of stick-slip friction. *Phys Rev B*, 71(24):245403, 2005.

[53] CE Chan and DJ Odde. Traction dynamics of filopodia on compliant substrates. *Science*, 322(5908):1687–91, 2008.

[54] ML Gardel, B Sabass, L Ji, G Danuser, US Schwarz, and CM Waterman. Traction stress in focal adhesions correlates biphasically with actin retrograde flow speed. *J Cell Biol*, 183(6):999–1005, 2008.

[55] S van Teeffelen and H Löwen. Dynamics of a Brownian circle swimmer. *Phys Rev E*, 78(2):020101, 2008.

[56] V Zaburdaev, S Uppaluri, T Pfohl, M Engstler, R Friedrich, and H Stark. Langevin dynamics deciphers the motility pattern of swimming parasites. *Phys Rev Lett*, 106(20):208103, 2011.

[57] BM Friedrich and F Jülicher. The stochastic dance of circling sperm cells: sperm chemotaxis in the plane. *New J Phys*, 10(12):123025, 2008.

[58] V Lobaskin, D Lobaskin, and IM Kulić. Brownian dynamics of a microswimmer. *Eur Phys J-Spec Top*, 157(1):149–56, 2008.

[59] Y Or. Asymmetry and stability of shape kinematics in microswimmers' motion. *Phys Rev Lett*, 108(25):258101, 2012.

[60] P Romanczuk and L Schimansky-Geier. Brownian motion with active fluctuations. *Phys Rev Lett*, 106(23):230601, 2011.

[61] D Selmeczi, L Li, LII Pedersen, SF Norrelykke, PH Hagedorn, S Mosler, NB Larsen, EC Cox, and H Flyvbjerg. Cell motility as random motion: a review. *Eur Phys J-Spec Top*, 157(1):1–15, 2008.

[62] Y Wu, AD Kaiser, Y Jiang, and MS Alber. Periodic reversal of direction allows Myxobacteria to swarm. *P Natl Acad Sci USA*, 106(4):1222–7, 2009.

[63] T Vicsek and A Zafeiris. Collective motion. *Phys Rep*, 517(3):71–140, 2012.

[64] T Vicsek, A Czirók, E Ben-Jacob, I Cohen, and O Shochet. Novel type of phase transition in a system of self-driven particles. *Phys Rev Lett*, 75(6):1226, 1995.

[65] L Li, EC Cox, and H Flyvbjerg. 'Dicty dynamics': Dictyostelium motility as persistent random motion. *Phys Biol*, 8(4):046006, 2011.

[66] E Lauga, WR DiLuzio, GM Whitesides, and HA Stone. Swimming in circles: motion of bacteria near solid boundaries. *Biophys J*, 90(2):400–12, 2006.

[67] R Amino, D Giovannini, S Thiberge, P Gueirard, B Boisson, JF Dubremetz, MC Prévost, T Ishino, M Yuda, and R Ménard. Host cell traversal is important for progression of the malaria parasite through the dermis to the liver. *Cell Host Microbe*, 3(2):88–96, 2008.

[68] M Akaki and JA Dvorak. A chemotactic response facilitates mosquito salivary gland infection by malaria sporozoites. *J Exp Biol*, 208(16):3211–8, 2005.

[69] S Johari, V Nock, MM Alkaisi, and W Wang. On-chip analysis of C. elegans muscular forces and locomotion patterns in microstructured environments. *Lab Chip*, 13(9):1699–707, 2013.

[70] D Arcizet, S Capito, M Gorelashvili, C Leonhardt, M Vollmer, S Youssef, S Rappl, and D Heinrich. Contact-controlled amoeboid motility induces dynamic cell trapping in 3D-microstructured surfaces. *Soft Matter*, 8(5):1473–81, 2012.

[71] C Meel, N Kouzel, ER Oldewurtel, and B Maier. Three-dimensional obstacles for bacterial surface motility. *Small*, 8(4):530–4, 2012.

[72] N Heddergott, T Krüger, SB Babu, A Wei, E Stellamanns, S Uppaluri, T Pfohl, H Stark, and M Engstler. Trypanosome motion represents an adaptation to the crowded environment of the vertebrate bloodstream. *PLoS Pathog*, 8(11):e1003023, 2012.

[73] MB Heintzelman. Cellular and molecular mechanics of gliding locomotion in eukaryotes. *Int Rev Cytol*, 251:79–129, 2006.

[74] B Rubinstein, MF Fournier, K Jacobson, AB Verkhovsky, and A Mogilner. Actin-myosin viscoelastic flow in the keratocyte lamellipod. *Biophys J*, 97(7):1853–63, 2009.

[75] F Ziebert and IS Aranson. Effects of adhesion dynamics and substrate compliance on the shape and motility of crawling cells. *PloS One*, 8(5):e64511, 2013.

[76] S Schmitz, IAT Schaap, J Kleinjung, S Harder, M Grainger, L Calder, PB Rosenthal, AA Holder, and C Veigel. Malaria parasite actin polymerization and filament structure. *J Biol Chem*, 285(47):36577–85, 2010.

[77] JF Joanny, F Jülicher, and J Prost. Motion of an adhesive gel in a swelling gradient: a mechanism for cell locomotion. *Phys Rev Lett*, 90(16):168102, 2003.

[78] AE Carlsson. Mechanisms of cell propulsion by active stresses. *New J Phys*, 13(7):073009, 2011.

[79] F Peruani and LG Morelli. Self-propelled particles with fluctuating speed and direction of motion in two dimensions. *Phys Rev Lett*, 99(1):010602, 2007.

[80] C Reichhardt and CJO Reichhardt. Dynamics and separation of circularly moving particles in asymmetrically patterned arrays. *Phys Rev E*, 88(4):042306, 2013.

[81] F Kümmel, B ten Hagen, R Wittkowski, I Buttinoni, R Eichhorn, G Volpe, H Löwen, and C Bechinger. Circular motion of asymmetric self-propelling particles. *Phys Rev Lett*, 110(19):198302, 2013.

[82] J Starruß, Th Bley, L Søgaard-Andersen, and A Deutsch. A new mechanism for collective migration in Myxococcus xanthus. *J Stat Phys*, 128(1-2):269–86, 2007.

[83] S Sidjanski and JP Vanderberg. Delayed migration of Plasmodium sporozoites from the mosquito bite site to the blood. *Am J Trop Med Hyg*, 57(4):426–29, 1997.

[84] JP Vanderberg and U Frevert. Intravital microscopy demonstrating antibody-mediated immobilisation of Plasmodium berghei sporozoites injected into skin by mosquitoes. *Int J Parasitol*, 34(9):991–6, 2004.

[85] B Richter, T Pauloehrl, J Kaschke, D Fichtner, J Fischer, AM Greiner, D Wedlich, M Wegener, G Delaittre, C Barner-Kowollik, et al. Three-dimensional microscaffolds exhibiting spatially resolved surface chemistry. *Adv Mater*, 25(42):6117–22, 2013.

[86] JL Connell, ET Ritschdorff, M Whiteley, and JB Shear. 3D printing of microscopic bacterial communities. *P Natl Acad Sci USA*, 110(46):18380–5, 2013.

[87] S Håkansson, H Morisaki, J Heuser, and LD Sibley. Time-lapse video microscopy of gliding motility in Toxoplasma gondii reveals a novel, biphasic mechanism of cell locomotion. *Mol Biol Cell*, 10(11):3539–47, 1999.

[88] Y Cai, T Erdmann, and US Schwarz. Stochastic modelling of malaria parasite gliding motility. *Unpublished draft.*

[89] L Haeggqwist, L Schimansky-Geier, IM Sokolov, and F Moss. Hopping on a zig-zag course. *Eur Phys J-Spec Top*, 157(1):33–42, 2008.

[90] L Schimansky-Geier, U Erdmann, and N Komin. Advantages of hopping on a zig-zag course. *Physica A*, 351(1):51–9, 2005.

[91] F Frischknecht, P Baldacci, B Martin, C Zimmer, S Thiberge, JC Olivo-Marin, SL Shorte, and R Ménard. Imaging movement of malaria parasites during transmission by Anopheles mosquitoes. *Cell Microbiol*, 6(7):687–94, 2004.

[92] V Schaller, C Weber, C Semmrich, E Frey, and AR Bausch. Polar patterns of driven filaments. *Nature*, 467(7311):73–7, 2010.

[93] X Trepat, MR Wasserman, TE Angelini, E Millet, DA Weitz, JP Butler, and JJ Fredberg. Physical forces during collective cell migration. *Nat Phys*, 5(6):426–30, 2009.

[94] C Makris, P Ratilal, S Jagannathan, Z Gong, M Andrews, I Bertsatos, OR Godø, RW Nero, and JM Jech. Critical population density triggers rapid formation of vast oceanic fish shoals. *Science*, 323(5922):1734–7, 2009.

[95] M Ballerini, N Cabibbo, R Candelier, A Cavagna, E Cisbani, I Giardina, V Lecomte, A Orlandi, G Parisi, A Procaccini, et al. Interaction ruling animal collective behavior depends on topological rather than metric distance: Evidence from a field study. *P Natl Acad Sci USA*, 105(4):1232–7, 2008.

[96] S Mishra, A Baskaran, and MC Marchetti. Fluctuations and pattern formation in self-propelled particles. *Phys Rev E*, 81(6):061916, 2010.

[97] A Baskaran and MC Marchetti. Statistical mechanics and hydrodynamics of bacterial suspensions. *P Natl Acad Sci USA*, 106(37):15567–72, 2009.

[98] Y Yang, F Qiu, and G Gompper. Self-organized vortices of circling self-propelled particles and curved active flagella. *Phys Rev E*, 89(1):012720, 2014.

[99] BNJ Persson. *Sliding friction: physical principles and applications*, volume 1. Springer, 2000.

[100] M Urbakh, J Klafter, D Gourdon, and J Israelachvili. The nonlinear nature of friction. *Nature*, 430(6999):525–8, 2004.

[101] A Schallamach. A theory of dynamic rubber friction. *Wear*, 6(5):375–82, 1963.

[102] BNJ Persson. Theory of friction: Stress domains, relaxation, and creep. *Phys Rev B*, 51(19):13568, 1995.

[103] T Erdmann and US Schwarz. Stability of adhesion clusters under constant force. *Phys Rev Lett*, 92(10):108102, 2004.

[104] EL Barnhart, GM Allen, F Jülicher, and JA Theriot. Bipedal locomotion in crawling cells. *Biophys J*, 98(6):933–42, 2010.

[105] A Chateauminois, C Fretigny, and L Olanier. Friction and shear fracture of an adhesive contact under torsion. *Phys Rev E*, 81(2):026106, 2010.

[106] H Levine, WJ Rappel, and I Cohen. Self-organization in systems of self-propelled particles. *Phys Rev E*, 63(1):017101, 2000.

[107] C Weber, PK Radtke, L Schimansky-Geier, and P Hänggi. Active motion assisted by correlated stochastic torques. *Phys Rev E*, 84(1):011132, 2011.

[108] C Drummond, J Israelachvili, and Ph Richetti. Friction between two weakly adhering boundary lubricated surfaces in water. *Phys Rev E*, 67(6):066110, 2003.

[109] EM Purcell. Life at low Reynolds number. *Am J Phys*, 45(1):3–11, 1977.

[110] M Kass, A Witkin, and D Terzopoulos. Snakes: Active contour models. *International journal of computer vision*, 1(4):321–31, 1988.

[111] I Daubechies et al. *Ten lectures on wavelets*, volume 61. SIAM, 1992.

[112] C Torrence and GP Compo. A practical guide to wavelet analysis. *B Am Meteorol Soc*, 79(1):61–78, 1998.

[113] DP Percival. On estimation of the wavelet variance. *Biometrika*, 82(3):619–31, 1995.

Acknowledgements

For giving me the opportunity to work on this doctoral thesis, for the supervision and the many inputs, I would like to thank deeply Prof. Dr. Ulrich Schwarz and Prof. Dr. Friedrich Frischknecht.

Past and present members of the Schwarz group all deserve special thanks, be it for discussion, proofreading, or helpful questions and answers. In particular, I would like to thank Christoph, Jérôme, Julian and Marco, who contributed to this work by kindly double checking its developments with me.

A heartfelt thank you goes to all members of the Frischknecht group, for the fruitful collaboration and their patience. Many special thanks to Konrad and Mendi, who made the experimental part of this doctoral thesis possible, and to Catherine and Mirko, for all the useful discussions.

Many thanks to Prof. Dr. Heinz Horner for kindly being the second referee of this thesis.

I am deeply grateful to my parents and siblings, for their constant support and regular supply of mailed goods. A fabulous thank you goes to Stefano, who knows that the sum of many trains is a train to the future.